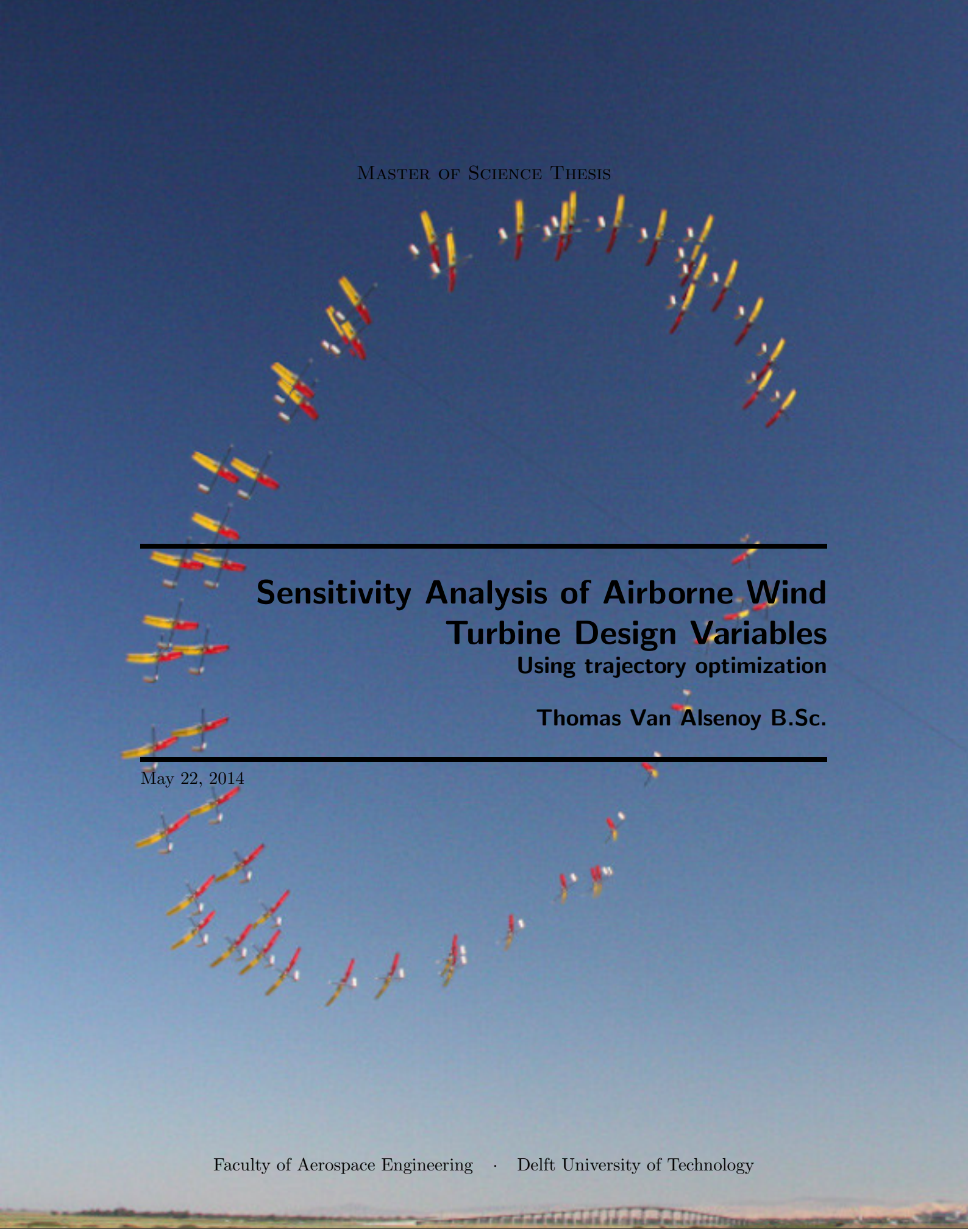

Master of Science Thesis

Sensitivity Analysis of Airborne Wind Turbine Design Variables

Using trajectory optimization

Thomas Van Alsenoy B.Sc.

May 22, 2014

Faculty of Aerospace Engineering · Delft University of Technology

TU Delft Delft University of Technology

CONFIDENTIAL

Challenge the future

Sensitivity Analysis of Airborne Wind Turbine Design Variables

Using trajectory optimization

Master of Science Thesis

For obtaining the degree of Master of Science in Aerospace Engineering at Delft University of Technology

Thomas Van Alsenoy B.Sc.

May 22, 2014

Faculty of Aerospace Engineering · Delft University of Technology

Delft University Of Technology
Department Of
Wind Energy

The undersigned hereby certify that they have read and recommend to the Faculty of Aerospace Engineering for acceptance a thesis entitled **"Sensitivity Analysis of Airborne Wind Turbine Design Variables"** by **Thomas Van Alsenoy B.Sc.** in partial fulfillment of the requirements for the degree of **Master of Science**.

Dated: May 22, 2014

Head of department: _____
Prof. dr. G.J.W. van Bussel

Supervisor: _____
Dr.ing R. Schmehl

Reader: _____
Dr.ir M. Voskuijl

Reader: _____
PhD. candidate G. Horn

Summary

The objective of this research is to determine the impact of design variables on power output of the Makani Power Wing7 airborne wind turbine. This system consists of a rigid wing connected to the ground using a using a number of bridles and a tether. The tethered wing flies crosswind trajectories and generates power using on-board turbines. Sensitivities of power output to design variables are required for various design trade-offs.

A simulation and optimization approach is presented which allows analysis of a fairly complex model with realistic controls and constraints. Using trajectory optimization removes the assumption of a predefined trajectory and allows analysis of the impact of the flightpath itself.

The wing is modeled as a rigid body with six degrees of freedom. Aerodynamic forces are determined using a response surface on results of a vortex lattice code. A time-varying position of the bridle attachment point couples the wing to the tether. This tether is implemented as a straight elastic element with analytic approximations for the effects of mass and aerodynamic drag. The power system model consists of a turbine response surface and DC-equivalent generator model.

Optimal trajectories are determined using the direct collocation method resulting in a capacity factor of 48.1% for a site with uniform wind field and annual mean wind speed of 7.5 m/s.

The relative impact of aerodynamic lift and drag on long term averaged power output are found to be an order magnitude more important than wing mass. Topology and circularity of the flight path are found to have a low impact on power.

Acknowledgments

This research was performed at the Makani Power project at Google[x]. Being able to work on systems which will physically exist, fly and generate power in such a beautiful, ingenious way has been the most perfect graduation adventure I could ever imagine.

I would like to sincerely thank the entire Makani team for the opportunity they gave me, their engineering passion they shared with me and their warm welcome in the team. In particular I would like to thank Damon Vander Lind for his continuous support, patience with my constant stream of questions, and for giving me the freedom to challenge every aspect of the design. Furthermore, I would like to thank Kenny Jensen, Erik Chubb and Paula Echeverri for brainstorming and challenging my ideas on a daily basis.

It's hard to imagine doing this thesis without the assistance of PhD candidate Greg Horn. First of all, without his numerical work on trajectory optimization a study like this would have been gruesome. Secondly, his patient support on using his software tool *Rawesome* allowed me to start this thesis with a working trajectory optimizer. Finally, his critical review of my work and understanding as part of my graduation committee is deeply appreciated. Greg, thanks a lot.

From the faculty of aerospace engineering I would like to gratefully thank my supervisor Dr. Ing. Roland Schmehl for keeping me on track and preventing me from reinventing the wheel on numerous occasions. I would like to thank Prof. dr. Gerard van Bussel for reading my thesis and being the head of the committee. Finally I would like thank Dr.Ir. Mark Voskuil for being part of my committee and making the Flight Performance and Propulsion masters track so divers and interesting.

Contents

List of Figures

List of Tables

Nomenclature

Latin Symbols

$\boldsymbol{a}$	acceleration vector	ms^{-2}
A_t	tether cross sectional area	m^2
$C_{d,t}$	tether drag coefficient, referenced to diameter	$-$
C_D	wing drag coefficient	$-$
C_L	wing lift coefficient	$-$
C_P	pressure coefficient	$-$
C_l, C_m, C_n	aerodynamic moment coefficients in the E_B frame	$-$
C_X, C_Y, C_Z	aerodynamic force coefficients in the E_B frame	$-$
C_{a_b}	aerodynamic stability or control derivative, effect of b on C_a	$-$
d_t	tether diameter	m
D	propeller diameter	m
D_{prop}	propeller drag force	N
$\boldsymbol{e}$	unit vector	$-$
E	reference frame	$-$
E_t	tether Young's modulus	Nm^{-2}
$F_{g,t,k}$	force at the wing due to gravity on the tether	N
g	gravitational acceleration	ms^{-2}
I	moment inertia around spin axis	kgm^2
I	generator current	A
$\boldsymbol{j}$	jerk vector	ms^{-3}
J	optimization objective function	W

J	propeller advance ratio	$-$
$\boldsymbol{J}$	moment of inertia tensor	kgm^2
k_τ	generator torque constant	NmA^{-1}
k_n	generator speed constant	$rads^{-1}V^{-1}$
k_t	tether spring constant	Nm^{-1}
l_{br}	distance between bridle point and Y_B axis	m
l_{tot}	total length of tether and bridle system	m
l_{t}	tether length	m
$l_{t,0}$	tether length at zero strain	m
$\mathcal{L}$	Lagrangian	J
m_{in}	total inertial system mass	kg
m_k	wing mass	kg
m_t	tether mass	kg
$\boldsymbol{M}$	moment vector	Nm
N	winding number	$-$
$\hat{p}, \hat{q}, \hat{r}$	non-dimensional rates in E_B frame	$-$
p, q, r	dimensional rates in E_B frame	$rads^{-1}$
$P_{\mathrm{el,gen}}$	generator electrical output power	W
$P_{\mathrm{el,mc}}$	motor controller electrical output power	W
$P_{\mathrm{el,teth}}$	electrical power at the ground side of the tether	W
P_{rat}	rated power output	W
P_{sh}	propeller shaft power	W
P_{sys}	long term average power output	W
q	generalized coordinate	$-$
Q	generalized force	$-$
$\boldsymbol{r}$	position vector of wing cg	m
$\boldsymbol{R}_{EB}$	rotation matrix converting a vector from frame E_B to E_E	$-$
R	generator resistive impedance	Ω
$\tilde{S}_a^B$	semirelative sensitivity of variable a to metric B	unit B
S_a^B	absolute sensitivity of variable a to metric B	unit B (unit a)$^{-1}$
t	time	s
T	kinetic energy	J
T	trajectory end time	s
$\boldsymbol{u}$	control variable vector	$-$
$\boldsymbol{V}$	wing center of gravity velocity vector	ms^{-1}
$\boldsymbol{V}_a$	airspeed vector	ms^{-1}
V	generator voltage	V
V	potential energy	J

$V_{\text{a,prop}}$	local airspeed at propeller plane	ms^{-1}
$\boldsymbol{w}$	wind speed vector	ms^{-1}
$w_{\text{cut,in}}$	cut-in wind speed	ms^{-1}
$w_{\text{cut,out}}$	cut-out wind speed	ms^{-1}
w_{rat}	rated wind speed	ms^{-1}

Greek Symbols

α	aerodynamic angle of attack	rad
β	aerodynamic sideslip angle	rad
β	tether elevation angle	rad
δ	control surface deflection	rad
ζ	power harvesting factor	$-$
η	efficiency	$-$
κ	flight path curvature	m^{-1}
θ_{br}	bridle pitch angle	rad
θ_t	tether pitch angle	rad
ρ	air density	kgm^{-3}
ρ	flight path radius of curvature	m
σ	standard deviation	$-$
τ	propeller shaft torque	Nm
τ_{fric}	generator friction torque	Nm
ϕ_{br}	bridle roll angle	rad
χ_{br}	bridle aperture angle	rad
$\boldsymbol{\omega}$	angular rates of the E_B frame	$rads^{-1}$
Ω	propeller rotational speed	$rads^{-1}$

Subscripts

$\overline{B}$	body reference frame with origin at wing center of mass
A	aerodynamic reference frame
br	bridle
B	body reference frame with origin at ground station
ec	eddy current
E	earth reference frame
gen	generator
max	maximum

$_{mc}$	motor controller
$_{opt}$	optimal
$_{prop}$	propeller
$_{ref}$	reference value
$_{t}$	tether

Abbreviations

AD	automatic differentiation
AVL	athena vortex lattice
AWE	airborne wind energy
AWT	airborne wind turbine
CFD	computational fluid dynamics
DAE	differential algebraic equation
DCM	direction cosine matrix
DNS	direct numerical simulation
DOE	design of experiments
DOF	degree of freedom
HAWT	horizontal axis wind turbine
IEC	international electrotechnical commission
IPCC	intergovernmental panel on climate change
IPOPT	interior point optimizer
LCOE	levelized cost of energy
NLP	non linear programming
NOAA	national oceanic and atmospheric administration
NOP	normal operating point
OCP	optimal control problem
ODE	ordinary differential equation
OFAT	one factor at a time
RANS	Reynolds averaged Navier-Stokes
RPC	representative concentration pathway
SNOPT	sparse nonlinear optimizer
SQP	sequential quadratic programming

Other Symbols

$\mathbf{1}_{x,y,z}$	column vector with all zeros except a one on the respective entry

1

Introduction

In order to put the topic of this thesis in a wider perspective, section 1.1 reviews the current global energy and climate situation and the role of conventional wind energy. Section 1.2 then introduces the field of airborne wind energy and its potential. The research question, goals and report structure are then presented in section 1.3.

1.1 Global energy production and climate outlook

The world population has doubled between 1970 and 2012 and is still growing rapidly at a rate of about 1.2 % per year [1]. The United Nations predicts a population increase to 9.6 billion by 2050 and 10.9 billion by 2100 [8]. Additionally, the average gross domestic product (GDP) per capita has almost doubled between 1970 and 2012 [1]. As global wealth levels increase, the energy use per capita increases, reaching 1760 kg of oil equivalent (73 GJ) per capita per year by 2012. This is the highest level in human history [1]. The combined effect of these trends will lead to a significant increase in global energy demand. According to the U.S. Department of Energy [9], the global annual energy demand is expected to increase from 524 quadrillion Btu in 2010 to 820 quadrillion Btu in 2040, an average increase of 1.5% per year.

1.1.1 Climate impact

As world population and GDP per capita rise quickly, so does pressure on the global environment. The fifth assessment report of the intergovernmental panel on climate change (IPCC) [10] presents a tremendous amount of scientific work and predicts the effect of a number of radiative forcing scenarios called representative concentration pathways (RPC). The four scenarios RCP 2.6, 4.5, 6.0 and 8.5 represent a concentration of 421, 538, 670 and 937 ppm of atmospheric CO_2 respectively by 2100. Figure 1.1 shows the predicted impact of these scenarios on mean global surface temperature.

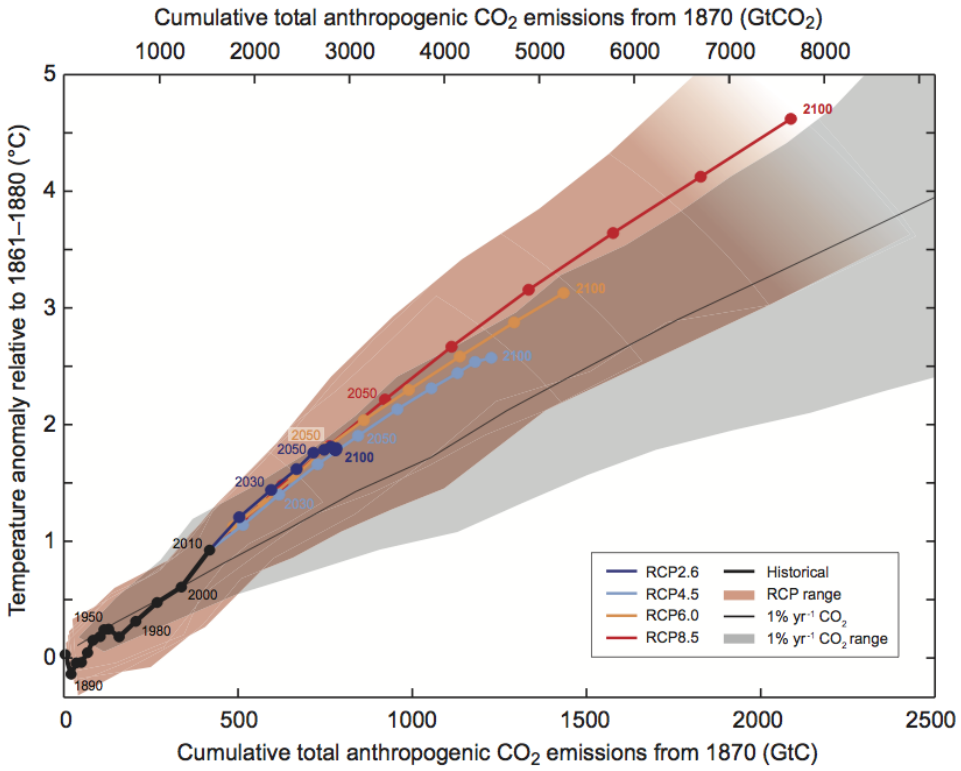

Figure 1.1: Mean global surface temperature anomaly for different representative concentration pathways and their predicted effect on global surface temperature as used by the IPCC in the Fifth Assessment Report. The dots represent the end of a decade and the and the plumes represent the uncertainty for the different scenarios [10]

In 2003 the yearly average CO_2 concentration measured by NOAA was 375.77 ppm, ten years later, in 2013, it measured 396.48 ppm. This suggests that a concentration of 421 ppm by 2100 is highly unlikely as the annual growth rate of about 2 ppm/year is still increasing [11].

A difficult topic is to quantify the impact of a certain temperature anomaly. Political discussions seem to have agreed on a maximum allowed temperature anomaly of 2°C by 2100 [12, 13] based on an expected sea level rise of around 1m [10]. Hansen et al. [14] warn for the danger of such targets as those are still assuming a linear response between global warming and sea level rise. They argue that although it is hard to predict exactly when, a rapid non-linear disintegration of ice sheets will probably happen if warming continues to the 2°C anomaly. Similar rapid responses have been observed in the Eemian period. During this period peak sea level rose 9m higher than the current level, while global average temperatures were only 2 °C warmer than preindustrial levels (1880 - 1920). Ignoring these non-linearities is therefore dangerous as they might eventually lead to an impact with an order of magnitude worse than anticipated today.

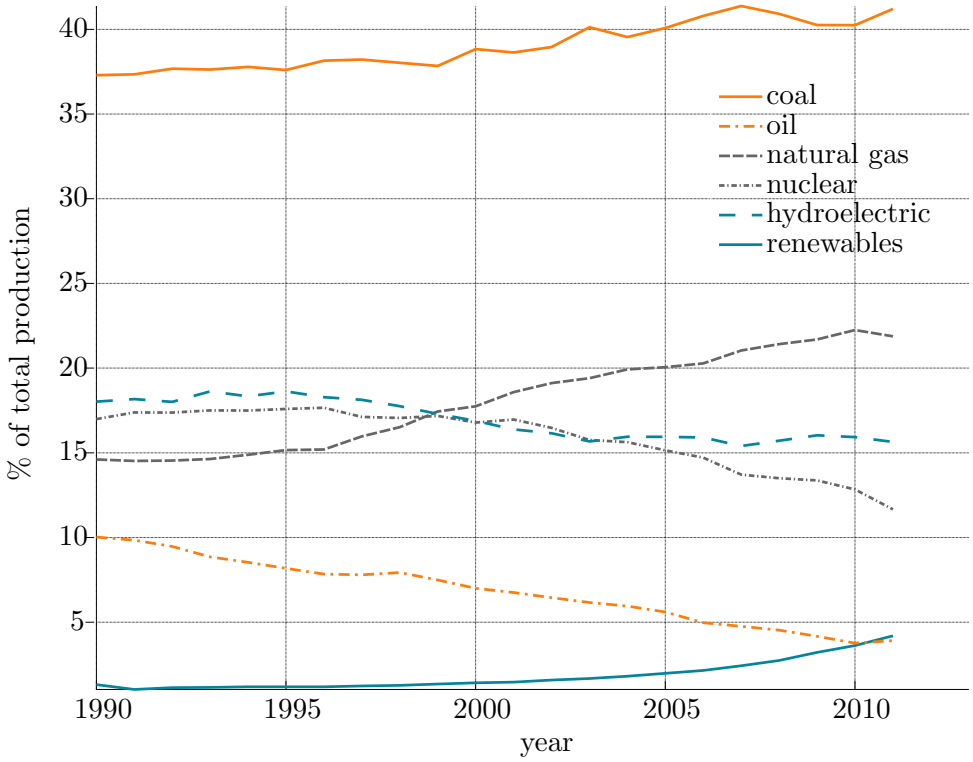

Figure 1.2: Contribution of energy sources to global electricity production [1]

1.1.2 Energy resources

With the clear need of drastic emission reductions established above, the current use of energy sources and the role of renewables is established in this section. According to the World Bank [1], 48.4 % of fuel combustion related emissions were associated with electricity production in 2011. Figure 1.2 shows the relative contribution of different energy sources to global electricity production.

In 2011, about 32 % of global electricity was generated from non-greenhouse gas emitting sources. A remarkable observation is the rise of renewables from an insignificant level before 2000 to 4% in 2010. At the same time the most CO2 intensive source, coal, has increased by a similar amount. In recent years initiatives such as cap-and-trade or a carbon tax have emerged trying to incorporate a cost of emissions into the value of energy and other industry output. Looking at the rise of coal in figure 1.2 however, one can only conclude that on a global scale, such initiatives have had very limited effect. Despite the rise in renewable energy production, it is clearly not sufficient.

Although transition to renewables encompasses a wide variety of topics such as social acceptance, regulatory frameworks, investment climate and electric grid readiness, the main driver is probably cost. A widely adopted cost metric is levelized cost of energy (LCOE) which incorporates all capital expenditures and costs expected during the system's lifetime. It does not take aspects such as dispatchability or storage capability into account.

1.1.3 Wind energy

The LCOE of wind energy based on conventional horizontal axis wind turbines (HAWT) has reduced more than a factor three between 1980 and early 2000s from about $150/MWh to about $50/MWh [15]. The cost reduction has however stabilized with even a slight increase in LCOE since the mid 2000s until 2010 in the U.S. and Europe. Based on a variety of studies, NREL predicts another LCOE drop of about 20%-30% by 2030. In the EIA annual energy outlook 2013 [16], the LCOE of wind is predicted to drop below coal in the US by 2018 but above natural gas. Due to the difference in LCOE and dispatchability between renewables and natural gas, no significant increase in share of energy production is expected in the coming decades in the US [16]. Although the lack of dispatchability is a fundamental aspect of wind energy, a breakthrough in LCOE for wind power could enable a competitive energy production when combined with energy storage solutions.

1.2 Airborne Wind Energy

Airborne wind energy (AWE) is a relatively new idea of harvesting wind energy using tethered airborne vehicles. Compared to HAWT, two key advantages can be identified. First, the structural efficiency of the system is potentially larger as the principal reaction force is carried by a tension member (referred to as tether) instead of a bending member (the tower). Secondly, airborne structures could operate at higher altitudes where wind power densities are significantly higher and more persistent over time. Archer and Caldeira [17] determine that on average, the global power density for median winds (available >50% of the time) increases with 125 W/m^2 per 100m between 80m and 500m altitude. To put this number in perspective, a wind site rated Class I (best wind resources) according to the IEC 61400-1 norm has a annual mean wind speed of 10m/s at hub height which corresponds to a density of about 600 W/m^2. It should be noted that similarly to low-altitude wind resources, the higher altitude power densities vary widely in time and location. At even higher altitudes, local median wind can reach power densities as high 10-15 kW/m^2 around 8-10km [17] but these altitudes seem out of reach for current AWE systems.

A wide variety of concepts exist ranging from hovering rotors [18] to lighter than air balloons with integrated turbines. More examples can be found in an excellent reference work for AWE theory and examples, recently published by Ahrens, Diehl and Schmehl [19]. Multiple research groups and companies are developing systems using flexible kites and a ground based winch. Notably, the Kite Power group at Delft University of Technology has developed and tested a 20kW demonstrator. A kite is flown roughly parallel to the prevailing wind and generates tension in the tether. By allowing the tether to reel out off a drum, connected to a generator, the system generates electrical power. After a specified time, the kite is positioned in a low lift orientation and reeled back in s small amount of power after which the cycle repeats. These two modes of operation are shown in figure 1.3 obtained from van der Vlugt et al. [2].

Other examples using a similar concept include the Swiss Kite Power research project [20] and the companies Skysails [21] and KiteGen Research[22]. A different concept using a rigid wing and on-board turbines is being developed by the company Makani Power, recently acquired by Google Inc. which is discussed in greater detail in section 2.1 as it is the subject of this research.

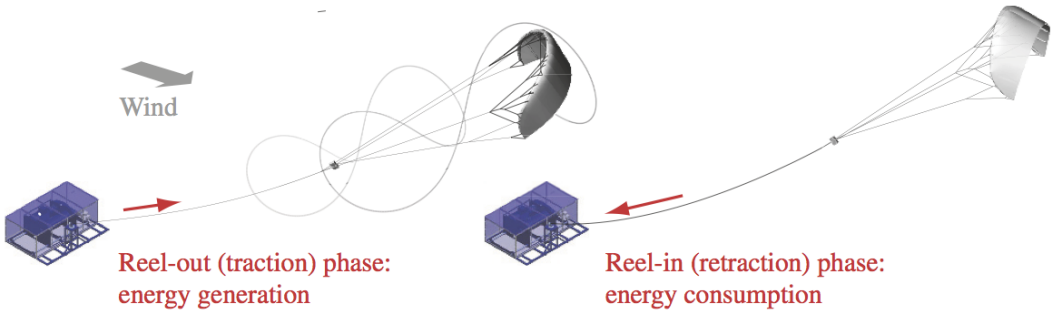

Figure 1.3: KitePower system of Delft University of Technology [2]

1.3 Research goals and structure

This thesis is targeted at airborne wind turbines being developed by Makani Power. As the project is moving from prototype development to commercial systems, detailed understanding of a wide range of design variables is required to make cost-effective decisions. The main goal of this thesis is to develop a system-level analysis tool which allows investigation of the impact of a wide variety of engineering design variables. Although ideally the impact on system cost would be investigated, the scope is narrowed to expected power output which is a large driver in system LCOE. The *impact* is quantified as the sensitivity of power output to a design variable, i.e. as the change in power output due to a change of design variable.

In order to compare the results of the analysis with internal knowledge at Makani Power, an existing prototype system is chosen, called *Wing7* which is discussed in detail in section 2.1. If the approach proves successful on this system, the same analysis tool can then be used for future systems with only system specific changes to the model.

The central research question in this thesis is formulated as follows: "Which design variables affect the Wing7 airborne wind turbine power output the most and how much?". Since the work in this thesis is not focussed on system scaling, "power output" is understood as normalized to the system's rated power. As such, the sensitivities should reflect a change in capacity factor of the system but will be expressed in terms of power. Based on literature and consultation with Makani, aerodynamic lift and drag coefficient and wing mass are investigated. Some design implications will be discussed but are deliberately kept general as it is not the key focus of the research.

A secondary point of interest is the influence of the physical path itself. As the real world trajectory is controlled using a reference trajectory, this can be considered a design variable. Currently, Makani uses circular reference trajectories which are easy to implement. A comparison between optimized and circular trajectories should reveal whether it is worth implementing non-circular reference trajectories. Additionally, a comparison between circular and figure-eight trajectories should be made as it significantly affects the complexity of the tether and ground station design.

The report is structured in the following way. In chapter 2 the available literature is reviewed, which shows that analytic theory provides a solid foundation to investigate a

range of design variables. It is however limited in complexity and relies on quasi-steady analysis on predefined flight trajectories. The approach presented in this thesis tries to overcome these limitations by using a more complex flight dynamics model and trajectory optimization. Suitable modeling, optimization and sensitivity analysis methods for this approach are also reviewed in chapter 2.

Chapter 3 presents the approach taken to answer the research question. As many components work together to finally determine the sensitivities, is a recommended chapter prior to reading any subsequent ones.

In chapter 4 the modeling strategy for each subsystem of Wing7 is discussed which leads to the derivation of the equations of motion in chapter 5. The derivation is strongly based on the work of Gros and Diehl [23].

Chapter 6 formulates the optimization cost function, constraints and bounds. The numerical optimization strategy from Horn and Diehl [24] is used. This is implemented in the open source software code *Rawesome* [25]. Their numerical method and implementation is crucial in enabling the work in this thesis and is described in detail in appendix C. Furthermore in chapter 6, the results of the optimization are discussed and compared with analytical theory.

The results of the sensitivity analysis for lift, drag, wing mass, path circularity and topology are then discussed in chapter 7. Finally in chapter 8, the conclusions and recommendations are presented.

2

Literature Review

This chapter presents some analytical background and an overview of the relevant literature for the thesis. Firstly, section 2.1 explains the working principle and main components of the Makani Power Wing7 system. The basic physical principles and modeling techniques for AWT flight dynamics, aerodynamics and the tether are covered in section 2.2. The core of the review is presented in section 2.3 which discusses the role of trajectory optimization in the field of AWE and the available numerical techniques for solving this class of problems. Since numerical experiments will be performed to obtain sensitivity information, a brief discussion on sensitivity analysis and design of experiments methodology is covered in section 2.4. Finally, the review is concluded and the proposed research is motivated in section 2.5.

2.1 Makani Power Wing7 system

This thesis will focus on a system being developed by Makani Power [7]. As it is the seventh design iteration of their airborne wind energy systems, the system under consideration is called Wing7. It is a 23kW demonstrator system designed to prove the concept and provide a testing planform. It consists of the following main components:

- Rigid wing with a wing span of 8m. The wing is constructed primarily out of carbon fibre composites.
- Vertical and horizontal tail. Similar to a traditional aircraft, the tail surfaces provide stability in flight.
- Aerodynamic control surfaces: flap, ailerons, elevator and rudder. These surfaces are used to control the lift and attitude wing.
- Tether. A high-strength fibre cable connecting the wing to the ground station. It also contains an electrical conductor which allows transmitting electrical power to and from the wing.

- Bridles. Three bridle lines, attached at different locations on the span, connect the wing with the tether, thereby relieving the bending moment in the wing.
- Power system. Consisting of four sets of turbines, generators and motor controllers which can fulfill their function in two directions: (a) convert wind energy into electrical power and (b) convert electrical power in propulsive or hover power.
- Ground station. The ground station transmits the tether tension to the ground while allowing the required rotational degrees of freedom for the wing operation. It furthermore provides a landing platform for the wing when parked. The tether is in that case reeled onto a drum.
- Flight computer, sensors and communications. The wing is flown fully autonomously using a flight controller and a variety of sensors such as a pitot tube, inertial measurement unit and global positioning system. Communications to the ground are provided using both the tether and a wireless system.

Due to the topological resemblance, the wing is often referred to as a kite. Although the Makani Wing7 is flexible to a certain degree, it is orders of magnitude more rigid than kites based on fabric material. Throughout this document the word *kite* is used to refer to both flexible and rigid aerodynamic surfaces generating lift and drag forces, tethered to the ground. The word *wing* is used exclusively for "rigid" structures.

Figure 2.1 shows Wing7 parked on the ground station. From this position, the wing can lift off, hovering like a helicopter, slowly reeling out the tether which is wound on the ground station drum. Electric power is consumed in this stage which is provided to the on-board motors and propellers generating the required hover thrust. Once the tether is reeled out to full length, the wing makes a *transition-in* maneuver and starts flying roughly circular crosswind trajectories. A composite picture of such a trajectory is shown in figure 2.2. In this flight mode, the wing is propelled by the available wind energy using the principle of crosswind (see section 2.2.1). The generated thrust is absorbed by the on-board turbines and generators and fed through the tether to the ground.

As long the prevailing wind speed is high enough, the system can operate continuously, i.e. no retraction phase as in figure 1.3 is required. In case the wind speed is too low or too high, the wing will *transition-out* back to hover mode and land on the ground station.

All stages, i.e. take-off, transition-in, crosswind, transition-out and landing are autonomously controlled using the on-board flight computer, sensors, motors and control surfaces.

Figure 2.1: Makani Power Wing 7 in take-off and landing position

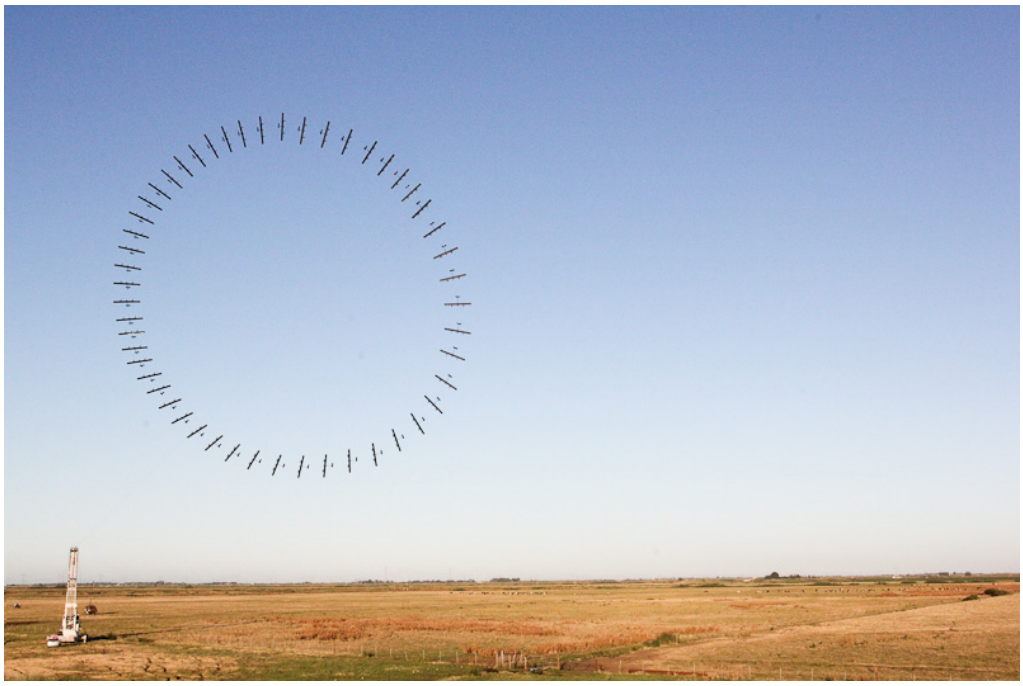

Figure 2.2: Composite picture of Wing 7 in crosswind

2.2 System modeling

This section reviews the available techniques to model airborne wind energy systems and subsystems. As the thesis will focus on optimization, an important aspect for the models is computational efficiency and suitability of implementation in such a framework. The field is introduced in section 2.2.1 by briefly reviewing the available analytical techniques and classifying various airborne wind energy concepts. Since trajectory optimization will eventually require a dynamic model of the kite, the available techniques are reviewed in section 5.2. Subsequently the various methods of aerodynamic modeling are reviewed in section 2.2.3. The last section 2.2.4 briefly covers modeling of a major subsystem, the tether.

2.2.1 Analytic models and classification

In many aspects Miles L. Loyd [26] provided the basis for airborne wind energy (AWE) concepts and preliminary studies. He indicates two global categories of airborne wind turbines (AWT), a so called *simple* kite and a *crosswind* kite. Simple kites rely on the working principle that the tether holding the kite, remains in a fixed orientation with respect to an inertial frame of reference. The kite generates tension in the tether which is used on the ground to for example propel a vehicle. In the second case, called crosswind, the kite is flown roughly parallel to the tether and the airspeed is increased above the local wind speed. The resulting power that can be extracted using this method is many times larger than the simple kite principle. Within the crosswind category, Loyd makes a distinction between *lift power* and *drag power* relating to the mode of power extraction. Lift mode uses the tension in the tether to create useful work, also denoted with *traction kite power*. In drag mode, the work is extracted from the apparent airspeed using on-board turbines and is referred to as *on-board generation*.

Another difference can be made in the structural difference between kites. Although Loyd initially investigated the use of a rigid aircraft in [26], multiple concepts using flexible lightweight kites have arisen since like the Kitegen [5] and Laddermill [27]. Table 2.1 shows various airborne wind turbines classified according to working principle and structural topology. As will become clear throughout the rest of this chapter, most academic interest lies with lift based power extraction systems.

Traction kite power

In traction kite power, energy is extracted from the system by allowing the kite to pull and reel out a tether attached to a generator unit on the ground. Figure 2.3, obtained from [3], shows the free body and kinetic diagram of a massless kite in crosswind using the lift power mode. The kite velocity $\boldsymbol{V}$ combined with the local wind speed $\boldsymbol{w}$ and the tether reel-out speed $\boldsymbol{V}_{out}$ results in the apparent velocity $-\boldsymbol{V}_a$ on the kite. The resulting tension at the ground multiplied with the tether reel out velocity is the power which can be absorbed by the generator. After a certain time, the kite is *de-powered*, i.e. positioned in a low lift and drag position and the kite is reeled back in, consuming a small amount of power after which the cycle repeats. The net difference is the power harvested by the system. This system is also often referred to in literature as a pumping cycle.

Table 2.1: Examples of the various modes of AWT concepts. Top left: Kitegen [5], Lower left: Ampyx power [6] Lower right: Makani Power [7]

[-]	traction	on-board
flexible kite		not available (only for on-board power supply)
rigid kite	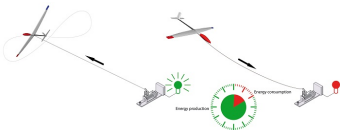	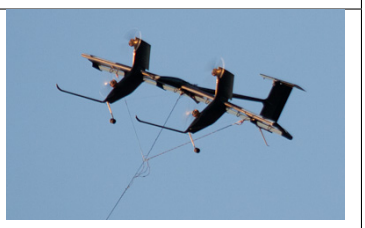

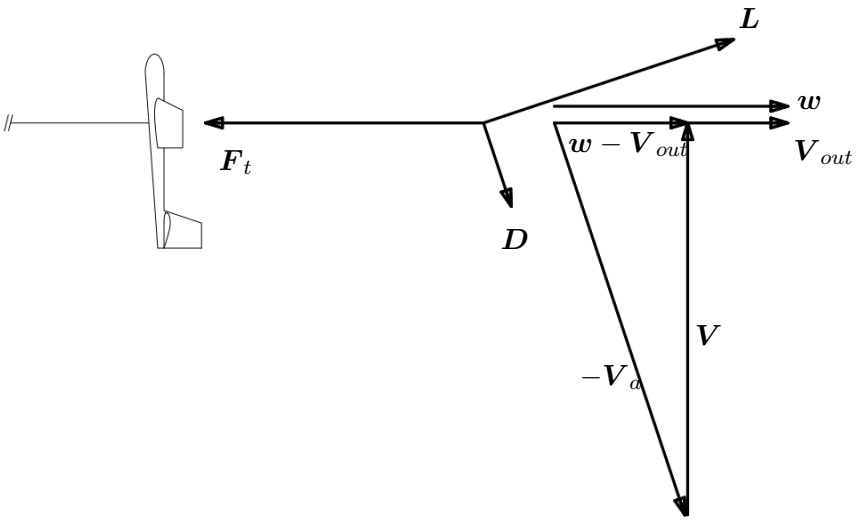

Figure 2.3: Free body and kinetic diagram of a massless kite in crosswind mode [3]

For the reel out phase, Loyd derives the following relation for maximum power absorption:

$$P_{max} = \frac{2}{27}\rho w^3 A \frac{C_L^3}{C_{D,k}^2} \tag{2.1}$$

which occurs at $V_{\text{out}} = \frac{1}{3}w$. Where A is the kite planform area, C_L is the kite lift coefficient and $C_{d,k}$ is the kite drag coefficient. In order to compare different analytical theory, the power harvesting factor ζ is defined as:

$$\zeta = \frac{P}{\frac{1}{2}\rho w^3 A} \tag{2.2}$$

Which in the case of Loyd becomes $\frac{4}{27}\frac{C_L^3}{C_{D,k}^2}$. This result indicates that contrary to a traditional aircraft, the optimality metric for the lifting surface is $\frac{C_L^3}{C_D^2}$ not $\frac{C_L}{C_D}$.

The simple analysis above is useful to analyze basic AWE principles but ignores the effect of mass, gravity, line angle with respect to the wind direction, tether drag and system inefficiencies. In [28], Argatov develops analytical theory for a pumping system to account for these effects and a closed form expression for maximal power extraction at a point along a figure-eight trajectory. In an numerical example of a large (500 m^2) and light (850 kg) pumping system, Argatov concludes that the effect of centrifugal force, gravity and tether friction (i.e. parallel to the tether) affect the output power less than 1%. This observation should be treated with care as the assumed L/D ratio of 37.5 of the kite is extremely large compared to typical real world kites which have a L/D ratio around 5 [29].

In [30] Schmehl et al. present a quasi-steady theoretical analysis of a traction system in power generation, vehicle towing and lifting application. Closed form expressions are derived for instantaneous power output of a pumping power system using a general kite in crosswind. In order to include the effect of gravity and inertial forces an iterative approach is proposed to obtain the correct kinematic ratio of the system. Based on this analysis, they conclude that kite mass reduces the mean generated power impact over a closed loop trajectory and imposes limits on the reel out factor of a pumping system.

On-board kite power

In on-board kite power, a generator is positioned on the kite which generates power by the generation of a drag force using for example propellers, denoted with $C_{D,prop}$. The tether length is usually fixed and the generated electricity is fed through the tether to the ground. Loyd [26] shows that in theory the optimal generated power occurs when $C_{D,prop} = \frac{1}{2}C_{D,k}$ and is again equal to:

$$P_{max} = \frac{1}{2}\rho V_w^3 A \frac{C_L^3}{C_{D,k}^2} \tag{2.3}$$

In [31] Vander Lind expands the theory of on-board systems to include the effect of azimuthal and elevation angle. Furthermore, he introduces a technique to include the effect of tension and power constraints of the system where equation 2.3 is corrected using the metric:

$$\tau = \frac{F_t w}{P} \tag{2.4}$$

which describes the generated power relative to the force in the tether. For the unconstrained case as shown in equation 2.3, $\tau = 3$.

2.2.2 Flight dynamic analysis

The goal of a flight dynamics model is to predict the time evolution of the position and attitude of the kite and it's subsystems. A major factor in determining a suitable model is the *rigidity* of the kite. The main effect of structural deformation is not on the dynamic properties of the kite (e.g. inertia tensor, internal damping) but the change in aerodynamic loading. This fluid body interaction is a complicated topic which for the most accurate results would require coupling of computational fluid dynamics with a structural finite element code. The work of Breukels [32], offers a different approach where the flexibility of the kite is modeled using multi-body dynamics combined with interpolation on an aerodynamic surrogate model, calculated in advance. However, even for flexible kite systems, the most common assumption in literature is that the kite can be modeled as a rigid body (e.g. [33, 24]). As the Makani system structurally resembles more an aircraft than a kite it is orders of magnitude more rigid and using this assumption seems reasonable. Undesired aeroelastic properties like flutter and aileron reversal are still of importance but can be implemented by limiting the flight envelope in the optimization. Different methods of deriving the equations of motion assuming a rigid body are discussed below.

De Groot et al. [34] derive the equations of motion for a rigid body kite by directly applying Newton's second law using Euler angles and spherical coordinates. This is a common approach for aircraft flight dynamics models which is expanded to include the tether forces and moments around the center of gravity. The tether is modeled as a straight spring-damper without mass or aerodynamic drag.

A frequently used method to derive the equations of motion is the Lagrangian framework. Equation 2.5 shows the core of the Lagrangian theory where $\mathcal{L}$ is the Lagrangian of the system (difference between kinetic and potential energy), $\boldsymbol{q}$ are the generalized coordinates, $\dot{\boldsymbol{q}}$ the generalized velocities, λ_k the Lagrange multiplier associated with the constraint f_k and $\boldsymbol{Q}$, the generalized forces. A more elaborate explanation of the Lagrangian formalism can be found in [35]

$$\frac{d}{dt}\left(\frac{\partial \mathcal{L}}{\partial \dot{q}_j}\right) - \frac{\partial \mathcal{L}}{\partial q_j} + \lambda(t)\frac{\partial f_k}{q_j} = Q_j \tag{2.5}$$

Both Houska and Diehl [36] and Williams [37] use this formalism to derive equations of motion which are subsequently used for optimization. The complexity of such derivation

largely depends on the number of degrees of freedom and constraints and the choice of how to represent rotations between coordinate systems. A distinction should be made here between *minimal* and *non-minimal* coordinates. Minimal coordinates use the same number of generalized coordinates as degrees of freedom in the system to represent them. A classical example are Euler angles to represent a rotation of a rigid body, where each rotational degree of freedom is represented by an angle.

A good example of a flight dynamics model using minimal coordinates is the work of Terink et al. [33] where the authors derive a five degree of freedom model of a tethered inflatable kiteplane. The position of the kite center of mass is represented using three spherical coordinates. Rigid body rotations are modeled using two angles for two degrees of freedom, where the yaw and roll motion are coupled through the bridles. This coupling assumes the bridles to act as a revolute joint. The resulting equations of motion are numerically solved and used to perform a stability analysis of the kiteplane. Terink shows the final expressions for equations of motion for the system in [38] which are long but easy to derive using a symbolic math toolbox.

Although minimal coordinates are conceptually the easiest to use, they suffer from certain drawbacks [23]:

- Minimal coordinates often appear nonlinearly in the dynamics which makes symbolic representation complex which is often necessary to derive the equations of motion from the Lagrangian formalism. Additionally, symbolic representation is required for automatic differentiation tools (e.g. CasADi [39]).
- Projections of one reference frame into the other requires nonlinear transformations (sines, cosines).
- Euler angles have singularities which could prove a problem as the kite could have a wide range of orientations.

Non-minimal coordinates use more generalized coordinates than the number of degrees of freedom and require additional constraints during integration to guarantee the representation remains correct. In [40], Gros derives a 6 degree of freedom (DOF) model using quaternions which require 4 states to describe a rotation in $\mathbb{R}^3$. Quaternions do not suffer from singularities but the resulting equations are still more non-linear compared to another technique called a *direction cosine matrix* (DCM) [23].

In [23] Gros uses such a DCM to represent the rotation between the kite and inertial reference frame. A DCM for a rotation in $\mathbb{R}^3$ is a 3×3 matrix where each component represents the cosine of the angle between the corresponding unit vectors in the different frames. Appendix A discusses this concept in more detail. Using a DCM results in 9 generalized coordinates to describe 3 degrees of freedom which results in an over-determined system. By using the property that any rotation matrix has to be orthogonal, the correct shape of the DCM can be enforced as a constraint. Although using a DCM results in six additional equations compared to Euler angles, the resulting set of equations is significantly less nonlinear.

2.2.3 Aerodynamics analysis

The purpose of an aerodynamic model is to determine the forces and moments on the kite as a function of its geometry, control surface deflection and orientation w.r.t. the apparent wind. As analytic solutions to accurately determine the flow field around such a structure are unavailable, numerical techniques are often employed to obtain the solution. A trajectory optimization algorithm will likely require hundreds or even thousands of iterations to reach an optimal solution, each requiring aerodynamic analysis of a full trajectory. Current state of the art aerodynamic codes require solution times in the order of minutes to even days depending on the complexity of the flow and required accuracy. In light of a reasonable time to obtain an optimal solution, direct computation at each step is therefore not feasible.

A widespread technique to deal with this issue is by analyzing the aerodynamic response in advance and approximating the result as a surrogate model which can be evaluated with low computational cost during the optimization [41]. Linearizing the aerodynamic response around a specific operating condition is a common method often referred to as *stability* and *control derivatives*. The resulting response is linear which allows a state space representation of the model. It fails however to address the inherently non-linear nature of aerodynamics in for example the stall regime. Depending on the width of the flight envelope, this technique might be suitable or higher order surrogate models are necessary.

The most high fidelity method to determine the input for surrogate models is to use computational fluid dynamics (CFD) to solve the Navier-Stokes equations. In direct numerical simulation (DNS), the equations are solved from the smallest relevant scales up to the size of the model [42]. Since the computational burden of obtaining such a solution is very large, DNS is typically only used for low reynolds number problems (see [43] for an example). The computational cost can be reduced by modeling the smaller scales using a turbulence model. Discussing the wide variety of models is beyond the scope of this review but it's worth noting the best industry practice. Most modern CFD tools for engineering applications use a Reynolds-averaged version of the Navier-Stokes equations (RANS) with a turbulence model depending on the type of flow problem (e.g. Spalart-Allmaras or k - ϵ). Although the so called Large Eddy Simulation approach in which smaller scales are resolved is becoming more available for detailed analysis, engineering applications for a full 3D-wing is still impossible at the present time [44].

An older approach for aerodynamic analysis is based on panel methods. The computational cost is orders of magnitudes smaller than Navier-Stokes based CFD but since the methods assume potential flow, only specific flow problems can be analyzed. When coupled with boundary layer models to include viscosity effects, these methods have been used successfully for high Reynolds number analysis of complete aircraft geometries [45]. A wide variety of commercial and open source tools is available, e.g. VSAERO [46] or the Athena Vortex Lattice program (AVL) [47].

2.2.4 Tether

A critical question in modeling a kite system is how to represent the tether. The following aspects regarding the tether affect the performance of the system:

- Aerodynamic drag. As the tether sweeps through the air, part of the generated forces on the tether act on the kite and affects its behavior and performance.
- Strength. The strength of the tether determines the maximum tension which can be developed in by the kite
- Stiffness. Even though the tether is not actively reeled out during on-board generation, it will elongate under tension. As the tension typically varies along the path, the stiffness affects the dynamics of the kite.
- Weight. For large systems, the tether mass is in the same order of magnitude as the kite mass. The action of gravity on this mass will affect the balance of forces at the kite and at the ground.
- Inertial effects. Due to the curvature of the flight path, the tether mass will experience accelerations which in turn affect the dynamics at the kite.
- Effect of cable sag. Due to the sag, the effective position of the kite will be closer to the ground station than the instantaneous tether length.

Before reviewing different models it should be noted that contrary to lift-based systems, the drag-based Makani system operates at constant tether length. Furthermore the key point of interest is the resulting force at the kite. Ground side tension is of smaller importance as contrary to traction based systems it is not used to generate power.

In [36], Houska and Diehl estimate the resulting force due to aerodynamic effects at the kite as one fourth of what the drag would be if the entire tether was moving at the speed of the kite, thus:

$$\boldsymbol{F}_{D,t} = -\frac{c_{D,t}\rho A_t}{8}\|\boldsymbol{V}_a\|\boldsymbol{V_a} \tag{2.6}$$

where $c_{D,t}$ is the drag coefficient of the tether referenced to the diameter, A_t the total frontal area of the tether, ρ the air density and $\boldsymbol{V}_a$ the airspeed vector (opposite direction to the apparent wind speed). Furthermore in [36] and [23], the inertial and gravitation effect of the tether is approximated by adding one third and one half of the tether mass to the kite mass respectively. This is a common approach in literature and is based on the assumption of a straight tether allowing analytical integration over the tether length.

Regarding the effect of gravity, more discussion is present in literature. Although the approximation of adding half the tether mass to the gravitational mass of the kite presented above intuitively seems to make sense (center of mass of the kite is positioned in the middle), a more detailed analysis presented by Noom [48] reveals interesting conclusions. He analyzes the case where the tether is inclined with an angle β with respect to the horizon and looks at the tangential and radial components of the gravitational tether force. He concludes that the resulting force experienced by the kite due to tether gravity is

$$F_{\text{k,teth,grav}} = \left[-\sin\beta \boldsymbol{e}_r + \frac{1}{2}\cos\beta \boldsymbol{e}_\theta \right] m_t g \tag{2.7}$$

where $\boldsymbol{e}_r$ and $\boldsymbol{e}_\theta$ represent the unit vectors in radial and tangential direction. In the case where $\beta = 0$, this reduces to the assumption discussed above.

The approximations above assume a straight tether. In reality, the tether will sag as it is unable to transfer bending loads. Sagging due to gravity is a widely studied topic and leads to the catenary equations, which can be found for example in [48].

In order to fully address all the relevant effects without a straight tether assumption, Breukels [49] proposes a multi-body model where the tether is modeled as a series of lumped masses connected by springs and dampers in both translational and rotational direction. In [50], Williams presents a similar lumped mass model for a tether towed by an aircraft flying a circular motion. The model is subsequently used for modal analysis and optimization using the SQP solver SNOPT.

2.3 Trajectory optimization

With the various methods of modeling the kite and subsystems established above, this section proceeds by examining how optimal flight trajectories can be obtained with these models. Trajectory optimization is a subset of a mathematical problem called an optimal control problem (OCP). Various methods of solving an OCP are given in section 2.3.2. In order to get an idea of the problem formulation, performance metrics and relevant constraints, trajectory optimization of AWE systems are reviewed first in section 2.3.1.

2.3.1 Airborne wind energy systems

Unfortunately no work specifically on on-board generation systems was found in literature. Most often the pumping cycle principle is analyzed. Although the method of power generation is fundamentally different for on-board systems, the optimization methodology for traction systems is reviewed as the they are otherwise very comparable.

In [36] Houska and Diehl present an approach to find optimal trajectories for a pumping cycle kite in crosswind. They derive a three degree of freedom model using the Lagrangian formalism with spherical coordinates. The OCP is set up as follows. The optimization objective function is taken to be the average generated power during one cycle. Control inputs of the system are the relieved cable length (reel out acceleration) and the time derivatives of the kite roll angle and lift coefficient. Two type of constraints are applied to a) guarantee periodic flight trajectories, i.e. the path repeats itself after one cycle time and b) the path is physically feasible. The latter includes bounds on control inputs like maximum rate of change of the kite's lift coefficient and bounds on differential states like maximum reel out speed. The OCP is subsequently solved numerically using the MUSCOD-II package which is based on the direct multiple shooting method, further discussed in section 2.3.2. The authors notice that there are many locally optimal solutions

to the OCP, relating to the topology of the path. The topology chosen here is a figure-eight loop which has the advantage that the cable does not wind up after a cycle. This choice is implemented by fixing the *winding number* of the trajectory, which is the degree to which the tether is coiled up after one cycle. By imposing a particular winding number in the form of a periodic boundary condition, the topology of the path can be fixed without predefining the actual shape. A circular loop has a winding number of 1 while a figure-eight has one of 0.

In [24], Horn et al. derive a full six degree of freedom model of a rigid body kite using non-minimal coordinates. The tether is assumed straight and implemented as a constraint. As they use the Lagrangian formalism, the tether force can be found by through the associated Lagrange multiplier. A similar OCP formulation as Houska and Diehl [36] is chosen but is in this case discretized using their own implementation of the direct collocation method. This method is further discussed in section 2.3.2. After discretization, the OCP is solved using the open source solver IPOPT. A method to generate feasible initial guesses is also presented which is based on the augmentation of the equations of motion with pseudo-forces. They further show the capability of the algorithm by computing optimal holding and transition trajectories for an AWT system. Solution times for a pumping system are reported to be between around 30 seconds on a modern desktop computer.

An extensive study on optimization of a pumping kite system was performed by Williams et al. in [37]. Again the equations of motion for a three degree of freedom model are derived using the Lagrange formalism. Since the angle of attack and roll angle are controlled directly (via their rates), attitude dynamics of the kite are essentially ignored. The objective is formulated as to maximize the average power and minimize, with a certain weighing factor, the control effort. The OCP problem is then solved using the Legendre pseudospectral method (see section 2.3.2). This method does not guarantee a global minimum, the best local minimum is chosen after trying a set of random generated initial guesses.

2.3.2 Numerical methods to solve optimal control problems

This section covers various numerical techniques of solving an optimal control problem and is based on the work of Von Stryk and Bulirisch [51]. A wide variety of techniques exist and the list below only covers the most common ones used to solve trajectory optimization problems. An OCP deals with finding the necessary controls of a certain dynamic system such that a certain *cost functional* is minimized. The dynamic system can be formulated as a set of (non)linear differential equations as shown in 2.8, where $x(t)$ represent the system states and $u(t)$ the controls.

$$\dot{x}(t) = f(x(t), u(t), t), \quad t_0 \leq t \leq t_f \tag{2.8}$$

An common performance metric is of a *Mayer type* (in which the functional is reduced to a function), given by equation 2.9, but more general formulations such as a Bolza type are possible. The final time t_f can be fixed or free.

$$J[u] = \Phi\left(x(t_f), t_f\right) \quad \text{with } \Phi : \mathbb{R}^{n+1} \Rightarrow \mathbb{R} \tag{2.9}$$

Most practical problems include constraints on the controls and states, given by 2.10 and 2.11 respectively. The resulting set of m constraints is $g(x(t), u(t), t) = (C, S) = (g_1, ..., g_m)$

$$C(u(t), t) \leq 0, \quad t_0 \leq t \leq t_f \tag{2.10}$$

$$S(x(t), t) \leq 0, \quad t_0 \leq t \leq t_f \tag{2.11}$$

In some cases, an analytic solution of the problem can be obtained but for complex systems like AWT, a numerical method is required.

Indirect methods

Indirect methods are based on the calculus of variations, specifically the Pontryagin principle and explicitly solve the optimality conditions. By formulating the Hamiltonian function of the system, given by 2.12, the problem can be formulated as a multi-point boundary value problem and the relations 2.13 through 2.15 hold.

$$H = \lambda^T f + \nu^T g \tag{2.12}$$

$$\dot{x} = \frac{\partial H}{\partial \lambda} = f \tag{2.13}$$

$$\dot{\lambda} = \frac{\partial H}{\partial x} = -\lambda^T \frac{\partial f}{\partial x} - \nu^T \frac{\partial g}{\partial x} \tag{2.14}$$

$$0 \geq g \tag{2.15}$$

The optimal control is then obtained by minimizing H with respect to u. In case of an nonlinear H in u, the first necessary conditions look as shown in 2.16. Additionally the Legendre-Clebsch condition states that $\frac{\partial^2 H}{u_i u_k}$ should be semi-definite.

$$\frac{\partial H}{\partial u} = \lambda^T \frac{\partial f}{\partial u} + \nu^T \frac{\partial g}{\partial u} = 0 \tag{2.16}$$

Depending on the structure of the problem, certain numerical methods can be used to obtain solutions, for example gradient methods, shooting methods or collocation. Although indirect methods can produce very accurate results, a good initial guess is required. Furthermore, the adjoint equations (eq. 2.14) have to be derived manually which requires a lot of work for large problems.

Direct Methods

Most methods found in literature to solve an OCP are not indirect but *direct* methods in which the problem is transformed into a non linear programming (NLP) statement and then solved. The specifics of the various methods depend on the following:

1. Discretization of the control variables $\boldsymbol{u}(t)$.
2. Integration (quadrature) of the differential states $\boldsymbol{x}(t)$ with the system differential equations and parametrized controls $\boldsymbol{u}(t)$. This can be done using the equations in original form (shooting methods) or by discretizating the states using a finite dimensional form, typically a Legendre polynomial.
3. NLP algorithm. Depending on the formulation above, the NLP can be formulated and a suitable solver can be selected. A variety of open source and commercial NLP solvers are available, e.g. IPOPT [52] or SNOPT [53].

The most common methods for discretizing the OCP are discussed below.

Direct Single Shooting
In direct single shooting only the controls and constraints are discretized. For example the value of $\boldsymbol{u}(t)$ on N grid points with linear interpolation between them. The time history of the controls is now described by a finite number of decision variables which are optimized by NLP algorithm. An ODE or differential algebraic equation (DAE) solver is then used in each step of the NLP algorithm to integrate the state equations and controls simultaneously. The kind of solver depends on the degree of non-linearity and stiffness of state equations but a solver which delivers sensitivities is required as they can in turn be used by the NLP algorithm [54].

Direct Multiple Shooting
Direct multiple shooting is essentially direct single shooting applied on a number of intervals of the time grid. Instead of integrating the ODE over the entire time grid, it is integrated over a section (e.g. the first half of the time grid). Each section of the grid is individually solved using direct single shooting. Without additional constraints, the solution would become infeasible since the end states of a section do not necessarily correspond to the starting states of the subsequent interval. In order to eliminate these so called *defects*, additional equality constraints are added. Direct multiple shooting methods tend to be more robust than single shooting methods and allow parallel processing for some parts of the computation [55].

Direct Collocation
In direct collocation, both the controls and the states are discretized. The first step is to discretize the trajectory in N intervals. Instead of explicitly integrating the equations of motions on each interval i (multiple shooting method), the states are approximated by a interpolating orthogonal polynomial (typically Lagrange or Chebyshev) with degree D and D+1 control points (called collocation points). The shape of the polynomial is determined by the state equations which are applied at the collocation points. If these points in the time domain are chosen as the zeros (roots) of the polynomial, the approximation error can be guaranteed [54].

Pseudospectral method
The pseudospectral method is used extensively in the field of optimal control. Instead of discretizing the trajectory (direct collocation, multiple shooting), the entire state time domain is approximated by a single polynomial with a high degree. Both Legendre and Chebyshev polynomials are often used for trajectory optimization [56]. In order to guarantee a certain degree of accuracy, the nodes of the polynomial have to be chosen according to some Gauss quadrature scheme. These are typically Legendre-Gauss-Lobatto or Chebyshev-Gauss-Lobatto nodes. The system differential equations can then again be applied at the nodes.

A more elaborate explanation of the direct collocation method is provided in appendix C as it is used in this thesis. The next section continues with how the output of the optimization algorithm can be used to determine sensitivities.

2.4 Sensitivity analysis

In literature the term 'sensitivity analysis' is used for many purposes. In the field of empirical research, it is used to for example measure the effect of small changes in an empirically obtained data set on the predicted correlation based on this set. The field of optimization often refers to sensitivity analysis as a method to obtain gradient information of a certain mathematically defined problem. In the context of this research, sensitivity analysis is understood as a way to quantify the effect of a change of a variety of parameters like design variables on a performance metric. This metric is in this case not the objective of the trajectory optimization but a compounded one measuring the performance over a range of wind speeds (later defined in section 3.3.1).

2.4.1 Definition and methods

In [57], Smith explains various kinds of sensitivities. The *absolute sensitivity* of a function F to a change in the parameter α is defined as given in equation 2.17 in which the subscript NOP refers to normal operating point.

$$S_\alpha^F = \left.\frac{\partial F}{\partial \alpha}\right|_{\text{NOP}} \tag{2.17}$$

An absolute sensitivity is a partial derivative of the function to a certain parameter. It is important to note that higher order derivatives can reveal interactions between different parameters. Non-zero higher order derivatives can also reveal quadratic, cubic, etc., dependencies of the function to a certain parameter. Absolute sensitivities can be used to estimate the resulting function value by evaluating the computed sensitivities at a certain distance away from the NOP. It is important to realize that even though the sensitivities can in some cases be computed exactly, evaluating them at a distance away from the NOP always introduces a certain error.

Another type of sensitivity is *relative sensitivity* which is useful for comparing the effect

of different parameters. The definition is given in equation 2.18.

$$\bar{S}_\alpha^F = \left.\frac{\partial F}{\partial \alpha}\right|_{\text{NOP}} \frac{\alpha_0}{F_0} \approx \frac{\%\text{ change in } F}{\%\text{ change in } \alpha} = \frac{\frac{\Delta F}{F}}{\frac{\Delta \alpha}{\alpha}} \tag{2.18}$$

Relative sensitivities can be used to find for example the largest change in function value with the minimum relative change in parameter value. Again, higher order sensitivities can reveal interactions between various parameters. Finally, the *semirelative sensitivity* is defined as given in equation 2.19 which can also be used to compare the effect of different parameters since the absolute sensitivity is scaled with the value of the parameter in the NOP.

$$\tilde{S}_\alpha^F = \left.\frac{\partial F}{\partial \alpha}\right|_{\text{NOP}} \alpha_0 \tag{2.19}$$

Often in complex models, sensitivities cannot be determined analytically. Instead they are often approximated by performing numerical experiments and subsequent analysis.

Estimation of sensitivities using numerical experiments

The basic idea is to perform a series of (numerical) experiments and use some form of statistical method like linear regression to find a relation between input and output data. Since the experiments can be computationally expensive with complex models a lot research has been done to obtain an accurate fit of the output with a minimum number of experiments. In [58], Kleijnen gives an overview of various methods, some of which are discussed briefly below. These methods are often referred to as *design of experiments* (DOE). Before discussing a few of these methods, it's important to mention that most of them use no information contained in the model, i.e. they're pure statistical methods to correlate input and output of the model. Kleijnen refers to this as considering the model as a black box.

In the field of engineering, probably the most often used and at the same time most criticized method is the *one factor at a time* (OFAT). As the name suggests, every experiment involves changing one factor with a certain level and calculating the change of the function value. Their can be multiple levels for each factor but only one parameter at a time is changed. The main critique on this method is that is neglects a potential correlated effect of factors. Depending on the purpose of the sensitivity analysis, this assumption might or might not be justified. If for example the purpose is to construct an accurate response surface of complex model with a large set of variables, assuming that none are correlated is probably wrong. If on the other hand the sensitivity analysis is only used to roughly estimate the impact of a certain variable, a quick OFAT analysis can suffice. If in the case of an OFAT analysis the performance metric, i.e. the output of the model is a single value, usually simple linear or higher order regression techniques are used to 'fit' the input to the output. The order determines the required levels of the factors under investigation and thus influences the number of experiments.

DOE which includes the effect of correlation between factors changes multiple factors at the same time to include their interaction. The most known method of this kind is a *factorial* experiment in which all possible correlations are experimentally checked. As an example, taken from Kleijnen [58], we look at a problem with three variables, $k = 3$,

each having 2 different levels. The number of experiments in a factorial experiment is then $2^k = 2^3 = 8$. Subsequently all eight parameters of the metamodel, i.e., fit, given by equation 2.20 can be solved using statistical techniques like least-squares.

$$\mathbf{y} = \beta_{\mathbf{0}} + \sum_{\mathbf{j=1}}^{\mathbf{3}} \beta_{\mathbf{j}} \mathbf{x_j} + \sum_{\mathbf{j=1}}^{\mathbf{2}} \sum_{\mathbf{j'>j}}^{\mathbf{3}} \beta_{\mathbf{j;j'}} \mathbf{x_j x_{j'}} + \beta_{1;2;3} \mathbf{x_1 x_2 x_3} \tag{2.20}$$

A disadvantage of factorial designs is that a lot of experiments are required. Alternative methods requiring less experiments like fractional designs are available but are not discussed here for the sake of brevity.

2.4.2 Sensitivity analysis for AWE systems

Williams et al. [37] use their trajectory optimization framework to determine various sensitivities like cycle time, tether length, kite area, kite mass and shape of the wind profile to average power output of pumping cycle system. The used methodology to determine these effects is not explicitly mentioned but is essentially an OFAT analysis where a single parameter is modified while keeping the others at the baseline level.

Canale et al. investigate the optimal power output of a pumping cycle and carousel AWE system as a function of kite area and efficiency, wind speed and cable length [59]. Again an OFAT method was used but the tether was sized according to the tension loads in the tether. As the sensitivity to tether mass and is high, including this effect is crucial to get the sensitivity of a realistic system. It should be mentioned that this is a different approach than taken by Houska et al. in [36], who as discussed in section 2.3.1 actually *optimize* the tether diameter, i.e. a flight path with lower tension in the tether might be more optimal.

2.5 Summary & Research motivation

From the literature study presented above, two global approaches for system level performance modeling of AWE systems can be identified. On the one hand, a quasi-steady approach such as the ones presented by Loyd [26], Argatov [28] and Noom [48] allows analytic modeling of the kite performance using a predefined trajectory.

On the other hand, dynamic simulation and optimization of the AWT trajectories allows analysis without a predefined trajectory and does not require quasi static assumptions. Examples of this approach are given by Houska and Diehl [36], Horn et al. [24] and Williams et al. [37].

An interesting observation is that all design variable studies using trajectory optimization focus on a single wind speed. From a design perspective a single windspeed is a rather poor metric. The long term performance of any wind harvesting device is determined by the power output for a range of wind speeds and wind speed probability at the wind site.

Predicting a full power curve using dynamic simulation and optimization has not been found in literature, probably due to the high computational cost of this approach. However, recent advancements in trajectory optimization focussed on AWE systems, are expected to dramatically decrease the solution time. Notably the implementation of the direct collocation method by Horn et al. [24] seems promising. In combination with a rigid body model with low nonlinearity developed by Gros et al. [23] this has led to the open source software code Rawesome.

This thesis aims at using this tool to provide an answer to the research question:

Which design variables affect the "Wing7" airborne wind turbine power output the most and how much?

In order to provide Makani Power with relevant results, the entire wind speed regime will be investigated. The resulting design variable sensitivities will reveal possible design improvements and can be used in design tradeoffs. Furthermore, the resulting optimization framework can be used for development of future systems and analysis of the flight path.

No work on optimization of on-board generating systems is present in literature. Although from a modeling and optimization standpoint they are less challenging due to the fixed tether length, the field of AWE as a whole will benefit from research on such a system.

3

Computational approach

With a suitable modeling and optimization approach selected in section 2.5 the overall approach is discussed here. The goal is to determine how much certain design variables affect the power generation of the Makani Wing7 system. An overview of the components and working principle were given in section 2.1. This will be reached through the following steps:

1. Derive the equations of motion of the wing using the Lagrangian framework. This part is strongly based on the work of Gros et al. in [23] with the only differences lying in how the tether and bridle is treated and the addition of propeller drag.
2. Derive the necessary equations for the on-board power system. They should determine the electric power output of the system at the ground side of the tether as a function of some control variable for each of the four power plants. The resulting drag generated by the propeller is an input for the equations of motion.
3. Compute the optimal trajectory and resulting power output at a certain wind speed. This will be done using the Rawesome software code developed by Horn [25] using the direct collocation method developed by Horn et al. [24].
4. Repeat step 3 for a sufficient range of wind speeds to interpolate a power curve of the system (see figure 3.5).
5. Compute the performance metric using the power curve and wind speed probability at the chosen site, defined in section 3.3.1.
6. Repeat steps 3 to 5 for a range of changes to the baseline design involving one design variable (following the OFAT methodology).
7. Analyze the results and calculate the sensitivity near the baseline. Discuss nonlinearity.

Steps 1-5 are visually shown in figure 3.1 to further clarify the approach.

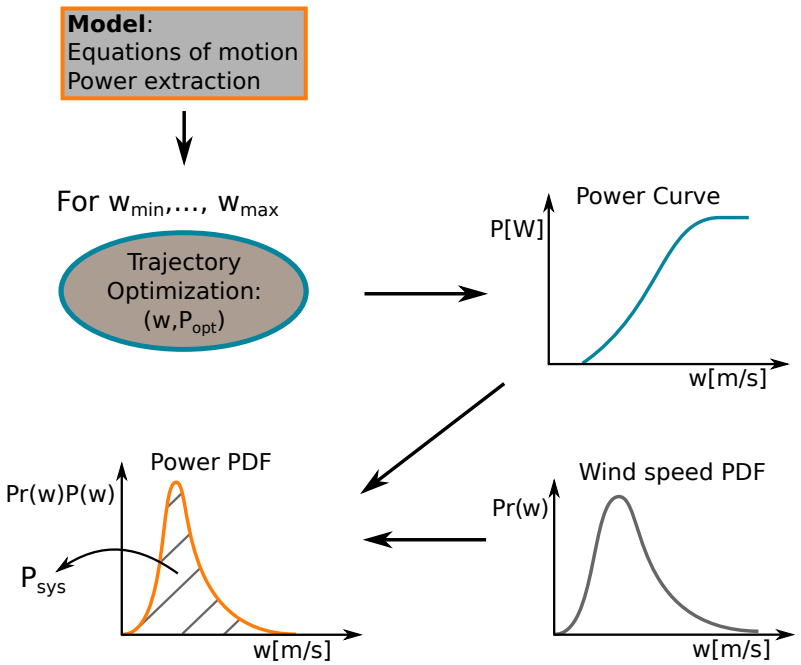

Figure 3.1: Overview of the steps to compute the performance metric P_{sys}. PDF refers to probability density function.

3.1 Modeling approach

Since low nonlinearity is desired for the optimization, the work from Gros et al. will be used to derive the equations of motion. The resulting equations are very similar to their model shown in [23]. The only difference is that the tether will not be implemented as a constraint and propeller drag is added. The wing will be treated as one rigid body with constant mass m_k and inertia $\boldsymbol{J}$, six degrees of freedom and the following external forces and moments:

- Tether force of time-varying magnitude and direction. The moment arm of this force around the kite center of mass is determined by the bridle system and is also time dependent.
- Aerodynamic forces and moments as a function of the airspeed vector, body rotational rates and control surface deflections.
- Propeller drag or thrust. Four forces and their resulting moments around the center of gravity. The magnitude of the four forces are independent and determined by the power system model discussed below.

Figure 3.2 shows these forces and the coupling with the power system model.

The power system will be modeled as four identical instances of the same sub-model with independent input and control variables. The sub-model consists of a series of power conversion elements which are also shown in figure 3.2:

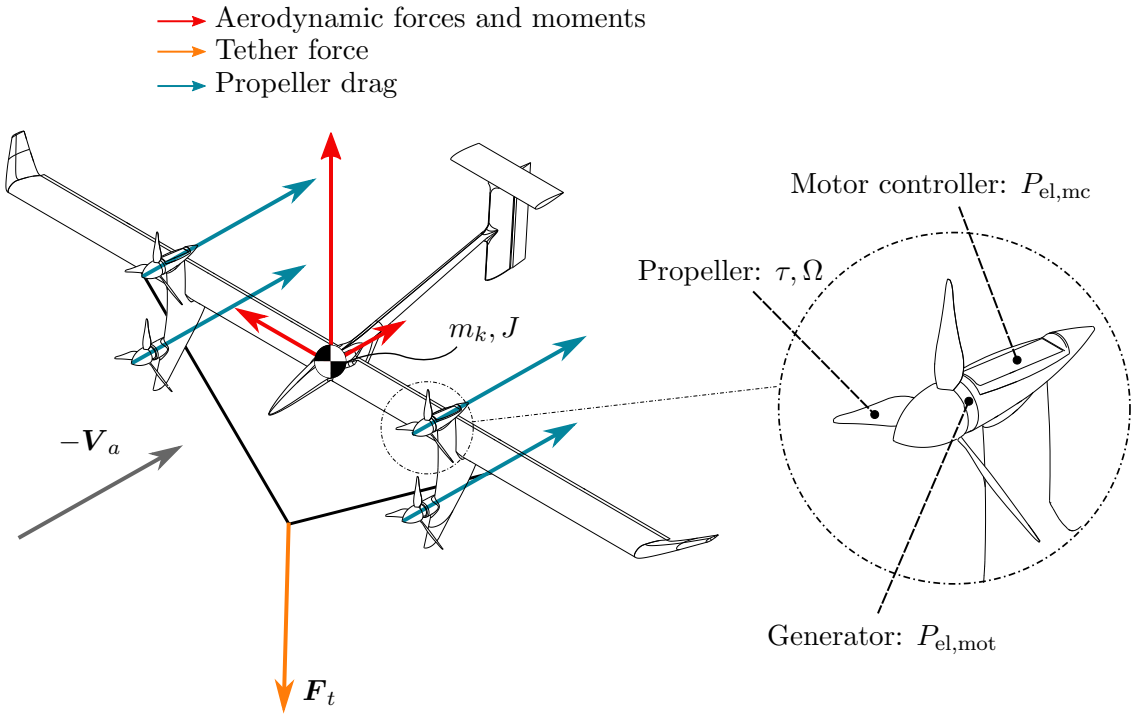

Figure 3.2: Illustration of the modeling approach. (left) Rigid body model of the wing with external forces. (right) Power system model. Not shown: electrical tether model

- The propeller model will determine the resulting shaft torque τ and rotational velocity Ω as a function of the *local* airspeed at the propeller plane and a control variable. This will be done by constructing a surrogate model on the output of an analysis tool XROTOR which is built on the work of Drela [60].
- Using the mechanical output τ, Ω of the propeller, the generator model determines the electrical generator power output $P_{\text{el,gen}}$. An analytical DC-equivalent motor model with fixed torque limit is used while ignoring any thermal characteristics.
- The motor controller is modeled as a power conversion device with a fixed efficiency and power limit.
- The electrical tether (not shown in figure 3.2) is modeled as a power conversion device with a fixed efficiency.

The resulting electrical power at the ground side of the tether, denoted with $P_{\text{el,teth}}$ will be the key component in the cost function of the optimization, discussed in the next section.

3.2 Trajectory Optimization

The next part (step 3 in the list at the beginning of this chapter) is to determine the optimal power output for a specific wind speed and a specific design configuration. The chosen optimization strategy is taken from Horn et al. [24] which was implemented by Horn in an open source software tool *Rawesome* [25]. The tool can solve a wide range of optimal control problems but was written with AWT applications in mind. Rawesome offers a custom implementation of a discretization method called Direct Collocation and a set of interfaces to other open source tools. Overall, Rawesome combines the strength of a powerful NLP solver, an automatic differentiation (AD) framework and a custom discretization method to obtain a fast and robust tool. Figure 3.3 shows the sequence of these steps.

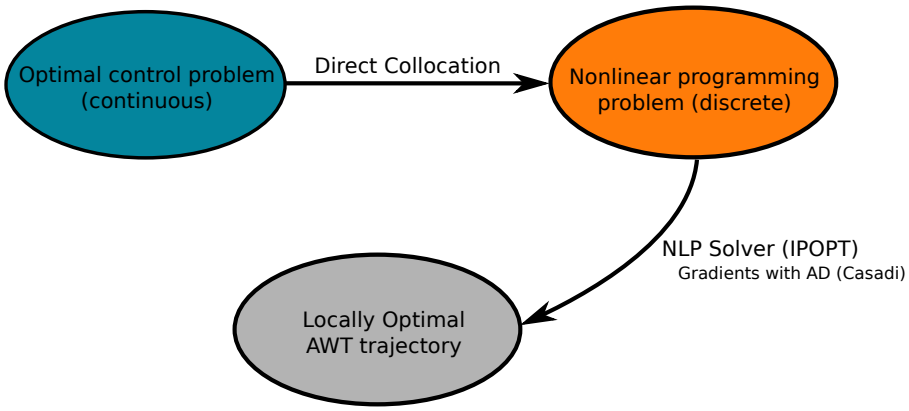

Figure 3.3: Elements of the optimization method as used by Rawesome

Central to the optimization process is the direct collocation discretization method which was briefly explained in literature review (section 2.3.2). Since this thesis does not present any contribution to this method, it is not explained in detail here. However, the interested reader is encouraged to review this piece as it is crucial in enabling the work in this thesis. A detailed explanation can be found in appendix C. The key steps of the method are listed below:

- Discretize the parametrized time domain in N intervals. In this thesis, N=40 is used for circular trajectories and N=60 for figure-eights.
- Assume a certain control variable discretization on each interval. A constant value is used in this work.
- Approximate the states on each interval by a Lagrange interpolating polynomial with degree D leading to $D+1$ *collocation nodes*. The nodes must be chosen carefully to obtain accurate quadrature integration. A polynomial with D=4 and Gauss-Radau quadrature scheme was used.
- Apply the equations of motion at the collocation nodes by formulating a constraint equating the analytic derivative of the polynomial with the relevant equation of motion. This is shown visually in figure 3.4.

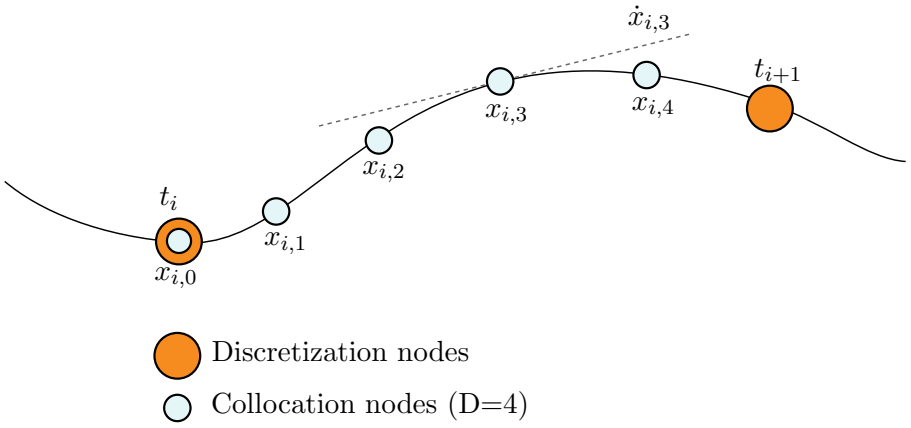

Figure 3.4: State trajectory discretization using collocation: the shape of the polynomial is fixed by imposing the model equations as the polynomial derivative (dotted line) at the collocation nodes

- Equate the final state of interval i (obtained using quadrature integration) to the initial state of interval $i+1$ (which is the first collocation node of that interval) for $i = 1, \ldots, N$ This allows direct integration over the entire time domain.

3.2.1 Initial guess

The NLP solver does not guarantee to find the global minimum of the solution space. The local optimum is a strongly influenced by the supplied initial guess which is required to start the optimization. Since the states are parameterized as a polynomial, successive iterations will "deform" the initial trajectory. The potential shape of the optimal solution is very broad but will be very likely topologically *homotopic* to the initial guess. In topology two functions are said to be homotopic if they can be continuously deformed into one another. The crucial parameter for the trajectories here is the *winding number* N which is the degree to which the physical trajectory is coiled up after one cycle (earlier discussed in section 2.3.1). A circular trajectory has $N = 1$, while a lemniscate has $N = 0$. Although any N in between results in a real class of trajectories (see [36] for examples), they are not periodic. With periodic boundary conditions in the optimization, feasible trajectories of $N = 0$ and $N = 1$ are thus not homotopic. Although the NLP algorithm will also (potentially) evaluate infeasible solutions during convergence, the violations are usually small such that there is no guarantee to "jump" from a trajectory with $N = 1$ to $N = 0$ or vice versa.

As the Makani power system is built with $N = 1$ in mind, a range of circular initial guesses were provided to the optimization and the best solution chosen. The generation of initial guesses was done using the method described by Horn et al. [24] by augmenting the equations of motion with *pseudo forces* which are step by step reduced to zero in sequential optimizations. This is explained in more detail in section C.3 of appendix C.

Since the choice for a particular winding number is an interesting design variable, the effect was studied in section 7.4. A Lissajous figure as used by Noom [48] was chosen as an initial guess for the $N = 0$ trajectories.

3.3 Design variable sensitivity analysis

The optimal power output of the trajectory optimization can now be used to investigate the effect of certain design variables on power output.

3.3.1 Performance metric

As a performance metric the long term power generation P_{sys} of the system is chosen, i.e. the average power which the system would generate if it would operate continuously for an infinite time. P_{sys} is defined as:

$$P_{\text{sys}} = \int_{w_{\text{cut,in}}}^{w_{\text{cut,out}}} P_{\text{el,teth}}(w)\text{Pr}(w)\text{d}w \tag{3.1}$$

where $P_{\text{el,teth}}(w)$ refers to the generated power at the ground side of the tether at a certain windspeed. This is represented using a power curve. Figure 3.5 shows a generic power curve with the definitions of the cut-in $w_{\text{cut,in}}$, rated w_{rat} and cut-out wind speed $w_{\text{cut,out}}$. $\text{Pr}(w)$ in equation 3.1 is the probability density function of the prevailing wind speed at "hub" height at a certain site, discussed in section 4.7

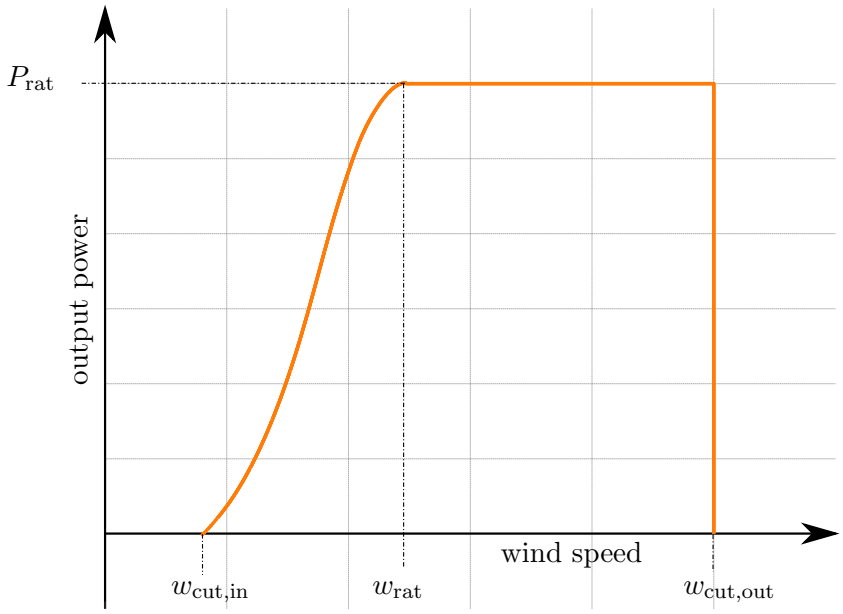

Figure 3.5: Generic power curve with the definition of $w_{\text{cut,in}}$, $w_{\text{cut,out}}$, w_{rat} and P_{rat}

The power curve, including $w_{\text{cut,in}}$ and w_{rat} is determined by successive trajectory optimization runs and interpolation. The spline interpolation function in the software package Matlab is used on data points spaced 0.5 ms^{-1} apart between $w_{\text{cut,in}}$ and w_{rat}. The cut-out windspeed is fixed at 25 m/s.

Furthermore, the rated power P_{rat} of the system is fixed through the power constraint imposed at the motor controllers in the power system. A difference in power output

between different levels of a design variable will thus only be caused by a difference in capacity factor.

All operational and maintenance aspects are ignored such that the system is always assumed to operate on it's power curve. This includes the following assumptions:

- No launch, landing and transition sections of the flight
- No downtime due to maintenance or (un)expected failure
- No degradation of system performance over time
- No losses from conversion to grid power

Furthermore, the system is assumed to:

- Not operate in a power-consuming region of the power curve, i.e. power generation for wind speeds below the cut-in wind speed is assumed zero.
- Provide constant power generation between rated wind speed and cut-out wind speed, i.e. this assumes the system can be de-powered without affecting maximum power.

The resulting metric P_{sys} thus only captures the power-generating operation of the system. Sensitivities to this metric therefore do not represent sensitivities to the global design optimum.

3.3.2 Sensitivity definition

Sensitivities are expressed as *absolute sensitivities* (see section 2.4) of P_{sys} and are defined as:

$$S_{\alpha}^{P_{\text{sys}}} = \left.\frac{\partial P_{\text{sys}}}{\partial \alpha}\right|_{\text{NOP}} \tag{3.2}$$

where NOP refers to the baseline value of design variable α.

Absolute sensitivities are expected to be the most valuable for the client, Makani Power. For example, the sensitivity to system mass, measured in $[W/kg]$ can directly be compared with for example the sensitivity to wing drag in $[W/C_D]$. Since the performance metric is subject to a large number of assumptions listed above, the interpretation of the absolute value of sensitivities should be done with care. However, since most design variables are not expected to influence those assumptions much, the main added value of the sensitivities will be in comparing them. Using the example above, the ratio between the two sensitivities, expressed in $[kg/C_D]$ can directly be used (keeping in mind the limitations!) in numerous design trade-offs such as wing root thickness.

In order to compare the relative impact of design variables, *semirelative sensitivities* will be used, defined as:

$$\tilde{S}_{\alpha}^{P_{\text{sys}}} = \left.\frac{\partial P_{\text{sys}}}{\partial \alpha}\right|_{\text{NOP}} \alpha_0 \tag{3.3}$$

The OFAT method will be used with k levels for each design variable α. The resulting set $\left\{\alpha^{1,\ldots,\mathrm{k}}, P_{\mathrm{sys}}^{1,\ldots,k}\right\}$ is used to fit a 2nd order polynomial $p(\alpha)$ with coefficients $\{p_0, p_1, p_2\}$ using least squares:

$$p(s) = p_2\alpha^2 + p_1\alpha + p_0 \tag{3.4}$$

The local sensitivity $\frac{\partial P_{\mathrm{sys}}}{\partial \alpha}(\alpha)$ is approximated as the derivative of the polynomial:

$$\frac{\partial P_{\mathrm{sys}}}{\partial \alpha}(\alpha) \approx 2p_2\alpha + p_1 \tag{3.5}$$

and will be given for all computed levels in order to show the degree of nonlinearity. The value of the sensitivity $S_\alpha^{P_{\mathrm{sys}}}$ is then approximated as:

$$S_\alpha^{P_{\mathrm{sys}}} \approx 2p_2\alpha_0 + p_1 \tag{3.6}$$

4

AWT System definition

With the general approach discussed in chapter 3, this chapter covers the first steps towards a mathematical model of the Wing7 system. In section 4.1, the various reference frames are presented. Section 4.2 covers how the aerodynamic response of the wing is modeled. After a short discussion on the ground station in section 4.3, the tether and bridle models are presented in sections 4.4 and 4.5. Finally, in section 4.6 the power extraction system including propellers, generators, motor controllers and the electrical tether is discussed.

4.1 Reference frames

In order to express different aspects of the model, various reference frames are used. All reference frames use natural coordinates, i.e. cartesian x-y-z coordinates, and rotations between them are expressed by means of a direction cosine matrix (see appendix A for a detailed explanation about DCM's).

An inertial, earth fixed reference frame E_E is chosen such that the origin coincides with the ground station. The X_E-axis is aligned with the direction of the prevailing wind (a particle carried by the wind will move in positive x-direction), the Z_E-axis downward and the Y_E-axis using the right hand rule. The inertial frame is depicted in figure 4.1. The position of the kite center of mass in the E_E frame is indicated with $\boldsymbol{r}^E$.

A body frame of reference E_B is chosen in accordance with aircraft conventions, i.e X_B-axis pointing forward, Y_B-axis in the direction of the starboard wing, Z_B-axis according to the right hand rule. The origin of E_B is however the same as the E_E frame. The body reference frame is fixed with respect to the wing's geometry, as if the axis were painted on the body but displaced to the ground station. This allows expressing the wing's moment of inertia tensor $\boldsymbol{J}$ as a time invariant parameter. An alternate reference frame $E_{\overline{B}}$ is defined to indicate the E_B frame displaced to the wing center of gravity since some variables make more sense when expressed w.r.t. the wing center of gravity. Figure 4.1 shows the E_B and $E_{\overline{B}}$ reference frames in the same figure as the inertial frame E_E.

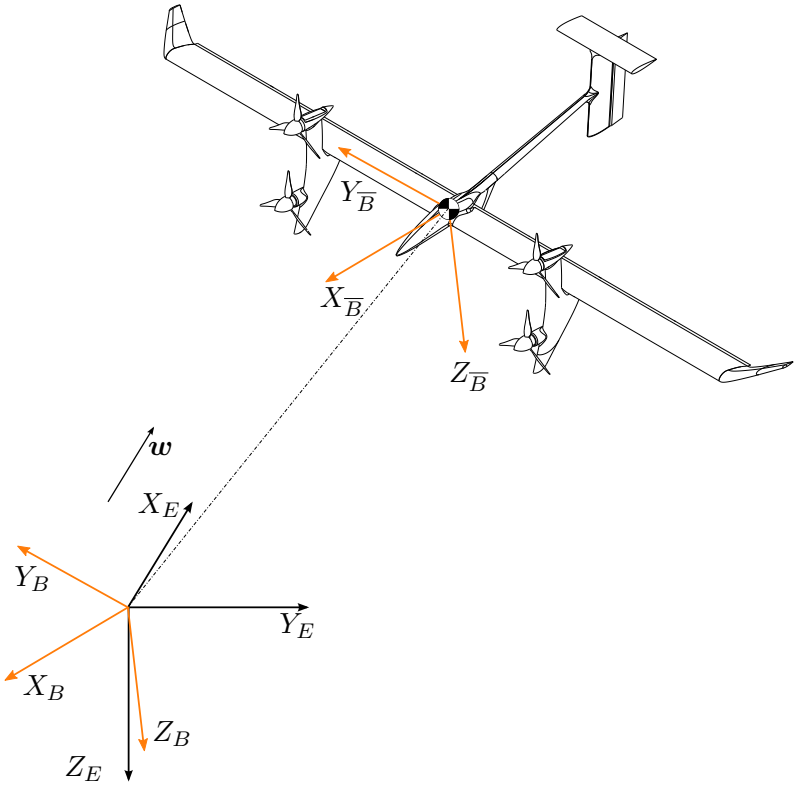

Figure 4.1: Earth-fixed and body reference frame

The rotation matrix required to rotate a vector in E_B to E_E is indicated with $\boldsymbol{R}_{EB}$ such that:

$$\boldsymbol{r}^E = \boldsymbol{R}_{EB}\boldsymbol{r}^B \tag{4.1}$$

As aerodynamic forces of a body are often expressed with respect to the apparent airflow, an aerodynamic reference frame E_A is used. It's origin is the same as the $E_{\overline{B}}$ frame, the centre of mass. The positive X_A-direction in the direction of the apparent wind, i.e. a drag force is positive, the Z_A-axis positive upward, i.e. a lift force is positive, and the Y_A-axis according to the right hand rule. Figure 4.2 shows the aerodynamic frame and the body frame. The airspeed vector $\boldsymbol{V}_a^B$ can be found as

$$\boldsymbol{V}_a^E = \boldsymbol{V}^E - \boldsymbol{w} \tag{4.2}$$

$$\boldsymbol{V}_a^B = \boldsymbol{R}_{BE}\boldsymbol{V}_a^E \tag{4.3}$$

were it should be noted that the airspeed vector is defined in the opposite direction than the apparent wind speed vector (but same magnitude). The angle of attack α and side slip angle β can be obtained from the airspeed vector using expressions 4.4 and 4.5 (in correspondence with Etkin [4])

$$\alpha = \tan^{-1}\frac{V_{a,z}^B}{V_{a,x}^B} \tag{4.4}$$

$$\beta = \sin^{-1}\frac{V_{a,y}^B}{\|\boldsymbol{V}_a^B\|} \tag{4.5}$$

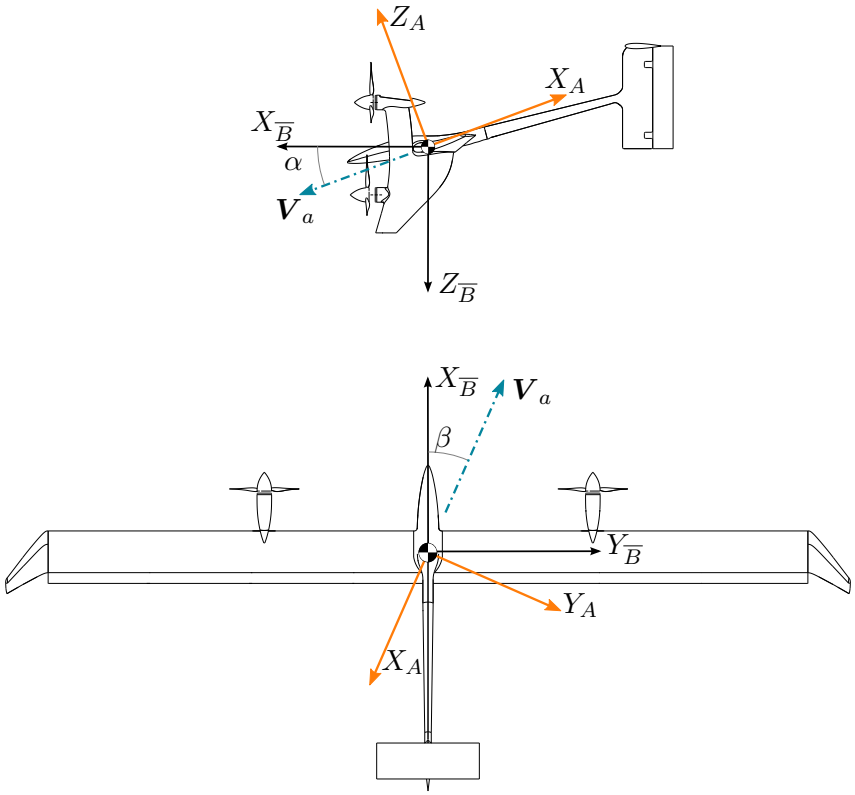

Figure 4.2: Body fixed and aerodynamic reference frame

4.2 Aerodynamics

The interaction of the wing with the air is probably the most important aspect of the entire model. As discussed in section 2.2.3, an external aerodynamic analysis tool called Athena Vortex Lattice (AVL) is used. AVL is a vortex lattice method which computes aerodynamics forces and moments by representing each lifting surface as a vortex sheet. Each vortex sheet is discretized into a finite number of horseshoe filaments in chord and span wise direction. Using the Biot-Savart law, the induced velocities due to all horse shoe vortices can be computed for each panel thereby approximating induced drag. Although AVL is an inviscid method, 2D airfoil data such as the $C_L - \alpha$ curve and lift drag polar can be set for each panel. These can obtained by 2D airfoil analysis including viscous effects. Control surfaces can be defined which allows computation of control derivatives.

An AVL model of Wing7, including viscous 2D data, was available at Makani Power and was priorly used successfully for simulation purposes. The output of the analysis was used to fit a polynomial response surface of the relevant stability and control derivatives, discussed separately in the following sections.

4.2.1 Stability coefficients and derivatives

Stability coefficients and derivatives describe the forces and moments response of the wing at a certain state with respect to the apparent wind. The first order states are

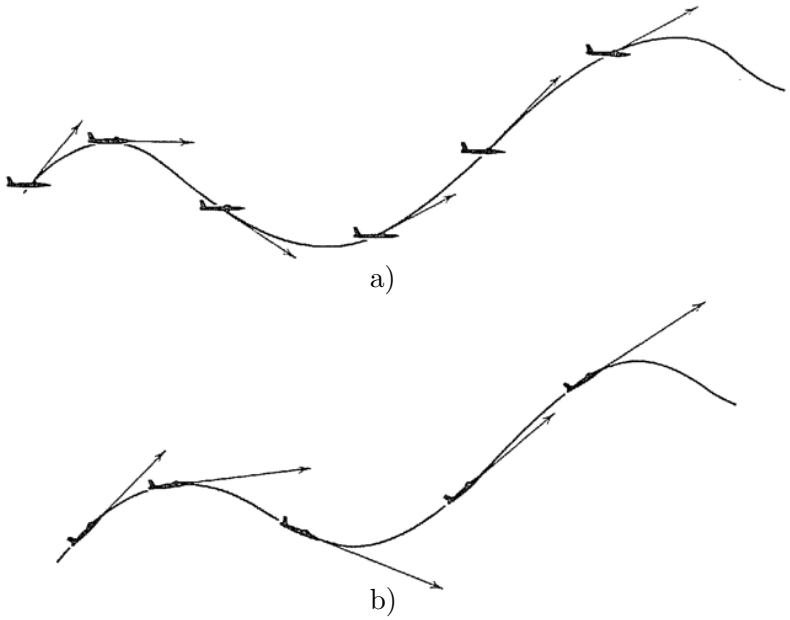

Figure 4.3: Identical flight path with a) $q = 0$ and $\dot{\alpha} \neq 0$ and b) $q \neq 0$ and $\dot{\alpha} = 0$ [4]

the angle of attack and sideslip α, β. As these angles change, the generated forces and moments change. In a completely linearized model, this effect would be captured in a single coefficient, often called a *stability derivative*. Since the range of operating conditions varies significantly along the trajectory and with wind speed, a linearized model would be too crude. Instead all coefficients are directly computed as a function of α and β. The required order to accurately fit the surrogate model to the AVL output was determined manually for each coefficient. Equation 4.6 shows all possible terms (up to order 3) in this case for C_Z as an example. For most coefficients, using both the linear terms proved sufficient.

$$C_Z(\alpha, \beta) = a_0 + a_1\alpha + a_2\alpha^2 + a_3\alpha^2 + a_4\beta + a_5\beta^2 + a_6\beta^3 + a_7\beta\alpha + a_8(\beta\alpha)^2 \tag{4.6}$$

The second order effects are the force and moments response as a function of the time rate of change of states. A distinction has to be made between change in aerodynamic rates $\dot{\alpha}, \dot{\beta}$ and body rates p, q, r. As shown in figure 4.3 (taken from Etkin [4]), depending on the flight maneuvers, either one or the other could be dominant. Since the AWT will mostly change its trajectory while keeping angle of attack constant, the response to $\dot{\alpha}, \dot{\beta}$ is ignored.

Ignored effects: In [4], Etkin describes the change of coefficients as a function of airspeed. This effect is attributed to change in Mach number and structural deformation under different aerodynamic loading. As the airspeeds are in the low subsonic regime, the effect of Mach number (and thus the change in) can be safely ignored. Aeroelastic deformations could have a significant effect on certain maneuvers but are ignored as discussed in section 2.2.2.

It's important to note that although all stability derivatives are modeled nonlinear in α and β they are assumed to be constant with respect to the body rates. For example, the

effect of a change in pitch rate q on the longitudinal moment coefficient C_m, denoted with C_{m_q} is modeled as a function of alpha α and β, i.e. $C_{m_q}(\alpha, \beta)$ but assumed independent of q itself. Therefore, these higher order contributions can be coined and computed as a *derivative*. An identical surrogate model as for the first order coefficients was used to capture the effect of the change in the value of the derivative with respect to α and β as shown in equations 4.7. Finally, the contribution of the pitch rate q to the moment coefficient C_m is computed using eq. 4.8.

$$C_{m_q}(\alpha, \beta) = b_0 + b_1\alpha + b_2\alpha^2 + b_3\alpha^2 + b_4\beta + b_5\beta^2 + b_6\beta^3 + b_7\beta\alpha + b_8(\beta\alpha)^2 \tag{4.7}$$

$$C_m(q) = C_{m_q}\hat{q} \tag{4.8}$$

Since pitch rates are relatively small along the trajectory, the assumption of using a linearized rate dependency would be justified. As yaw rates are very high, this does no necessarily hold for derivatives like C_{X_r}. However, as the wing is expected to fly circular trajectories, the *change* in yaw rate is expected to be small. Instead of including the yaw rate dependency of the stability coefficients, a linearization point with representative yaw, pitch and roll rates was chosen in AVL. Besides body rates, the linearization point also includes an elevator deflection such that the wing is trimmed in pitch.

All rate related derivatives are computed using non-dimensional rates, indicated with a hat, according to equations 4.9 through 4.11.

$$\hat{p} = \frac{pb}{2V_a} \tag{4.9}$$

$$\hat{q} = \frac{qc}{2V_a} \tag{4.10}$$

$$\hat{r} = \frac{rb}{2V_a} \tag{4.11}$$

In reality, every change in aerodynamic state has an effect on all the forces and moments. For the sake of simplicity, only the major contributions were included, shown in table 4.1. All coefficients are expressed in the body frame of reference E_B with the center of gravity as a reference point.

4.2.2 Control derivatives

Control derivatives describe the change in forces and moments due to a control input. Wing7 has five aerodynamic control surfaces, similar to a conventional aircraft as shown in figure 4.4. The two ailerons primarily control the wing in roll but can collectively be used as a flap to control the effective camber and thus lift of the wing. In high wind conditions this can be used to de-power the wing by deflecting upward. A rudder and elevator are used to control the yaw and pitch orientation of the wing.

The same approach as described in 4.2.1 was used to generate the control derivatives. Again a representative operating condition was modeled in AVL and the output used to generate a polynomial response surface to express the value of control derivatives as a function of α and β. The same fitting function as in equation 4.6 is used. Table 4.2 shows the implemented derivatives.

As the propeller thrust/drag can be actively controlled, their response could be expressed as a control derivative. Instead they are treated separately in section 4.6.

Table 4.1: Implemented coefficients and stability derivatives in order of importance for each force/moment

Symbol	Descritpion
$C_X(\alpha, \beta)$	Effect of α and β on C_X (longitudinal force)
C_{X_r}	Effect of yaw rate r on C_X
$C_Y(\alpha, \beta)$	Effect of α and β on C_Y (side force)
C_{Y_r}	Effect of yaw rate r on C_Y
$C_Z(\alpha, \beta)$	Effect of α and β on C_Z (vertical force)
$C_l(\alpha, \beta)$	Effect of α and β on C_l (roll moment)
C_{l_p}	Effect of roll rate p on C_l
C_{l_r}	Effect of yaw rate r on C_l
$C_m(\alpha, \beta)$	Effect of α and β on C_m (pitch moment)
C_{m_q}	Effect of pitch rate q on C_m
C_{m_r}	Effect of yaw rate r on C_m
$C_n(\alpha, \beta)$	Effect of α and β on C_n (yaw moment)
C_{n_r}	Effect of yaw rate r on C_n
C_{n_p}	Effect of roll rate p on C_n

Table 4.2: Implemented control derivatives in order of importance for each force/moment

Symbol	Descritpion
$C_{X_{\delta r}}$	Rudder input on C_X (longitudinal force)
$C_{Y_{\delta r}}$	Rudder input on C_Y (side force)
$C_{Z_{\delta f}}$	Flap input on C_Z (vertical force)
$C_{Z_{\delta a1}}$	Aileron 1 input on C_Z
$C_{Z_{\delta a2}}$	Aileron 2 input on C_Z
$C_{l_{\delta a1}}$	Aileron 1 input on C_l (roll moment)
$C_{l_{\delta a2}}$	Aileron 2 input on C_l
$C_{m_{\delta e}}$	Elevator input on C_m (pitch moment)
$C_{n_{\delta r}}$	Rudder input on C_n (yaw moment)
$C_{n_{\delta a1}}$	Aileron 1 input on C_n
$C_{n_{\delta a2}}$	Aileron 2 input on C_n

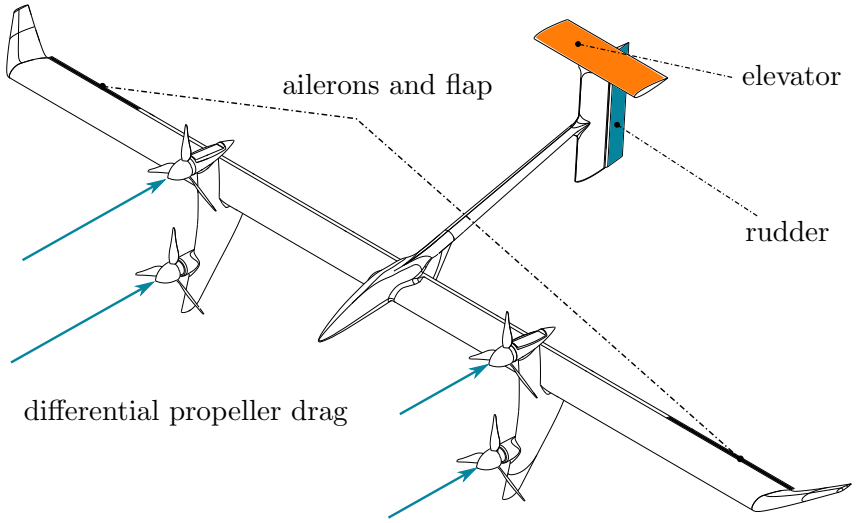

Figure 4.4: Aerodynamic control surfaces on Wing7. Differential propeller drag drag shown for completeness (not treated as a control derivative)

4.3 Ground station

Although the actual ground station is a quite complex system, it is modeled as spherical joint without friction or inertia. As the kite changes its elevation in the sky, the tether is free to rotate around a bearing with virtually no inertia. On a change of azimuthal location in the sky, the ground station rotates about the vertical axis to realign the tether force with the main bearing axis. If the ground station had no inertia around this axis and the elevation bearing was located in the main bearing centre, it would act exactly as a spherical joint. Due to ground station inertia and the offset of the elevation bearing the instantaneous center of rotation of the tether end point slightly shifts along the loop. Compared to a tether length of around 140m, this change in offset is very small and is discounted in the model. From an energy point of view, rocking the ground station inertia back and forth requires some energy which has to be generated by the kite. With a few simple assumptions the energy loss without friction is computed in table 4.3. The resulting loss is about two orders of magnitude lower than the electric power generated by the wing so is safe to neglect.

4.4 Tether

Instead of modeling the tether as a body with it's own degrees of freedom, each relevant aspect of the tether is modeled separately and added to the equations of motion directly or through generalized forces. The tether is idealized as a straight, elastic element with mass (split up in inertial and gravitational effects) interacting with the air. In this section, the relevant length $l_{\text{tot}}$is the total length of the tether and bridle system which will be defined later.

$$l_{\text{tot}} = l_t + l_{\text{br}} \tag{4.12}$$

Table 4.3: Ground station energy loss computation

Description	Symbol	Value	Units
Input			
total azimuthal width of cone	θ_{cone}	20	deg
cycle time (time to complete one loop)	t_c	4	s
gs inertia around azimuthal (vertical) axis	$I_{zz,gs}$	550	kgm^2
Output (assuming sawtooth rotational velocity profile)			
gs mean azimuthal rotational velocity (per 1/2 loop)	$w_{az,mean}$	± 10	deg/s
gs peak azimuthal rotational velocity	$w_{az,peak}$	± 20	deg/s
gs angular acceleration	α_{gs}	$\pm$ 20	deg/s^2
gs torque: $\alpha_{gs}/I_{zz,gs}$)	T_{gs}	$\pm$ 192	Nm
energy loss: $2T_{gs}\theta_{cone}$)	E_{loss}	134	J
Power loss (T_{gs}/t_c)	P_{loss}	33.5	W

The bridles are assumed to have the same linear density in the direction of the tether and the same aerodynamic drag per unit length as the tether.

Inertial mass and aerodynamic loading

The effect of inertial mass is approximated as in [23, 40] by considering the kinetic energy stored in the moving tether. Using the straight tether assumption, the velocity of an infinitesimal element dl at a distance s from the ground station is $\frac{V}{l_{\text{tot}}}s$. The kinetic energy of the tether can then be found as:

$$T_{\text{kin,teth}} = \int_0^{l_{\text{tot}}} \frac{1}{2}\mu_t \frac{V^2}{l_{\text{tot}}^2} s^2 ds \tag{4.13}$$

with μ_t the linear density of the tether and thus $m_t = \mu_t l_{\text{tot}}$ it follows that:

$$T_{\text{kin,teth}} = \left[\frac{1}{6}\mu_t \frac{V^2}{l_{\text{tot}}^2} s^3\right]_0^{l_{\text{tot}}} \tag{4.14}$$

$$= \frac{1}{6} m_t V^2 \tag{4.15}$$

and thus one-third of the tether mass can be added to the kite mass when stating the kinetic energy of the system referenced the kite velocity $\boldsymbol{V}$.

A similar approximation is made to determine the aerodynamic loading on the tether. Again, using the straight tether assumption, the airspeed of an infinitesimal element dl at a distance s from the ground station is approximated as $\frac{V_a}{l_{\text{tot}}}s$. Since the wind speed does not scale linearly with s, this introduces an error, especially near the ground. Considering the fact that the airspeed is dominated by the kite velocity and that the error is small near the kite (where the airspeed is highest) the total error is expected to be small. The tether is a symmetric round element so no other forces than a drag force are present. The distributed loading on the tether is:

$$q = \frac{1}{2}\rho d_t C_{d,t} \frac{V_a^2}{l_{\text{tot}}^2} s^2 ds \tag{4.16}$$

Using the result of Noom [48], the fraction of the force, acting on the kite is then:

$$F_{\mathrm{D,teth}} = \frac{1}{l_{\mathrm{tot}}} \int_0^{l_{\mathrm{tot}}} \frac{1}{2} \rho d_t C_{d,t} \frac{V_a^2}{l_{\mathrm{tot}}^2} s^3 ds \tag{4.17}$$

$$= \frac{1}{8} \rho d_t C_{d,t} l_{\mathrm{tot}} V_a^2 \tag{4.18}$$

with $C_{d,t}$ the tether drag coefficient referenced to its diameter d_t and ρ the density of air, all assumed constant. Examining equation 4.18, the aerodynamic effect of the tether can thus be included by adding 1/4th of the tether drag to the kite drag.

As the tether cannot carry bending moments, no resulting moments arising from the inertial or aerodynamic loading are transmitted to the wing. In reality, the tether will deform under the loading such that no bending moment is present and thereby (slightly) rotate the direction of the tension force. In the straight tether assumption it is assumed that this rotation is equal to adding a tangential (fictitious) force at the kite. This argument also holds for the tangential component of the gravitational pull on the tether, discussed below and shown in figure 4.6.

Additionally, it is assumed that the tangential components due to inertial and aerodynamic loading attach in the kite center of gravity and thus do not introduce a moment. Since both these forces are small compared to the total tension, the introduced error on the rotational dynamics is expected to be small.

Gravity

As discussed in section 2.2.4, a suitable model to represent the effect of gravity on the tether was given by Noom [48], repeated in equation 4.19

$$F_{g,t} = m_t g \left[(-\sin\beta) \boldsymbol{e}_r + (\frac{1}{2}\cos\beta) \boldsymbol{e}_\theta \right] \tag{4.19}$$

The coordinate system $\{\boldsymbol{e}_r, \boldsymbol{e}_\theta\}$ is later shown in figure 4.6.
It is important to consider the effect of pre-tension in the tether. For a typical AWT, the tension in the cable is dominated by the aerodynamic loads on the wing. The effect of tether gravity should therefore be superimposed on this pre-tension. As long as the tension is bigger than the radial gravity component in the tether, the only effect of this component is a tension reduction at the ground side of the tether. Since the dynamics of the kite are only influenced by the tether tension at the kite, the radial component of the tether gravity can be ignored.

In order to clarify this possibly counterintuitive conclusion, a thought experiment is shown in figure 4.5. An AWT is flying in a straight line, continuously in crosswind in a fictitious environment where the wind blows parallel but opposite to gravity. Two scenario's are shown. In the first case (left), the kite is connected to a slider on the ground with a massless tether. The tether tension at the kite $F_{t,k}$ balances the upward component of the net aerodynamic force N. The tether tension is balanced by a reaction force from the slider. In the second case (right), a tether is attached to the kite with a carefully chosen mass such that $F_{t,k} = m_t g$. The resulting tension at the ground station $F_{t,gs}$ is zero and

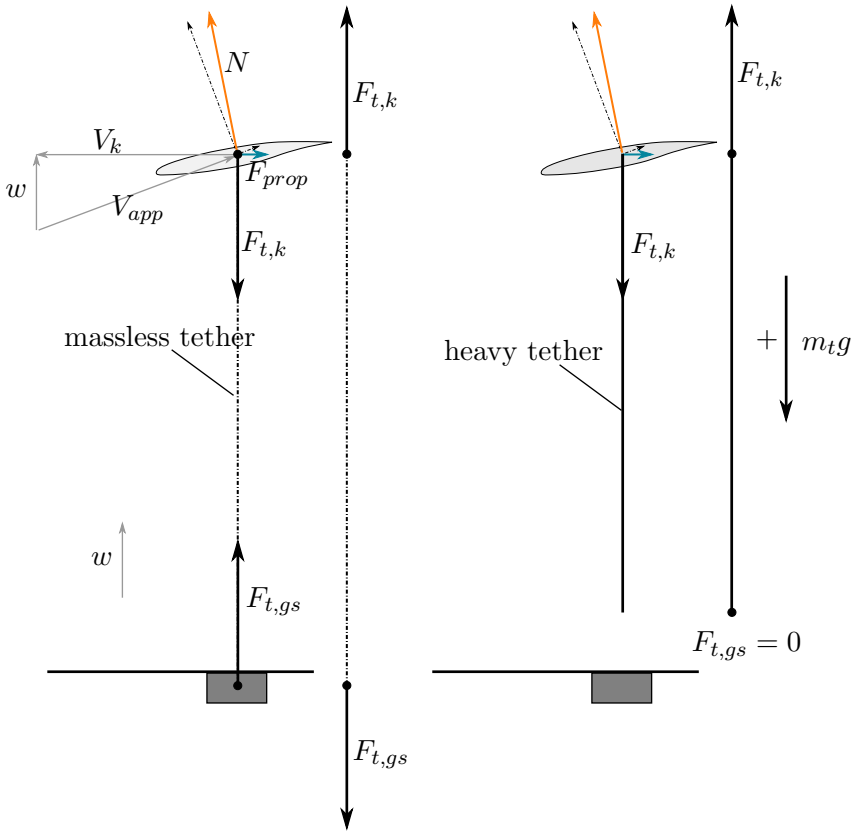

Figure 4.5: Thought experiment with a linear AWT showing that the tether tension at the kite is independent of gravitational pull on the kite (in this orientation)

thus the tether can be detached from the slider (as shown). Since $F_{t,k}$ is equal in both scenarios, the dynamics are equal. The difference between the two cases is that the case of the massless tether the vertical component of N is balanced by a reaction force at the ground while in the second case, it is balanced by gravity acting on the tether. In other words, the kite does not "know" to which force it is reacting.

For the general case where the elevation angle is not vertical, the same reasoning holds regarding the radial component. However, the now present tangential component causes the tether to follow a catenary curve which changes local tether angle at the kite. Using the approach from Noom in [48], the tether is simplified to a straight rod with a radial and tangential component of gravity acting as a distributed load. However, as explained above, the radial component is ignored since pre-tension is present. Figure 4.6 shows the resulting simplified model. Using expression 4.19, the force at the kite due to the gravitational pull on the tether mass is shown in 4.20

$$F_{g,t,k} = \frac{1}{2} m_t g \cos\beta \boldsymbol{e}_\theta \tag{4.20}$$

An important observation is that $\boldsymbol{e}_\theta$ is generally not aligned with the vertical (only at zero elevation). In order to guarantee the tether does not go slack over it's entire length, the minimum tension at the kite is equal to the radial component of equation 4.19.

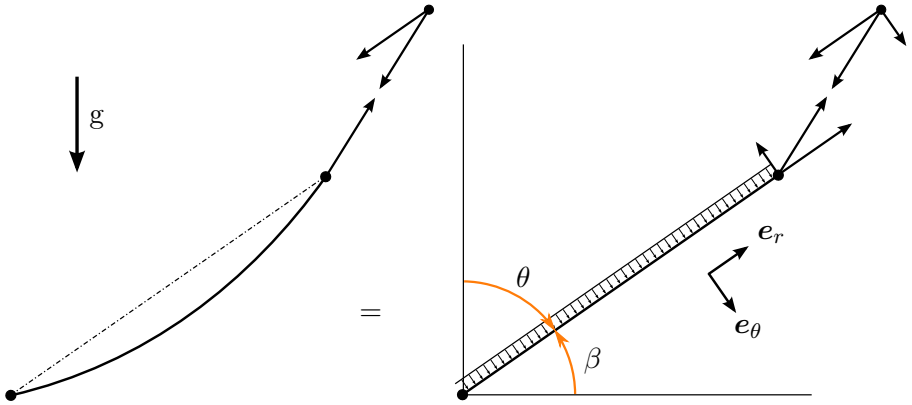

Figure 4.6: Simplified tether model: the rotation of the tether force due to the gravity catenary (exaggerated) is equal to adding a force in tangential direction equal to the distributed load (after Noom [48])

Elasticity

As inertial and external forces act on the wing a major fraction of the force it is transferred through the bridles into the tether, and ultimaltely through the ground station into the ground. Due to the tension in the tether, it will elongate and thus store potential energy. The change in length is generally less than 1% and so is expected to not affect the system dynamics significantly. However, the potential energy stored in the tether is not negligible. For Wing 7, the tether spring stiffness is about 15kN/m with typical tether stretch of around 1m which results in about 7.5kJ. Compared to a typical 100kJ of energy generation per loop this is considered significant. Especially in the scope of optimization, the potential tether energy can act as a energy buffer to transfer energy from power constrained sections of the loop to unconstrained parts. The tether is assumed to behave as a linear spring without damping or hysteresis losses, leading to the potential energy V_t stored in elongation as in equation 4.21.

$$V_t = \frac{1}{2} k_t \left(l_t - l_{t,0}\right)^2 \tag{4.21}$$

$$k_t = \frac{E_t A_t}{l_{t,0}} \tag{4.22}$$

where k_t can be found from the flexural modulus E_t, cross-sectional area A_t and undeformed length $l_{t,0}$ using eq. 4.22. Since the potential energy shown in equations 4.21 is a conserved property, it can be included in the Lagrangian during the derivation of the equations of motion.

It should be mentioned that by modeling the tether as a linear spring, the radial component of equation 4.19 is ignored. Although as discussed above, this component will not affect the magnitude of the tension at the kite, it will affect the strain distribution in the tether. Since the magnitude of this contribution is depending on the elevation angle, the true spring stiffness of the tether is nonlinear and time dependent. This causes the tether force to not be conservative, violating the assumption above. However, since elevation

angles are low and the tether weight is less than 1% of the maximum tether tension, the error is expected to be very small.

In order to avoid compression in any part of the tether, a minimum positive tension equal to the radial component of equation 4.19 is set as a constraint in the optimization.

4.5 Bridles

The tether is attached to the wing through a set of bridles. The connections between the bridle lines and both the tether and the wing are modeled as a spherical joints, i.e. constraining all translational degrees of freedom and allowing all rotational ones. In order to simplify the kinematics, the bridle lines are assumed to have no elastic deformation. Additionally the system dynamics are constrained such that the bridle lines are always under tension. This can be achieved by enforcing the following constraints while solving the equations of motion:

- Constrain tether force: $F_t > 0$
- Constrain bridle-tether angle to not exceed the bridle aperture (internal) angles: $-\phi_{\text{br}} < \chi_{\text{br},1}$ and $\phi_{\text{br}} < \chi_{\text{br},2}$

The tether roll angle ϕ_{br} will be defined in figure 5.2. Under these conditions the bridle system behaves as a set of two rigid links with fixed length and aperture angles $\chi_{br,1}$ and $\chi_{br,2}$. As the bridles are connected to the wing with two spherical joints this is equivalent to a revolute joint. This constrains the bridle system to rotate along a circle in a $\{X_{\overline{B}}, Z_{\overline{B}}\}$ plane with fixed $Y_{\overline{B}}$ coordinate. The $Y_{\overline{B}}$ coordinate of the bridle rotation plane, determined by the position of the bridle attachment points and length of the individual bridle lines, does not coincide with the center of gravity. Even at $\phi_{\text{br}} = 0$, the tether force generates a moment of force around the center of gravity.

4.6 Power system

In order to absorb the available power, four on-board turbines extract energy from the apparent wind speed. Since all elements of the power system can reverse their function, the words turbine/propeller and motor/generator are used interchangeably. The propellers slow the airspeed $\boldsymbol{V}_a$ down, adding a drag force D_{prop} and convert it into rotational speed and torque $\{\Omega, \tau\}$ Each propeller shaft is coupled to a generator which converts the available mechanical power $\{\Omega, \tau\}$ into electric power. Each generator is in turn controlled by a motor drive which converts the electrical power into a DC signal which can be transmitted down the tether to the load (e.g. the grid).

4.6.1 Propeller performance

From an energy generation perspective, the key point of interest is at which efficiency the available wind energy $\{V_a, D_{\text{prop}}\}$ is converted into mechanical power $\{\Omega, \tau\}$. In order to

address limiting factors such as torque limits, tip speed mach number it is crucial to resolve the power to output into Ω and τ separately. The propellers on Wing 7 are fixed-pitch meaning that the geometric incidence angle of the blades cannot be controlled. The only control variable is therefore the amount of torque absorbed or added by the generator. The resulting angle of attack on the blades is thus only a function of the local airspeed and the local tangential velocity on the blade due to the rotational velocity. Although local twist in the blade affects the local angle of attack, an important ratio to describe the propeller as a whole is the non-dimentional advance ratio J, given by

$$J = \frac{2\pi V_{\text{a,prop}}}{\Omega D} \tag{4.23}$$

where $V_{\text{a,prop}}$ is the local airspeed in front of the propeller and D the propeller diameter. When no torque (end thus power) is fed into or absorbed from the shaft, the propeller will be free-spinning. As the advance ratio increases, so does the angle of attack on the blades which generates torque, absorbed by the shaft. Above a certain value $J_{\max}$, the blades will stall which results in a sharp drop in efficiency and strong vibrations in the airframe. If the propeller spins faster than it's free-spinning value at that airspeed it consumes power from the shaft and provides thrust. This could be desired for certain parts of the trajectory in low wind speeds.

In order to determine the performance of the propellers a similar approach as the aerodynamic analysis was taken where the output of a high-fidelity analysis was represented using a surrogate model. The analysis was available at Makani Power and was performed using the software tool XROTOR which uses an extension of classical blade-element/vortex formulation [60]. Figure 4.7 shows a performance map of the W7 propellers which was obtained using XROTOR. The generator and power electronics will impose limits on the maximum torque and power which can be absorbed, indicated in figure 4.7. Together with the advance ratio limit discussed above and a maximum tip Mach number (not shown), these limits bound the operation envelope of the propellers.

Within this operation envelope, the XROTOR output was fitted to a surrogate model using least squares regression. The surrogate model is shown below:

$$\tau(\Omega, V_a) = a_1\Omega + a_2\Omega^2 + a_3 V_a + a_4 V_a^2 + a_5 V_a \Omega + a_6 \tag{4.24}$$

$$D(\Omega, V_a) = b_1\Omega + b_2\Omega^2 + b_3 V_a + b_4 V_a^2 + b_5 V_a \Omega + b_6 \tag{4.25}$$

The resulting mechanical shaft power from the prop is then:

$$P_{\text{sh}} = \tau\Omega \tag{4.26}$$

In reality, the rotational velocity of the rotors Ω is a degree of freedom which is controlled by the torque command in the motor. Compared to the rate of change of other states in the system, the combined rotor and motor inertia is very small. This requires a high resolution control system to keep the rotors operating in the relatively narrow operation envelope shown in figure 4.7. Including the rotor rotational velocity as a degree of freedom in the equations of motion would require a large node density in the trajectory discretization.

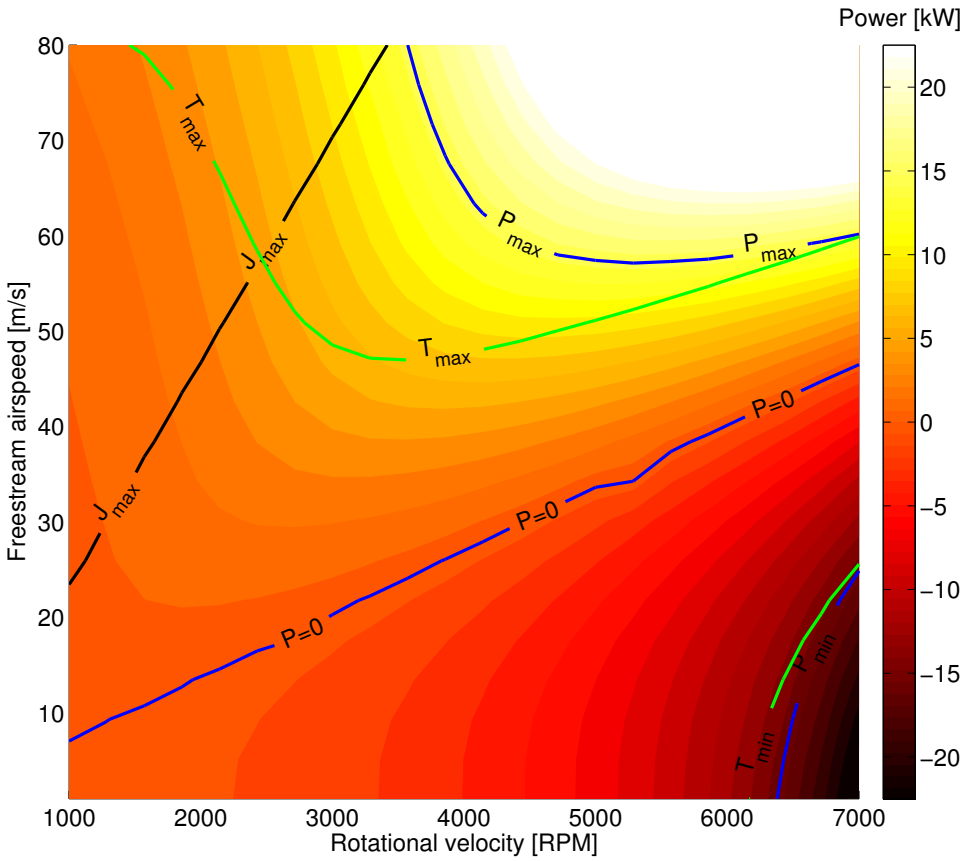

Figure 4.7: Shaft power output of a Wing7 propeller. Positive power indicates power generation. The advance ratio limit is indicated with $J_{\max}$. Torque and power limits from the generator and power electronics are also shown.

The alternative, which was implemented in the model, is to directly control the rotational velocity or advance ratio of the rotors. By setting proper bounds on the rate of change of the control variable, the time history of the rotor speed can be kept feasible. A disadvantage of this approach is that the energy stored in the rotating inertia is not included. Since periodic constraints on the controls are applied, this energy is recovered after a full cycle. However, rotational inertia could provide an energy buffer which allows transferring energy from power constrained parts of the loop to unconstrained parts. The rotational energy stored in each rotor spinning at maximum speed is about 8kJ of which maybe half is usable as a buffer since the rotor speed can not be reduced much without deviating too much from the optimal power setting. Compared to a typical high power loop, with available shaft power around 17kW and a cycle time of 10 seconds this results in a buffer size less than 10% of the available energy. For lower power cases, rotor speeds are lower and the relative size of the buffer drops even further.

4.6.2 Generator

The generators are connected to the shaft of the propellers and convert the shaft power into electrical power. The main motivation to model the electrical performance of the generators is to include how the efficiency changes depending on the operating conditions. It should be noted that the generators are also electrical motors but the term generator is used here to indicate it's primary function, generating electrical power. However, from an electrical perspective they are identical. Developing a full electrical model including each phase separately would be beyond the scope of this work so instead an equivalent DC-motor is used, based on [61].

The electric model tries to predict the electric output power $\{I, V\}$ for a given shaft speed and torque $\{\Omega, \tau\}$. It is assumed that the motor behavior can be captured with constant speed and torque coefficients k_n, k_τ. When using the units $\frac{\text{rad/s}}{\text{V}}$ and $\frac{\text{Nm}}{\text{A}}$, these coefficients are related in the following way:

$$k_n = \frac{1}{k_\tau} \tag{4.27}$$

The losses in the generator are modeled as coming from three different sources (in order of importance):

- Resistive impedance loss R [Ω]. In reality the impedance will change with temperature but is assumed constant here.
- Eddy current torque loss k_{ec} [Nm/rad/s] proportional to motor speed.
- Constant friction torque τ_{fric} [Nm] independent of motor speed and shaft torque.

The output current, voltage power and efficiency can then be computed as follows:

$$I = \frac{1}{k_\tau}\left[\tau - \tau_{\text{fric}} - k_{\text{ec}}\Omega\right] \tag{4.28}$$

$$V = \frac{1}{k_n}\Omega - IR \tag{4.29}$$

$$P_{\text{el,gen}} = IV \tag{4.30}$$

$$\eta_{\text{gen}} = \frac{\tau\Omega}{P_{\text{el,gen}}} \tag{4.31}$$

All values for the above constants were obtained from other models and measurements performed priorly at Makani Power.

4.6.3 Motor controller and tether

Each generator is controlled by a power electronics circuit (called motor controller or drive) which converts the alternating electric power from the generator to a DC signal which is sent down the tether. Compared to the generator, the efficiency of the motor controllers is fairly constant over the operating range. In order to avoid unnecessary

complexity, they are therefore modeled as having a constant efficiency $\eta_{\text{mc}} = 0.95$ and imposing an electric input power limit of 6.5 kW.

For the same argument, the tether is also modeled as having a constant electrical efficiency $\eta_t = 0.95$

4.7 Environment

The earth is assumed to be an inertial reference frame with constant gravitational acceleration of $g = 9.81$ ms^{-2}. An atmosphere with constant density of $\rho = 1.225$ kg m^{-3}.

As wind speed is a very sensitive parameter to power output, it is modeled as being independent of altitude. Although this is a drastic assumption, it allows better measurement of sensitivities. An example is to study the effect of maximum flight path curvature. With an imposed minimum altitude, a maximum curvature constraint (assuming it can be active) will affect the maximum altitude. If the wind speed varies with altitude, the measured sensitivity will be dominated by the local change in wind speed. Furthermore, a constant wind speed allows easier comparison with analytical theory.

In order to predict long term energy production and use it as the performance metric (see section 3.3.1), a mean wind speed and frequency distribution is required. In accordance with the IEC 61400-1 norm, a Rayleigh distribution is used. Such a distribution has been shown (e.g. [62]) to correlate well with measured wind site data but is of course site specific. Figure 4.8 shows such a distribution for three IEC wind classes with a mean (not most probable!) of 7.5, 8.5 and 10 ms^{-1}. As Makani Power hopes to be profitable in relatively low wind areas, the lowest class was chosen with a mean wind speed of 7.5 ms^{-1}.

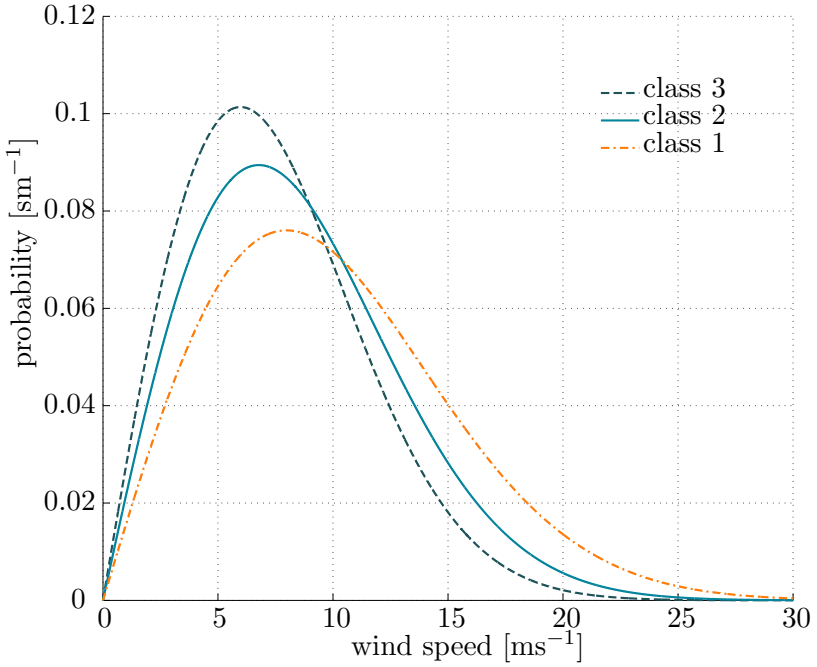

Figure 4.8: Rayleigh distribution for three IEC wind classes with different mean velocity

5

Equations of motion

With the individual subsystems described and the reference frames in place, this chapter describes the steps to obtain the equations of motion for the system. The actual derivation is quite elaborate and is therefore shown in appendix B.

5.1 Kinematics

As introduced in section 4.5, the bridles are approximated by a rigid triangle connected to the wing with a revolute joint. The connection between the bridles and the tether, called the bridle point $\boldsymbol{r}_{\text{br}}$ here, is a in reality a spherical joint so both the tether and the bridle can rotate independently around an axis parallel to the body y-axis (see figure 5.1). In principle this allows an additional degree of freedom where $\theta_b \neq \theta_t$. As the tether force is very large compared to the inertia of the bridle-tether system around this axis, it is assumed that the tether and bridle are always aligned, i.e. $\theta_b = \theta_t$. This simplification reduces the spherical joint to another revolute joint (ignoring torsion in the tether). The resulting degrees of freedom are shown in figure 5.2 which also shows the definition of the effective bridle length l_{br}.

With these assumptions, the bridle point lies $\boldsymbol{r}_{\text{br}}$ on the circle with radius l_{br}, in a $\{X^{\overline{B}}, Z^{\overline{B}}\}$ plane with fixed $Y^{\overline{B}}$ coordinate. The assumption that the tether and bridles are aligned is equivalent to positioning the bridle point such that it is closest to the tether ground attachment point. In order to find the location of the bridle point, first the unit vector $\boldsymbol{e}_{\text{br}}^{\overline{B}}$ as seen from the centre of mass (notice the reference frame is $E_{\overline{B}}$) is determined in equations 5.1 and 5.2. This is done by omitting the y-coordinate from the $\boldsymbol{r}^B$ vector, reversing it and normalizing the result. The position of $\boldsymbol{r}_{\text{br}}^{\overline{B}}$ can then be found at a distance l_{br} in the $\boldsymbol{e}_{\text{br}}^{\overline{B}}$ direction and offsetting the result to the correct $Y^{\overline{B}}$ location (equation 5.3). Finally the location of the bridle point in the E_E reference frame can be obtained using expression 5.4.

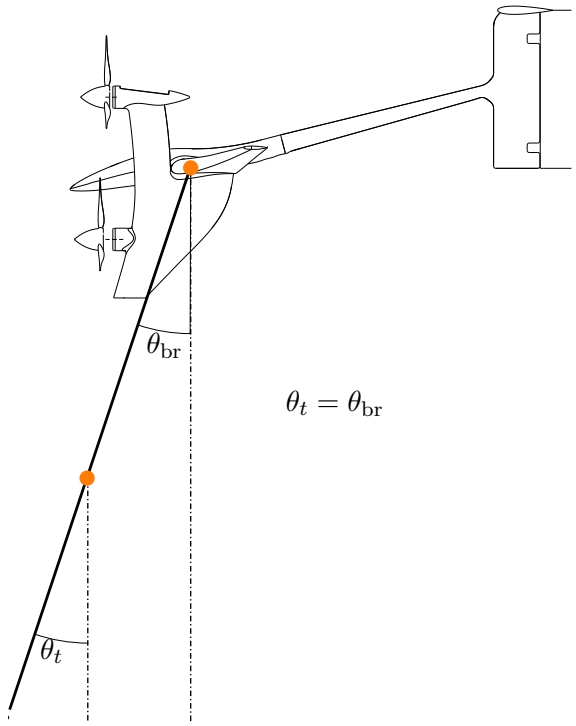

Figure 5.1: Illustration of the assumption that the bridle and tether are always aligned

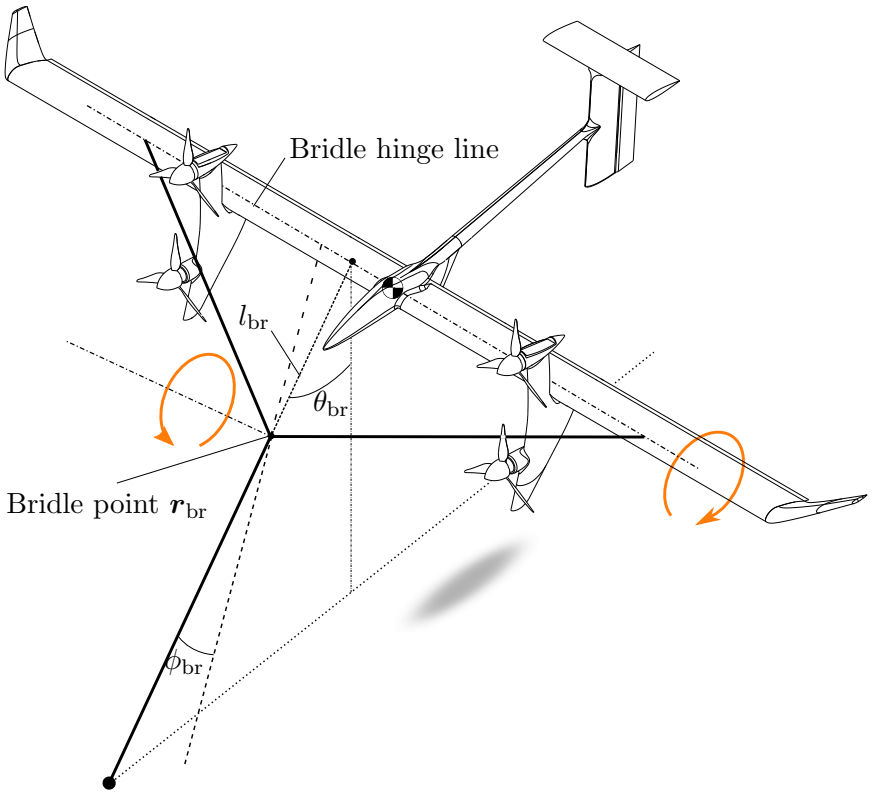

Figure 5.2: Degrees of freedom for the bridle system. Notice the offset between the tether working line and center of gravity at $\phi_{\text{br}} = 0$

$$\boldsymbol{t}_{\mathrm{br}}^{\overline{B}} = -\begin{bmatrix} \boldsymbol{r}_x^B \\ 0 \\ \boldsymbol{r}_z^B \end{bmatrix} \tag{5.1}$$

$$\boldsymbol{e}_{\mathrm{br}}^{\overline{B}} = \frac{\boldsymbol{t}_{\mathrm{br}}^{\overline{B}}}{|\boldsymbol{t}_{\mathrm{br}}^{\overline{B}}|} \tag{5.2}$$

$$\boldsymbol{r}_{\mathrm{br}}^{\overline{B}} = \boldsymbol{e}_{\mathrm{br}}^{\overline{B}} l_{\mathrm{br}} + \mathbf{1}_y \, y_{\mathrm{br}}^B \tag{5.3}$$

$$\boldsymbol{r}_{\mathrm{br}}^E = \boldsymbol{r} + \boldsymbol{R}\boldsymbol{r}_{\mathrm{br}}^{\overline{B}} \tag{5.4}$$

The tether length is now simply the distance between the ground station and the bridle point:

$$l_t = \|\boldsymbol{r}_{\mathrm{br}}^E\| \tag{5.5}$$

By analytically finding the location of the bridle point (expression 5.4), the tether-bridle system can be treated as a time-varying force and moment instead of a component with separate states. The orientation of the tether with respect to the center of mass is thus not obtained through integration but described analytically. It is however important to identify the possible orientations to get an insight in the dynamics. The bridle and tether pitch angles $\theta_t, \theta_{\mathrm{br}}$ are shown in figure 5.1 and are assumed equal. Figure 5.2 shows the bridle roll angle ϕ_{br} which will prove to be crucial for the wing's turning performance. Since the center of mass is located on the bridle hinge line, the moment caused by the tether will only have a roll and yaw component. Generally, θ_{br} is small such that the tether moment mainly causes a roll moment at the wing. Finally, as the wing rotates around the tether direction it will twist the tether the same amount. The spherical joint at the ground station allows the tether to rotate freely. In reality some friction is present and some twist will build up but this is not expected to affect the dynamics of the system significantly.

Overall, this system results in six degrees of freedom, the position of the wing's center of mass: $\boldsymbol{r}^E \in \mathbb{R}^3$ and the rigid body orientation of the wing. As introduced in section 4.1, the three rotational degrees of freedom are described using a direction cosine matrix $\boldsymbol{R}_{EB}$ with nine individual components. The rotational rates however are described using a 3-element vector $\boldsymbol{\omega} \in \mathbb{R}^3$.

5.2 Lagrangian dynamics

The equations of motion are derived using the Lagrangian formalism of the second kind. Since the same generalized coordinates are used, the methodology is strongly based on the work of Gros et al. [23]. The most important difference is that the tether is not treated as a constraint but as described in section 4.4 and no control is present on the tether length. The equations of motion can be derived using equation 5.6.

$$\frac{d}{dt}\left(\frac{\partial \mathcal{L}}{\partial \dot{q}_j}\right) - \frac{\partial \mathcal{L}}{\partial q_j} = Q_j \tag{5.6}$$

Where $\mathcal{L}$ is the Lagrangian of the system, q_j are the generalized coordinates used to describe the kinematics of the system and Q_j are the generalized forces. The Lagrangian is defined as the difference between the kinetic energy T and potential energy V of the system.

$$\mathcal{L} = T - V \tag{5.7}$$

The generalized coordinates are chosen to be the components of the DCM $\boldsymbol{R}_{EB}$ and the position vector $\boldsymbol{r}_{cg}$ of the kite center of mass in the inertial frame of reference as shown in equation 5.8. For the sake of brevity the subscripts $_{EB}$ and $_{cg}$ are dropped in the future.

$$\boldsymbol{R}_{EB} = \begin{bmatrix} e_{11} & e_{12} & e_{13} \\ e_{21} & e_{22} & e_{23} \\ e_{31} & e_{32} & e_{33} \end{bmatrix} \quad \boldsymbol{r}_{cg} = \begin{bmatrix} x_{cg} \\ y_{cg} \\ z_{cg} \end{bmatrix} \tag{5.8}$$

Although using the components of the DCM as a generalized coordinate will prove to be convenient later on, a more intuitive set of coordinates are angular rates of the body, expressed in the body frame of reference, denoted with $\boldsymbol{\omega}$. The relation between the two is derived in appendix B and is repeated below (equation 5.9)

$$\dot{\boldsymbol{R}} = \boldsymbol{R}\boldsymbol{\omega}_{\times} \tag{5.9}$$

5.2.1 Kinetic and potential energy

Including the contribution of the tether as discussed in section 4.4, the total inertial mass of the system is:

$$m_{\text{in}} = m_k + \frac{m_t}{3} \tag{5.10}$$

The kinetic energy of the system can then be stated as:

$$T = \frac{1}{2}\left(\boldsymbol{\omega}^T \boldsymbol{J} \boldsymbol{\omega}\right) + \frac{1}{2}\left(\dot{\boldsymbol{r}}^T m_{\text{in}} \dot{\boldsymbol{r}}\right) \tag{5.11}$$

where $\boldsymbol{J}$ is the inertia tensor expressed in the body frame.

The potential energy consists of a contribution due to gravity and the elastic elongation of the tether. As described in section 4.4, the gravitational effect of tether mass is not

treated as a conservative force but instead added as a generalized force. Therefore the only contribution of the gravitational force to the potential energy treated here is the wing mass. Using equation 4.21 and expression 5.5 for the tether length, the potential energy in the tether is shown in equation 5.12 where $l_{\mathrm{t},0}$ is the tether length at zero strain and k_t is tether spring constant which can be found using equation 4.22

$$V_t = \frac{1}{2}k_t \left(\left(\left(\boldsymbol{r} + \boldsymbol{R}\boldsymbol{r}_{\mathrm{br}}^{\overline{B}} \right)^T \left(\boldsymbol{r} + \boldsymbol{R}\boldsymbol{r}_{\mathrm{br}}^{\overline{B}} \right) \right)^{1/2} - l_{\mathrm{t},0} \right)^2 \tag{5.12}$$

The total potential energy of the system is shown in equation 5.13

$$V = \frac{1}{2}k_t \left(\left(\left(\boldsymbol{r} + \boldsymbol{R}\boldsymbol{r}_{\mathrm{br}}^{\overline{B}} \right)^T \left(\boldsymbol{r} + \boldsymbol{R}\boldsymbol{r}_{\mathrm{br}}^{\overline{B}} \right) \right)^{1/2} - l_{\mathrm{t},0} \right)^2 + m_k g z \tag{5.13}$$

Combining the terms gives the Lagrangian of the system:

$$\mathcal{L} = \underbrace{\left[\frac{1}{2} \left(\boldsymbol{\omega}^T \boldsymbol{J} \boldsymbol{\omega} \right) + \frac{1}{2} \left(\dot{\boldsymbol{r}}^T m_{\mathrm{in}} \dot{\boldsymbol{r}} \right) \right]}_{\text{kinetic energy } T} - \underbrace{\left[\frac{1}{2}k_t \left(\left(\left(\boldsymbol{r} + \boldsymbol{R}\boldsymbol{r}_{\mathrm{br}}^{\overline{B}} \right)^T \left(\boldsymbol{r} + \boldsymbol{R}\boldsymbol{r}_{\mathrm{br}}^{\overline{B}} \right) \right)^{1/2} - l_{\mathrm{t},0} \right)^2 + m_k g z \right]}_{\text{potential energy } V} \tag{5.14}$$

The complete derivation of the equations of motion is given in appendix B. The resulting equations are shown below 5.15.

$$\begin{bmatrix} m_{\mathrm{in}} \boldsymbol{I}_3 & 0 \\ 0 & \boldsymbol{J} \end{bmatrix} \begin{bmatrix} \ddot{\boldsymbol{r}} \\ \dot{\boldsymbol{\omega}} \end{bmatrix} = \begin{bmatrix} \mathbf{F} + m_k g \mathbf{1}_z - k_t \lambda \left(\boldsymbol{r} + \boldsymbol{R}\boldsymbol{r}_{\mathrm{br}}^{\overline{B}} \right) \\ \boldsymbol{M}^B - \boldsymbol{\omega} \times \boldsymbol{J}\boldsymbol{\omega} - k_t \lambda \left(\boldsymbol{r}_{\mathrm{br}}^{\overline{B}} \times \boldsymbol{R}^T \boldsymbol{r} \right) \end{bmatrix} \tag{5.15}$$

where λ is defined as:

$$\lambda = 1 - \frac{l_{\mathrm{t},0}}{\left(\left(\boldsymbol{r} + \boldsymbol{R}\boldsymbol{r}_{\mathrm{br}}^{\overline{B}} \right)^T \left(\boldsymbol{r} + \boldsymbol{R}\boldsymbol{r}_{\mathrm{br}}^{\overline{B}} \right) \right)^{1/2}} \tag{5.16}$$

5.3 Generalized forces

The terms $\boldsymbol{F}$ and $\boldsymbol{M}^B$ in the equations of motion (5.15) refer to *generalized forces*. In the general case of Lagrangian dynamics they represent the change in virtual work done by the generalized coordinates under the influence of external forces. In the case of this particular choice of generalized coordinates they are equivalent to physical forces ([N]) and moments ([Nm]) in the earth and body reference frame respectively. In the following sections the contributions of tether gravity, aerodynamics and the power systems to these external forces are determined.

5.3.1 Tether gravity

As discussed in section 4.4, the gravitational force of the tether on the kite is approximated with equation 4.20, repeated below.

$$\boldsymbol{F}_{g,t,k} = \frac{1}{2} m_t g \cos\beta \boldsymbol{e}^E_{\text{tan}} \tag{5.17}$$

The unit vector $\boldsymbol{e}^E_{t,tang}$ is oriented perpendicular to the tether radial axis and lies in the plane spanned by the Z^E vector and the radial unit vector $\boldsymbol{e}^E_{\text{br}}$. Equation 5.18 shows the decomposition in earth-reference frame coordinates.

$$\boldsymbol{e}^E_\theta = \frac{\boldsymbol{e}^E_{\text{br}} \times (\mathbf{1}_z \times \boldsymbol{e}^E_{\text{br}})}{\|\boldsymbol{e}^E_{\text{br}} \times (\mathbf{1}_z \times \boldsymbol{e}^E_{\text{br}})\|} \tag{5.18}$$

Since the force acts on the bridle point it's important to consider how it is transferred through the bridles to the wing. Regardless of the orientation between the unit vector $\boldsymbol{e}^E_\theta$ and the bridle plane (the plane in which the bridles lie), the force is simply transmitted through the bridles and the same force acts on the wing's center of mass. Due to the degrees of freedom in the bridle system the resulting moments of force however depend on the orientation. If $\boldsymbol{e}^E_\theta$ lies in the bridle plane, the resulting moment on the wing is the same as if the entire bridle system was rigid. In the case were $\boldsymbol{e}^E_\theta$ is perpendicular to the bridle plane, the bridle will slightly rotate around the tether-bridle joint and therefore not transmit any moment. For the sake of simplicity the resulting shift in bridle point is ignored In order to obtain the transmitted moment, $F_{g,t,k}$ is projected onto the bridle plane and cross multiplied with the moment arm (expression 5.19)

$$\boldsymbol{M}_{g,t,k} = \boldsymbol{r}^{\overline{B}}_{\text{br}} \times \left[(\boldsymbol{F}^B_{g,t,k} \cdot \mathbf{1}_y) \boldsymbol{e}^{\overline{B}}_y + (\boldsymbol{F}^B_{g,t,k} \cdot \boldsymbol{e}^{\overline{B}}_{\text{br}}) \boldsymbol{e}^{\overline{B}}_{\text{br}} \right] \tag{5.19}$$

5.3.2 Aerodynamics

As discussed in section 4.2, the aerodynamic forces and moments are described using stability and control derivatives. For each derivative and first order coefficient, the value is determined using equation 4.6. The contributions for both force and moment coefficients in each direction (X_B, Y_B, Z_B) are subsequently added. Expressions 5.20 and 5.21 show this as an example for the X_B direction.

$$C_X(\alpha, \beta, \hat{r}, \delta r) = C_X(\alpha, \beta) + C_{X_r}\hat{r} + C_{X_{\delta r}}\delta r \tag{5.20}$$

$$C_m(\alpha, \beta, \hat{q}, \hat{r}, \delta e) = C_m(\alpha, \beta) + C_{m_q}\hat{q} + C_{m_r}\hat{r} + C_{m_{\delta e}}\delta e \tag{5.21}$$

The resulting generalized forces and moments due to aerodynamics are given by

$$\boldsymbol{F}_{aero} = \begin{bmatrix} C_X(\alpha, \beta, \hat{r}, \delta r,) \\ C_Y(\alpha, \beta, \hat{r}, \delta r) \\ C_Z(\alpha, \beta, \delta f, \delta a1, \delta a2) \end{bmatrix} \frac{1}{2}\rho V_a^2 S \tag{5.22}$$

$$\boldsymbol{M}_{aero} = \begin{bmatrix} C_l(\alpha, \beta, \hat{p}, \hat{r}, \delta a1, \delta a2)\, b \\ C_m(\alpha, \beta, \hat{q}, \hat{r}, \delta e)\, c \\ C_n(\alpha, \beta, \hat{r}, \hat{p}, \delta r, \delta a1, \delta a2)\, b \end{bmatrix} \frac{1}{2}\rho V_a^2 S \tag{5.23}$$

5.3.3 Power systems

The generated drag (or thrust) by the propellers is assumed to act on the center of the rotor disc and is assumed parallel to the X_B direction. As the motors are not located on the center of gravity the resulting moment of force is included. This moment has a component around the Y_B and Z_B axis and thus affects both pitch and yaw stability. As each motor is controlled separately, this allows the use of *motor steering* in conjunction with the rudder. Gyroscopic moments arising from the spinning inertia are ignored as the produced toques are an order of magnitude lower than the aerodynamic moments acting on the wing.

In order to use the method described in 4.6.1, the local airspeed at the position of the rotor plane should be determined. Two effects are included which cause the local airspeed to differ from the airspeed at the center of gravity:

- Body rates, especially the high yaw rate.
- Aerodynamic upwash from the wing. The presence of the wing greatly affects the local airflow at the rotors. Using CFD results from Makani a symmetric lift dependent correction of $C_{\mathrm{P,corr}} = \pm 0.04\ C_L$ was estimated, where the pressure coefficient $C_{\mathrm{P,corr}}$ can be resolved in a velocities correction using equation 5.24

$$C_{\mathrm{P,corr}} = 1 - \left(\frac{V_{\mathrm{a,corr}}}{V_a}\right)^2 \tag{5.24}$$

The local velocities at the four rotor positions can then be found as:

$$\boldsymbol{V}_{\mathrm{a,prop,i}} = \boldsymbol{V}_a \left(\pm\sqrt{1 - C_{\mathrm{P,corr}}}\right) + \boldsymbol{\omega} \times \boldsymbol{r}^B_{\mathrm{prop,i}} \tag{5.25}$$

where $\boldsymbol{r}^B_{\mathrm{prop,i}}$ is the location of rotor i with respect to the center of mass. Finally the local airspeed is projected on the X_B axis:

$$V_{\infty,i} = \boldsymbol{V}_{\mathrm{a,prop,i}} \cdot \mathbf{1}_x \tag{5.26}$$

This value is used in the surrogate model (see equation 4.25) together with the advance ratio (control variable) J_i to get the value of the propeller generated drag. The resulting generalized forces and moments caused by the propellers are then:

$$\boldsymbol{F}^B_{\mathrm{prop}} = \sum_{i=1}^{4} D_{\mathrm{prop}}(V_{\infty,i}, J_i)\mathbf{1}_x \tag{5.27}$$

$$\boldsymbol{M}^B_{\mathrm{prop}} = \sum_{i=1}^{4} \boldsymbol{r}^B_{\mathrm{prop,i}} \times D_{\mathrm{prop}}(V_{\infty,i}, J_i)\mathbf{1}_x \tag{5.28}$$

6

Trajectory Optimization

This chapter covers the implementation of the optimal control problem using the methodology described in section 3.2. The cost function of the optimization, not to be confused with the performance metric used for the sensitivities, is covered first in section 6.1. Section 6.2 and 6.3 then cover the implemented control variables and bounds and constraints.

6.1 Cost function

The main objective of the optimization is maximization of average power along the loop, i.e. the total generated energy divided by the end time T (which is free parameter). Since this is an integral quantity, this requires a quadrature variable E.

$$E = \int_0^T P_{\text{el,teth}}(t)\mathrm{d}t \tag{6.1}$$

Using the results discussed in section 4.6 $P_{\text{el,teth}}$ this is found as:

$$P_{\text{el,teth}} = \sum_{i=1}^{4} P_{\text{sh}}\eta_{\text{gen}}\eta_{\text{mc}}\,\eta_{\text{t}} \tag{6.2}$$

As shown in [24], adding a small cost to the squared control action results in a faster convergence without significant impact on the solution. The total cost of this control regulation is kept at 0.1 % or less of the total objective value by choosing γ_{cr}. The resulting objective function can thus be written as:

$$J = -\frac{E}{T} + \gamma_{cr}\boldsymbol{u}^T\boldsymbol{u} \tag{6.3}$$

with $\boldsymbol{u}$ the control variable vector.

6.2 Control variables

A total of nine control variables are implemented corresponding to the movement of the five control surfaces of the wing and the instantaneous advance ratios of the four propellers. As the collocation method assumes a constant level of a certain control input for each collocation interval, the control was set on the rate of change of these variables. By adding a state for each control variable, the aerodynamic and propeller response can be determined. The implemented controls and their corresponding states are shown in table 6.1

Table 6.1: Implemented control variables and derived states

Control variable	Derived state
elevator rotational velocity $\dot{\delta_e}$ [rad/s]	elevator position δ_e [rad]
rudder rotational velocity $\dot{\delta_r}$ [rad/s]	rudder position δ_r [rad]
aileron 1 rotational velocity $\dot{\delta_{a1}}$ [rad/s]	aileron 1 position δ_{a1} [rad]
aileron 2 rotational velocity $\dot{\delta_{a2}}$ [rad/s]	aileron 2 position δ_{a2} [rad]
flap rotational velocity $\dot{\delta_f}$ [rad/s]	flap position δ_f [rad]
advance ratio rate of change $\dot{J}_{1...4}$ [1/s]	advance ratio $J_{1...4}$ [-]

6.3 Bounds and Constraints

A number of bounds and constraints are required to keep the resulting trajectory feasible. This section discusses the bounds and constraints which are considered *potentially active*, i.e. they are expected to limit the trajectory in some wind conditions at some point along the trajectory. Some states or controls have bounds which are expected to not influence the solution and are therefore not discussed here. The following relevant bounds on control variables and states are applied:

- **Control surface deflection angle** *Minimum and Maximum*; $\forall\, t \in [0, T]$
- **Control surface deflection speeds** *Minimum and Maximum*; $\forall\, t \in [0, T]$
  All control surfaces (see table 6.1) are driven by a servo motor with a certain maximum rotational speed. Additionally, a torque limitation is present but is ignored.
- **Propeller advance ratio** *Maximum*; $\forall\, t \in [0, T]$
  As discussed in section 4.6.1, a the propellers can operate up to a certain maximum advance ratio after which the blades stall.
- **Change in propeller advance ratio** *Maximum*; $\forall\, t \in [0, T]$
  Since the rotational speed of the propellers are not modeled as a free state, this constraint on the time rate of change in propeller advance ratio guarantees that the changes in rotational remain feasible. Although airspeed also affects the advance ratio (see equation 4.23), the fastest changing component is the rotational speed

of the rotors and the constraint is therefore approximated using the ratio between peak torque and rotational inertia as shown below.

$$\left(\frac{\mathrm{d}\Omega}{\mathrm{d}t}\right)_{\max} = \frac{\tau_{\max}}{I_{\text{prop}} + I_{\text{gen}}} \tag{6.4}$$

$$\left(\frac{\mathrm{d}J}{\mathrm{d}t}\right)_{\max} \approx \frac{2\pi V_{\text{ref}}}{D_{\text{prop}}} \frac{\mathrm{d}}{\mathrm{d}t}\left(\frac{1}{\Omega}\right) = \frac{2\pi V_{\text{ref}}}{D_{\text{prop}}\Omega_{\text{ref}}^2}\left(\frac{\mathrm{d}\Omega}{\mathrm{d}t}\right)_{\max} \tag{6.5}$$

where V_{ref} and Ω_{ref} are taken the minimum airspeed and maximum rotational speed respectively.

- **Altitude** *Minimum*; $\forall\, t \in [0, T]$
  In order to allow a margin for real world wind gusts, a minimum altitude of the wing tip is enforced.

The following (in)equality constraints are applied

- **Airspeed** *Minimum and maximum*; $\forall\, t \in [0, T]$
  These constraints guarantee enough control authority and maximum loads on the structure. Although, the flight envelope is for Wing 7 not limited by aeroelastic effects such as flutter, these limits could be enforced here.

- **Tether tension** *Minimum and maximum*; $\forall\, t \in [0, T]$
  Minimum tension is required to make sure the tether does not go slack which would violate the spring assumption as explained in section 4.4. The value is set slightly above the radial component of equation 4.19. Maximum tension is set to 16kN.

- **Angle of attack and sideslip** *Minimum and maximum* $\forall\, t \in [0, T]$
  These constraints limit the aerodynamic attitude. As the angle of attack impacts the maximum lift coefficient, the maximum allowed angle of attack is crucial for the performance and is expected to be active in most conditions.

- **Shaft Torque and Power** *Minimum and maximum* $\forall\, t \in [0, T]$
  A shaft torque limit arises from the motor heating due to ohmic (I^2R) losses in the motor. Although different losses occur in the motor which also lead to heating (see section 4.6.2), the ohmic losses dominate and are assumed to impose a hard current and thus torque limit. In reality the motors have a thermal time constant and a detailed model of motor heating could reveal a different flight strategy. This would be however beyond the scope of this thesis. A similar constraint arises from the motor controllers which impose a maximum input power due to heating.
  As the generators can reverse their function, these constraints also hold for motor-mode and thus also impose a minimum.

- **Propeller mach number** *Maximum* $\forall\, t \in [0, T]$
  Due to propeller noise limits, which are primarily influenced by the tip mach number, this constraint thus affects the maximum rotational speed of the rotors.

- **Orthogonality of DCM** $t = 0$
  This is the only non-physical constraint and is required to guarantee that the DCM

represents a rotation matrix with correct shape. The constraint is a set of 6 constraints applied on the individual components of the DCM and is only applied at the start of the trajectory as the correct (orthonormal) evolution of the DCM components is guaranteed through the equations of motion.

Finally, periodic boundary conditions are applied on all control variables and states in order to guarantee that the same trajectory could be flown successively.

6.4 Solution

The optimization was solved on a Macbook Pro machine with a 2.6 GHz Intel Core i7 (4 core) processor using a single logical core. The solution time depends on the initial guess and the number of active constraints but is typically around 90 seconds. Separate logical cores (8 available in this case) can be used to run multiple optimizations in parallel which allows generation of a entire power curve in about five minutes.

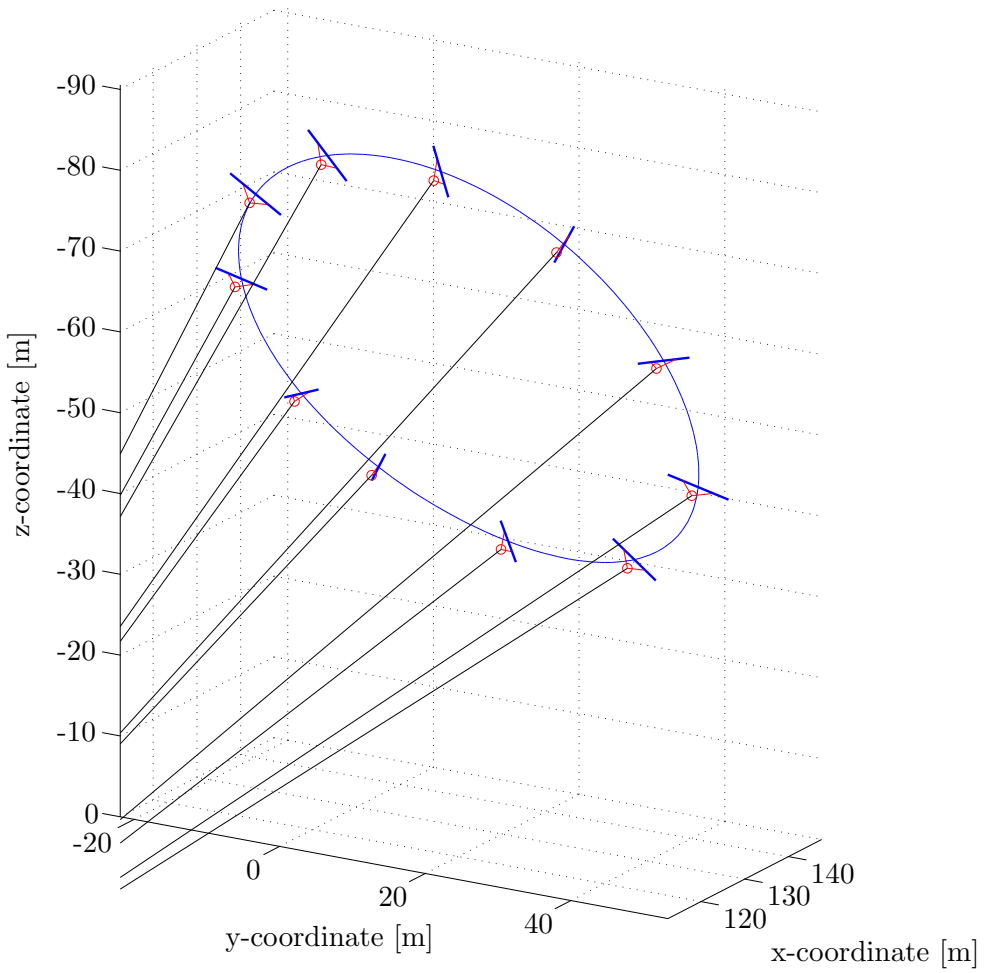

Figure 6.1: Three dimensional view of optimized Wing7 kite trajectory at w =10m/s. Time progresses in clockwise direction. The red lines represent the bridle system. The solid blue line the full Wing7 wingspan.

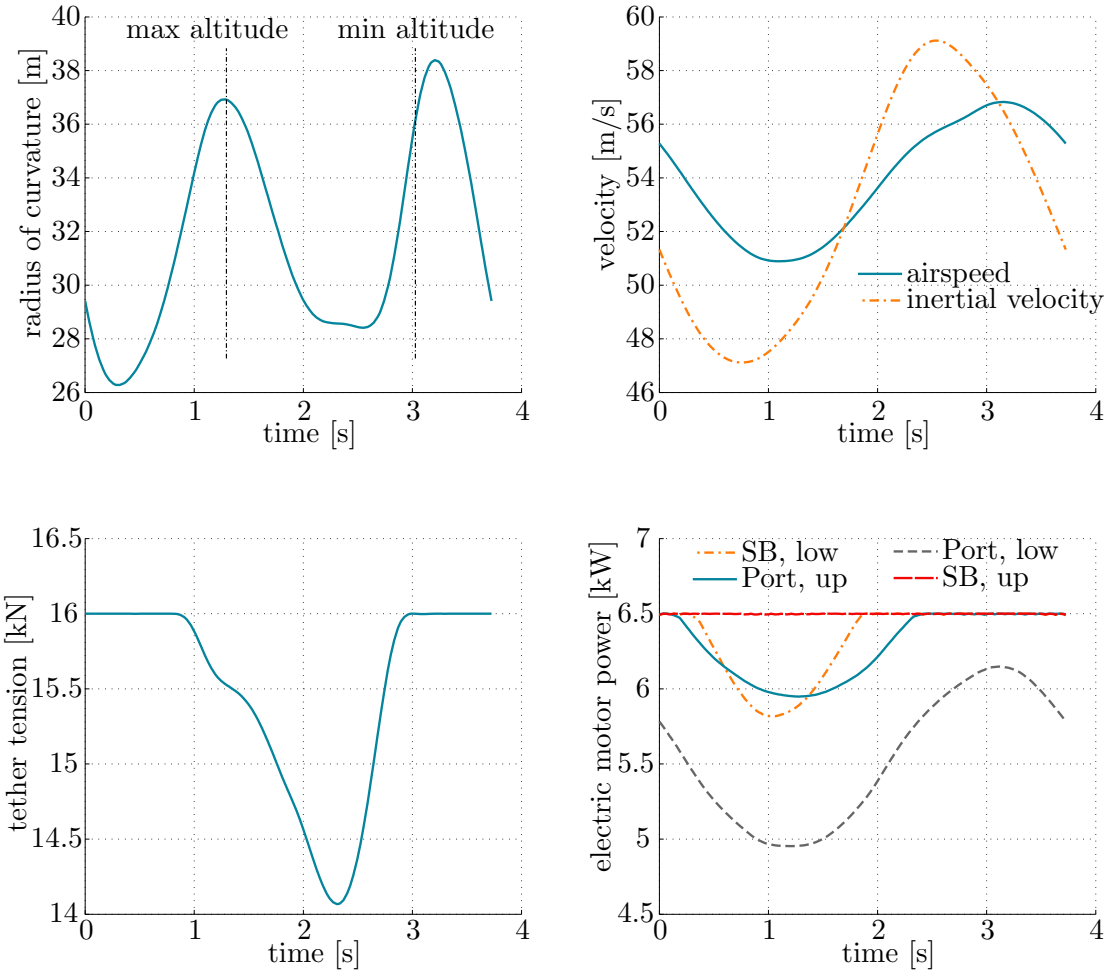

Figure 6.2: Optimization output of Wing7 baseline design at w =10m/s. Both the tether tension and motor power constraints are active on parts of the trajectory. SB refers to starboard

A typical output trajectory for Wing7 trajectory with w=10m/s is shown in figure 6.1 where the relative size of the wing, bridles and trajectory are kept correct. Some additional output is presented in figure 6.2 which shows that both the tether tension and motor power constraints are active on parts of the trajectory. Since the trajectory is inclined, the airspeed is higher than the inertial speed during the upstroke and lower during the downstroke. The curvature plot shows a mean radius of curvature of about 32m, corresponding to 4 wingspans.

6.5 Validation using Loyd's limit

In order to validate the model from a power generation perspective it is compared with the theoretical limit as originally proposed by Loyd [26]. In accordance with Vanderlind [31], this limit is corrected for the local geometry of the path as follows:

$$P_{\text{max}} = \cos(\theta)^3 \frac{2}{27} \rho w^3 A \frac{C_L^3}{C_D^2} \tag{6.6}$$

which occurs at

$$V_{\text{a,opt}} = \frac{2}{3} \frac{C_L}{C_D} w \cos\theta \tag{6.7}$$

where θ is the total angle between the wing position vector and the wind direction and can be computed as:

$$\theta = \cos^{-1}\left(\mathbf{1}_x \cdot \frac{\boldsymbol{r}^E}{|\boldsymbol{r}^E|}\right) \tag{6.8}$$

This limit is compared to the *idealized mechanical power* which is computed as the sum of the propeller shaft powers devided by there respective instantaneous efficiencies. Figure 6.3 shows the comparison for $w = 7$ m/s which has no power or tension limiting constraint active at any point along the loop. The power limit of equation 6.6 is shown for the instantaneous C_L and C_D values, indicated with ζ_{actual} and for the maximum achievable zeta ζ_{max} at every position along the loop. Comparing the two shows that the optimized solution manages quite well to stay close to the ζ_{max} condition.

Comparing the mean value of the optimization output with the idealized mechanical power shows that the optimized trajectory is less than 5% below the theoretical limit. Although close, it is interesting to investigate the reason for the difference. The lower graph on figure 6.3 shows that the optimized airspeed is significantly higher than the one predicted by equation 6.7. This is likely due to the increase of motor efficiency with reduced shaft torque. In order absorb the same amount of power and keep the propellers operating at an efficient advance ratio, the optimized airspeed is higher. Another cause is the influence of gravitational mass. This causes a variability in airspeed or absorbed power. The resulting deviation in airspeed causes a small drop in power extraction efficiency compared to the fundamental limit of equation 6.6.

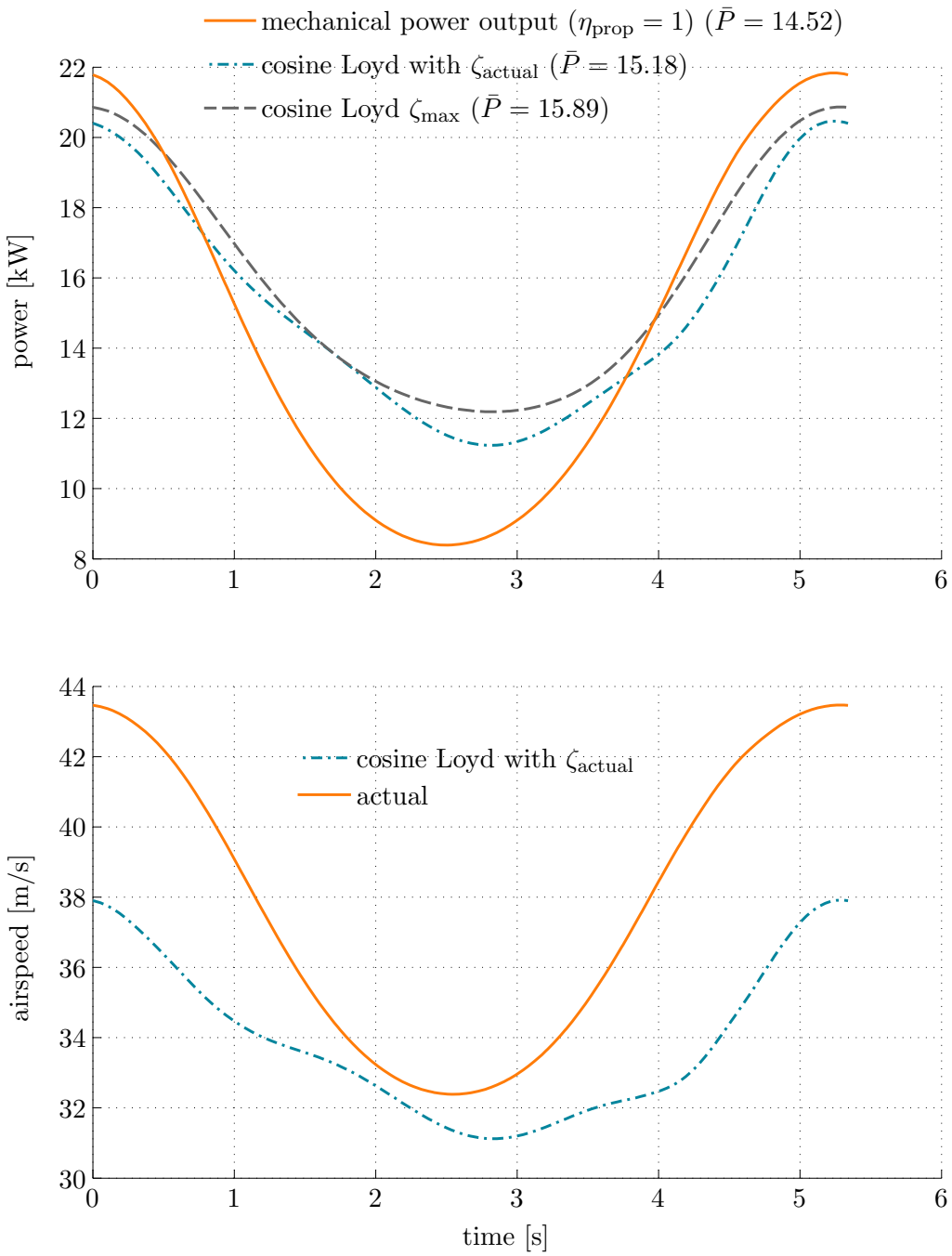

Figure 6.3: Comparison between idealized mechanical output power from the optimization and the cosine corrected Loyd limit at $w = 7$ m/s (top). Airspeed comparison between the actual and optimal airspeed as predicted by the cosine Loyd limit (bottom)

7

Results

This chapter covers the results of the sensitivity study. The following parameters are investigated based on the literature and internal discussions at Makani power: lift and drag coefficient (section 7.1) which are compared to simple analytic theory, wing mass (section 7.2), circularity of the path (section 7.3) and topology of the path (section 7.4). In each section, a few implications for the Wing7 design are discussed.

7.1 Aerodynamic coefficients

7.1.1 Lift coefficient

The effect of lift investigated by adding or subtracting a discrete amount of lift coefficient $C_{\mathrm{L,add}}$ to every aerodynamic operating point. This corresponds to shifting the $C_L - \alpha$ curve up and down. The main physical influence is the increase in maximum lift coefficient $C_{\mathrm{L,max}}$ and thus an increase in the power harvesting factor ζ. As can be seen in figure 7.1, increasing the lift coefficient causes a leftward shift of the power curve with a lower cut-in wind speed and higher power production in low wind speeds. Maximum power is not affected as this is limited by the power system. The sensitivities for different levels of added C_L are shown in table 7.1. The absolute sensitivity is 6.00 $\frac{W}{C_L-\mathrm{point}}$ near the baseline design and is slightly nonlinear. A C_L-point is defined as $1/1000^{\mathrm{th}}$ of a C_L unity, e.g. the difference between $C_L = 2.000$ and $C_L = 2.001$ is one point. The relative sensitivity of lift is also shown in table 7.1 which is 159 $\frac{W}{\%C_L}$ near the baseline.

7.1.2 Drag coefficient

Similar to the lift coefficient discussed above, changing the drag coefficient is understood as changing the parasitic drag, i.e. shifting $C_D - \alpha$ curve left and right. The results are shown in figure 7.2 and table 7.2. The sensitivity is about $36\frac{W}{C_D-\mathrm{point}}$ near the baseline design and significantly higher for drag reduction than increase. The relative sensitivity near the baseline is 122 $\frac{W}{\%C_D}$.

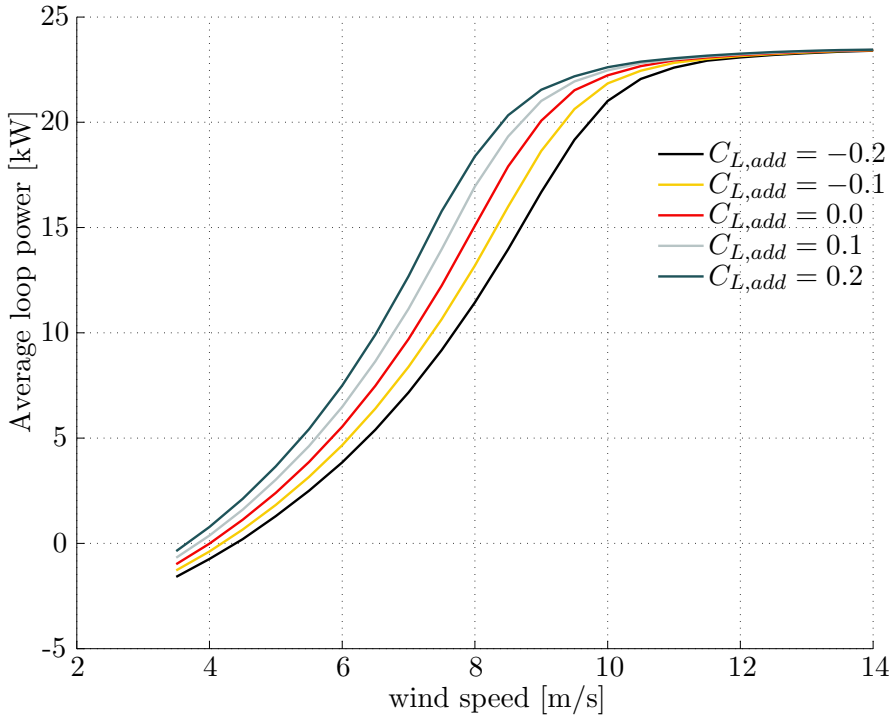

Figure 7.1: Change in Wing7 power curve due to change in $C_{L,add}$

Table 7.1: Sensitivity of lift coefficient to long term power output. A C_L-point is defined as $1/1000^{\text{th}}$ C_L

added C_L	-0.2	-0.1	**0.0**	0.1	0.2
$C_{L,\max}$	2.45	2.55	**2.65**	2.75	2.85
P_{sys} [kW]	10.01	10.67	**11.29**	11.87	12.41
capacity factor [%]	42.67	45.46	**48.11**	50.58	52.9
absolute sensitivity [W/C_L-point]	6.76	6.38	**6.00**	5.62	5.24
relative sensitivity [W/%C_L]	179.14	169.09	**159.04**	148.99	138.93

7.1.3 Discussion & comparison to Loyd's limit

A few conclusions for the Wing7 design can be drawn based on results above. First of all, the absolute sensitivity to drag is about 6 times higher than for lift. This implies that the effect of a design change which aims at improving power production should have a lift-to-drag ratio greater than 6. For example, improving the airfoil design only makes sense if the incremental change in lift and drag occurs at a ratio greater than 6.

A second implication is that the potential of lift increase or drag reduction is dramatic. An obvious design improvement is to reduce the drag caused by the tether. At the scale of Wing7, the estimated drag-coefficient of the tether by Makani is currently 1.2, referenced to it's diameter. This translates to a parasitic drag coefficient of 0.1 on the wing (referenced to wing area) using the 1/4th assumption described in section 4.4. Although Reynolds effects will slightly reduce the drag coefficient for larger systems, tether drag reduction will be a dramatic improvement on all scales. One way to reduce the drag

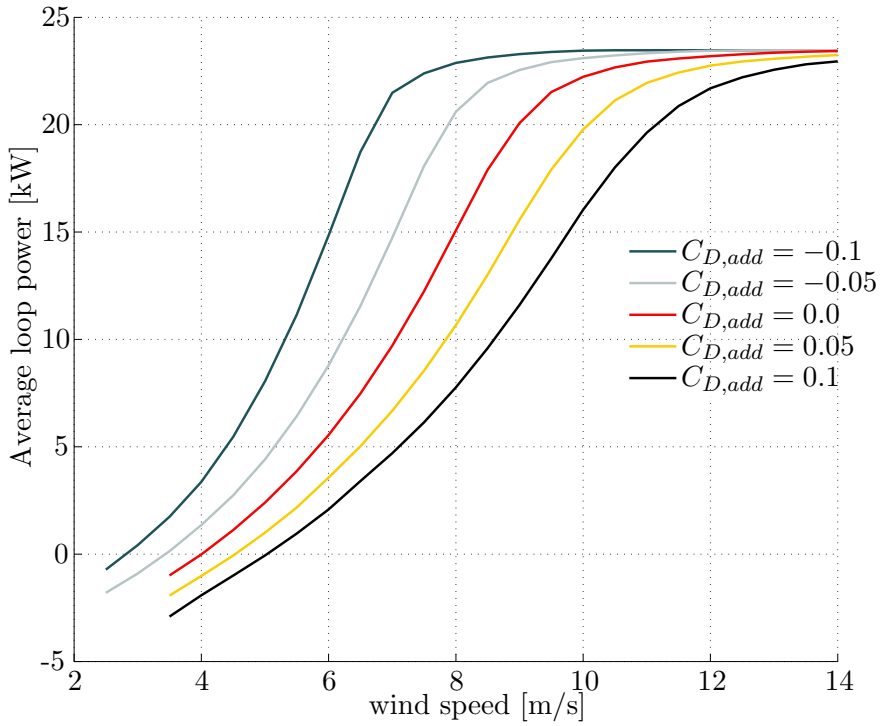

Figure 7.2: Change in Wing7 power curve due to change in parasitic drag

Table 7.2: Sensitivity of drag coefficient to P_{sys}. A C_D-point is defined as $1/1000^{\text{th}}$ C_D

added C_D	-0.1	-0.05	**0.0**	0.05	0.1
total C_D (incl. tether) at $C_{L,\max}$	0.238	0.288	**0.338**	0.388	0.438
P_{sys} [kW]	15.36	13.21	**11.29**	9.59	8.13
capacity factor [%]	65.46	56.3	**48.11**	40.87	34.65
absolute sensitivity [W/C_D-point]	-45.30	-40.73	**-36.16**	-31.59	-27.02
relative sensitivity [W/ %C_D]	-153.12	-137.67	**-122.22**	-106.77	-91.31

is by adding a faring to tether. This is common practice in deep-sea towing operations requiring a large depression angle (Henderson [63]). A relatively simple (blunt) fairing is described in [63] which has a measured drag coefficient of 0.16 for Reynolds numbers comparable to the Wing7 tether. Assuming a similar faring would be applied, the drag reduction on the kite would be 0.0867, i.e. 86.7 C_D-points. Using interpolation on the values in table 7.2, this would increase the power output from 11.3 kW to 14.76 kW, an increase of 30%.

Comparing the relative sensitivity of lift and drag shows that lift coefficient has a higher relative importance. This shows that the Wing7 system is a lift-driven design which could be expected considering the performance metric $\frac{C_L^3}{C_D^2}$ originally derived by Loyd [26].

It is interesting to also compare the magnitude of the computed sensitivities with Loyd's theory. Determining an analytic power curve based on this theory would greatly overestimate power production at high wind speeds since no tension or power constraints are present. Instead, a "characteristic" windspeed is chosen resulting in the same long-term

average power output P_{sys} as the baseline design, i.e. 11.3 kW. For the purpose of this comparison, equation 6.6 can be reduced to:

$$P_{\text{max}} = \mu \frac{C_L^3}{C_D^2} \tag{7.1}$$

where μ includes some characteristic wind speed of the power curve, air density, tether angle, component efficiencies, etc. but is independent of C_L and C_D. By matching the value of μ to the computed P_{sys}, i.e.

$$\mu = P_{\text{sys}} \frac{C_D^2}{C_L^3} \tag{7.2}$$

the analytical absolute sensitivities can be determined as:

$$\frac{\partial P_{\text{sys}}}{\partial C_L} = 3\mu \frac{C_L^2}{C_D^2} \tag{7.3}$$

$$\frac{\partial P_{\text{sys}}}{\partial C_D} = -2\mu \frac{C_L^3}{C_D^3} \tag{7.4}$$

Using the values provided tables 7.1 and 7.2 the absolute sensitivities are found to be 12.78 $\frac{W}{C_L-\text{point}}$ and 66.80 $\frac{W}{C_D-\text{point}}$-point near the baseline which is about double the values presented above. The difference is mainly due to the fact that no tension and power constraints are included in the simple analytic analysis. Additionally, the effect of mass, inertia, bounds and drag of control surfaces is that the wing cannot be flown at maximum $\frac{C_L^3}{C_D^2}$ ratio along the entire loop (which was earlier discussed in section 6.5). It is interesting that on aggregate for the case of Wing7, these effects reduce the sensitivities of the aerodynamic coefficients by half compared to the simple analytical case. Although analytic theory including constraints exists (Vanderlind [31]), it not compared for brevity.

7.2 Wing mass

In order to determine the effect of system mass, a more elaborate approach as for lift and drag above is required. Wing mass is closely coupled to the bridle geometry as the offset which is present in the geometry determines the natural tendency of the wing to roll. The bridle offset $y_{\text{br}}^{\overline{B}}$ is the offset between the projected working line of the tether on the body $Y_{\overline{B}}$ axis and center of gravity at zero tether roll angle (see section 5.1). Due to this offset, the wing naturally tends to roll without aileron input. Additional rolling motion can be achieved using the ailerons but the associated lift loss (ailerons are only allowed to reduce lift for stall reasons) significantly affects the generated power.

In order to adjust the bridle offset to the specified mass levels in the sensitivity analysis, it is optimized as a parameter together with the trajectory. This is done at a representative wind speed for the chosen wind site and subsequently fixed for all other wind speeds. This representative wind speed is taken as the wind speed with highest power probability (product of power curve and wind speed probability) for the baseline power curve being 9.2 m/s.

Table 7.3: Sensitivity of wing mass computed using bridle optimization at each mass level

added wing mass [kg]	-40	-20	-5	**0**	5	20	40
wing mass [kg]	18	38	53	**58**	63	78	98
P_{sys} [kW]	12.27	11.90	11.52	**11.39**	11.24	10.80	10.19
capacity factor [%]	52.29	50.73	49.12	**48.52**	47.91	46.02	43.41
absolute sensitivity [W/kg]	-18.45	-22.42	-25.40	**-26.39**	-27.38	-30.35	-34.32
relative sensitivity [W/%mass]	-10.70	-13.00	-14.73	**-15.31**	-15.88	-17.61	-19.91

By changing the bridle offset from a constant to a free parameter in the optimization, the optimal value can be obtained directly from the NLP solution. Such parameters, denoted with θ in the OCP formulation (eq. C.2) have only one value for the entire trajectory. Figure 7.3 shows the optimized bridle offset for a range of mass added to the wing mass at a wind speed of 9.2 m/s.

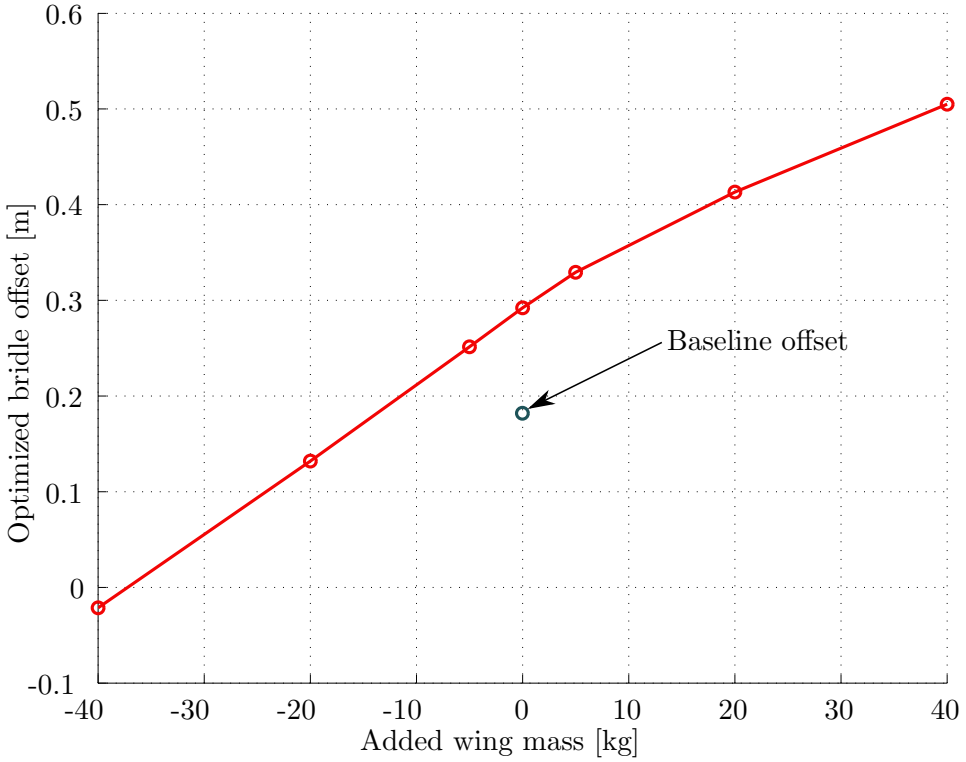

Figure 7.3: Optimized bridle offset for different levels of added wing mass for $w = 9.2$ ms^{-1}

The arrow indicates that the optimized offset is different than the baseline design. This could indicate a possible (easy) design improvement depending on how much the take-off and landing performance are affected. For consistency, the optimized bridle offset for the baseline level is used in the mass sensitivity analysis. Figure 7.4 shows the sensitivity of P_{sys} to wing mass and illustrates the need for bridle optimization. In table 7.3, the numeric sensitivities are listed which shows a relatively constant value over a wide range of wing mass with -26.4 $\frac{W}{kg}$ and -15.31 $\frac{W}{\%\text{mass}}$ near the baseline.

Comparing the relative sensitivity to the results for C_L and C_D, it is interesting to see

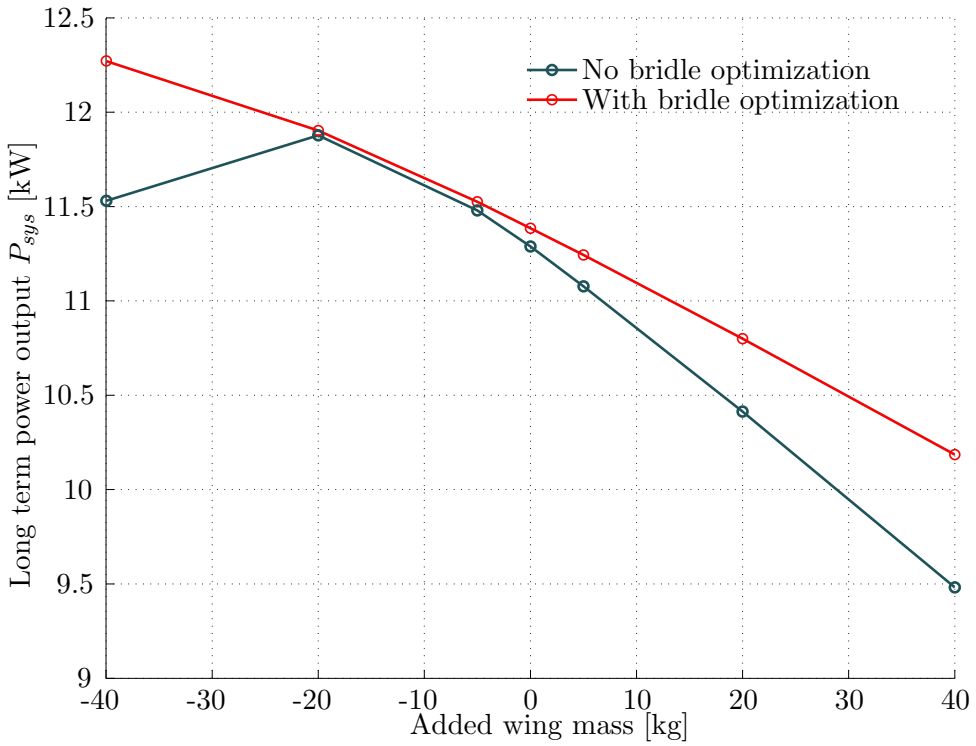

Figure 7.4: Effect of bridle optimization on mass sensitivity

that the relative sensitivity of mass is a full order of magnitude lower. Table 7.3 shows that increasing the system mass with 40kg (69% !) only reduces the power output with 10%. This conclusion has potentially great consequences for the design philosophy as currently a great focus of development within Makani is devoted to lightweight design.

However, it should be stressed that the analysis in this thesis only looks at the power generating operation mode of the system. Mass is expected to be a very sensitive parameter for hovering performance (required for take-off and landing) as it directly affects the thrust to weight ratio.

Nevertheless, it might be worth revising certain trade-offs in the structural design, especially in the light of commercial viability. One of those trade-offs is the material used for the wing spar and skins which is currently a high-strength carbon fibre composite. A significant cost saving is expected if (one of) these components could be constructed out of glass fibre based composites. Analysis of this trade-off is beyond the scope of this work as in entails a long list of considerations. One of the items of that list, the impact on power production, can be quantified using the sensitivities presented above.

7.3 Circularity of the path

A point of interest particularly useful for real world implementation is the sensitivity to circularity of the path. As an online controller will control the wing, it typically tries to keep the actual flight path on a reference one. Compared to the curve as shown in figures 6.1 and 6.2, a circular reference trajectory is significantly easier to implement.

The most straightforward way of measuring the circularity is the amount of change in curvature along the trajectory. A closed curve with no change in curvature along the curve is by definition a circle. In order to not prescribe a certain curvature but only influence the circularity of the solution the time rate of change of curvature is controlled.

For a curve $\gamma(t) \in \mathbb{R}^3$, parametrized by t, the curvature can be computed by equation 7.5 (see [64] for reference).

$$\kappa(t) = \frac{|\gamma' \times \gamma''|}{|\gamma'|^3} \tag{7.5}$$

As the flight path is parametrized by time and $\boldsymbol{\gamma(t)}$ corresponds to $\boldsymbol{r}(t)$, the derivatives γ' and γ'' represent the velocity and acceleration vector respectively. Equation 7.5 can thus be written as

$$\kappa(t) = \frac{|\boldsymbol{v} \times \boldsymbol{a}|}{|\boldsymbol{v}|^3} \tag{7.6}$$

The expression for the time rate of change of the curvature is derived below in equations 7.7 to 7.9 in which the vector $\boldsymbol{j}$ is the time rate of change of the acceleration, often reffered to as *jerk*.

$$\frac{\mathrm{d}\kappa}{\mathrm{d}t} = \frac{1}{|\boldsymbol{v}|^3}\frac{d}{dt}\left(|\boldsymbol{v} \times \boldsymbol{a}|\right) + |\boldsymbol{v} \times \boldsymbol{a}|\frac{d}{dt}\frac{1}{|\boldsymbol{v}|^3} \tag{7.7}$$

$$= \frac{1}{|\boldsymbol{v}|^3}\frac{(\boldsymbol{v} \times \boldsymbol{a}) \cdot \left(\left(\boldsymbol{v} \times \frac{d}{dt}\boldsymbol{a}\right) + (\boldsymbol{a} \times \boldsymbol{a})\right)}{|\boldsymbol{v} \times \boldsymbol{a}|} - 3\frac{|\boldsymbol{v} \times \boldsymbol{a}|\,(\boldsymbol{v} \cdot \boldsymbol{a})}{|\boldsymbol{v}|^5} \tag{7.8}$$

$$= \frac{(\boldsymbol{v} \times \boldsymbol{a}) \cdot ((\boldsymbol{v} \times \boldsymbol{j}))}{|\boldsymbol{v} \times \boldsymbol{a}||\boldsymbol{v}|^3} - 3\frac{|\boldsymbol{v} \times \boldsymbol{a}|\,(\boldsymbol{v} \cdot \boldsymbol{a})}{|\boldsymbol{v}|^5} \tag{7.9}$$

This value of $\frac{\mathrm{d}\kappa}{\mathrm{d}t}$ is computed together with the equations of motion. The optimization objective is then augmented with a penalty on the integrated value and becomes:

$$J = -\frac{E}{T} + \gamma_{cr}\boldsymbol{u}^T\boldsymbol{u} + \gamma_{\mathrm{circ}}w^3\int_0^T \frac{\mathrm{d}\kappa}{\mathrm{d}t} \tag{7.10}$$

The penalty γ_{circ} is multiplied with the cubed windspeed to approximately scale it to the average power term. Increasing the penalty leads a more constant-curvature (circular) solution.

In order to compare the circularity of different solutions the normalized standard deviation of radius of curvature σ_ρ, defined in equation 7.11 is used, measured at the discretization

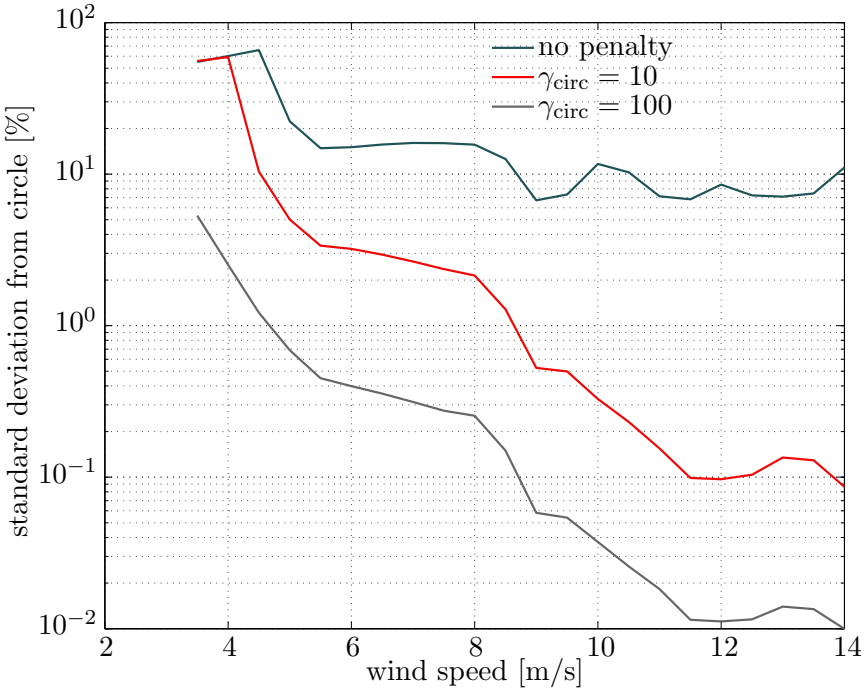

Figure 7.5: Effect of circularity penalty γ_{circ} on normalized standard deviation from mean circle radius

Table 7.4: Impact of path circularity on P_{sys}

Penalty level γ_{circ}	0	10	100
P_{sys} [kW]	11.288	11.220	11.199

nodes, where ρ is the local radius of curvature.

$$\sigma_\rho = \frac{1}{\bar{\rho}} \sqrt{\sum_{i=0}^{N-1} \frac{(\rho_i - \bar{\rho})^2}{N}} \tag{7.11}$$

Figure 7.5 shows σ_ρ for a range of wind speeds and three levels of penalization. The first observation is that the natural path circularity increases with wind speed. At 4 m/s, σ_ρ is about 60% of the mean radius while at 12 m/s this is less than 10%. Applying a penalty of $\gamma_{\text{circ}} = 100$ reduces standard deviation further to a few percent at low wind speeds and about 0.01% in stronger winds.

The impact on power output is extremely small as shown in table 7.4. Using a circular reference trajectory instead of a fully optimized curve is therefore not expected to influence power output significantly. Although more evidence is required, the low sensitivity to circularity seems to indicate a low sensitivity to the exact path position in general. As controlling the wing requires often costly control inputs, a relatively 'loosely' flown trajectory is likely better than following the reference strictly.

7.4 Path topology

Although the Wing7 system is designed for a 'circular' trajectory (winding number $N = 1$), it is interesting to investigate the effect of other topologies. As explained in chapter 3, the optimization will only find the locally optimal trajectory with the same winding number as the provided initial guess. In this section, the baseline Wing7 design (with slight modifications, discussed below) was optimized using an alternate, lying figure-eight ($N = 0$) initial guess. This is a commonly used trajectory for AWE systems since it has the advantage that the tether will not coil up after one cycle. On the other hand, since the yaw rate does not switch direction on a circular path, the system can be optimized to turn a single direction. The two most important 'unidirectional' design features of Wing7 are:

- A non-zero bridle offset which results in a rolling moment around the center of gravity due to the tether force. This leads to a natural tendency of the wing to fly a curved trajectory without any control input.
- Non-zero camber in the generator mounting structure (pylons) which causes a net side-force of the wing under zero side-slip. This counters the centripetal acceleration caused by the flight path curvature and thereby allows the wing to roll less, resulting in a more normal orientation w.r.t. the prevailing wind speed.

In order to reduce the impact of the unidirectional bias in the comparison, the bridle offset was optimized for the figure-eight trajectory in the same fashion as done for the mass sensitivity (section 7.2). The non-zero camber of the pylons however not changed.

Table 7.5 and figure 7.6 show the results for a circular and two figure-eight initial guesses. The terms "slow-climb" and "fast-climb" refer to the flight direction where the wing either climbs in the middle of the figure-eight or on the vertical sections of the figure-eight sides. The results show a relatively small difference in power output, with a reduction in capacity factor of less than 3 percentage points for the figure-eight trajectories compared to circular ones. These results suggest that the added complexity and cost of the un-coil system (incl. thrust bearing and slip ring) might not be worth it. However, it should be mentioned that the radius curvature of the optimized figure-eight solutions approaches 2 wingspans compared to a minimum of 3 wingspans for the circular trajectories. This likely exceeds the validity of the linearized aerodynamic response of the wing to yaw rate (see section 4.2.1). Additionally, controlling the wing on such curved sections is challenging.

Table 7.5: Impact of path topology on P_{sys}

Initial guess	circular	"slow climb" figure-8	"fast climb" figure-8
P_{sys} [kW]	11.39	10.75	10.69
capcity factor [%]	48.52	45.81	45.55

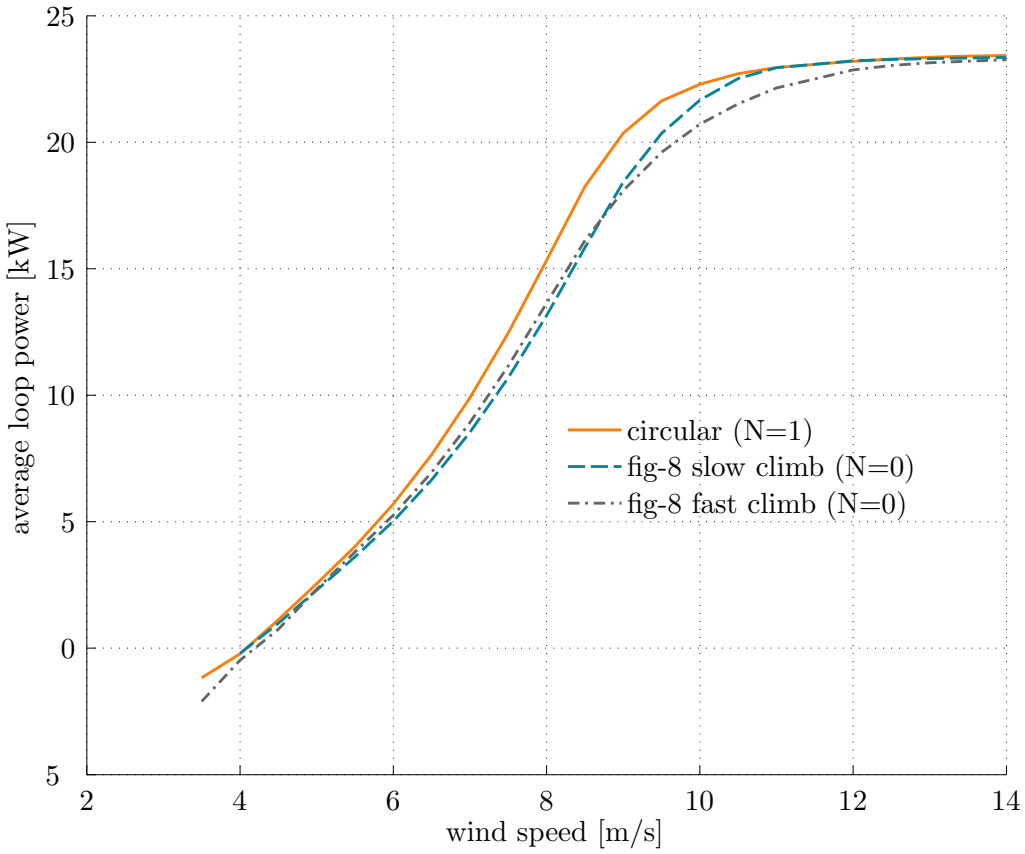

Figure 7.6: Effect of path topology on power output showing one circular and two figure-eight trajectories. N refers to the winding number

8

Conclusion and recommendations

This thesis shows that trajectory optimization is powerful and useful technique to obtain information on the sensitivity of power to design variables using fairly complex AWT model. As such, it proves a suitable approach to answer the key research question "Which design variables affect the "Wing7" airborne wind turbine power output the most and how much?".

This question is answered by computing the sensitivities of system power output for a wind site with mean annual wind speed of 7.5 ms^{-1} without wind shear. This is done by keeping the rated power of the system fixed such that the measured sensitivities are due to a change in capacity factor of the system.

The computed semirelative sensitivities near the baseline Wing7 design to lift and drag coefficient and wing mass are 159 $\frac{W}{\%C_L}$, -122 $\frac{W}{\%C_D}$ and -15.3 $\frac{W}{\%\mathrm{mass}}$ respectively. These results confirm the higher relative importance of lift compared to drag as predicted by analytic theory. Their sensitivity magnitude however is found to be about 50% compared to unconstrained theory (Loyd [26]) when assuming a characteristic windspeed resulting in the same system power output. Furthermore, the relative influence of the mass of the wing is a full order of magnitude lower than the influence of it's aerodynamic coefficients.

The computed absolute sensitivities to the same variables are 6.00 $\frac{W}{C_L-\mathrm{point}}$, -36.2 $\frac{W}{C_D-\mathrm{point}}$ (1 point = 1/1000th of unity C_L or C_D [-]) and -26.4 $\frac{W}{\mathrm{kg}}$. These values can be used directly in design trade-offs for improvements of the Wing 7 system. Keeping in mind that these results do not include the impact on take-off and landing, the main conclusions regarding the design are:

- Any aerodynamic design change targeting improved power production should occur at a $\frac{C_L}{C_D}$-ratio greater than 6.
- The sensitivity to mass of -26.4 $\frac{W}{\mathrm{kg}}$ is very low considering a total mass of 58kg (excluding tether) and power output of 11.3 kW. In light of commercial viability, the use of expensive, lightweight fibers such as carbon might not be cost-effective.

- Tether drag reduction has huge potential for improved power generation. Reducing the C_d-coefficient of the tether from 1.2 to 0.16 using a fairing is expected to increase power generation with 30%.

A secondary goal of the research is to investigate the influence of the physical path itself. Sensitivity to the circularity of the flight path is found to be very low with a decrease in capacity factor of only 0.37 percentage points when forcing the typical natural standard deviation of circularity from around 10% to less than 1%. This leads to the following qualitative conclusions regarding the real-time control system:

- Real time control on complex optimized trajectory shapes is not advised. Simple circular reference trajectories are deemed sufficient.
- Strict path-following is not advised since the expected losses arising from large control inputs will outweigh the losses due to small deviations from the reference trajectory.

Similarly, the effect of path topology is relatively low with a capacity factor reduction of less than 3 percentage points for figure-eight trajectories compared to circular ones.

Finally, the following recommendations are made for future work:

- Improve the aerodynamic model using wind tunnel data or high-fidelity CFD. Especially for high yaw rates, the linearized approach does likely not capture all relevant effects.
- Compare the analytic model of the tether with a high-fidelity tether model to validate this part of the model. Investigate tether eigenmodes and formulate constraints to avoid exciting them.
- Include a 'controllability metric' of the flight path. This would improve the flyability of the optimization results and enable them to be used for control algorithm design.
- Parametrize suitable elements of the model such as the tether diameter and length. By implementing such design variables as free parameters in the NLP, they can be optimized directly. Include constraints from other flight maneuvers such as take-off and landing if required.
- Formulate the optimization problem for the entire power curve instead of a single windspeed. This would allow parameter optimization directly on an objective function similar to P_{sys} instead of the average loop power at a 'characteristic' windspeed.

References

[1] World Bank. (2014, Feb) World development indicators. [Online]. Available: http://databank.worldbank.org/

[2] R. van der Vlugt, J. Peschel, and R. Schmehl, "Design and experimental characterization of a pumping kite power system," in *Airborne Wind Energy*, U. Ahrens, M. Diehl, and R. Schmehl, Eds. Berlin Heidelberg: Springer, 2013, ch. 23, pp. 403–425. doi:10.1007/978-3-642-39965-7

[3] R. H. Luchsinger, "Pumping cycle kite power," in *Airborne Wind Energy*, U. Ahrens, M. Diehl, and R. Schmehl, Eds. Berlin Heidelberg: Springer, 2013, ch. 3, pp. 473–490. doi:10.1007/978-3-642-39965-7_3

[4] B. Etkin, *Dynamics of Flight*. John Wiley and Sons, Inc., 1967.

[5] M. Canale, L. Fagiano, and M. Milanese, "Kitegen: A revolution in wind energy generation," *Energy*, vol. 34, no. 3, pp. 355 – 361, 2009. doi:10.1016/j.energy.2008.10.003

[6] Ampyx Power. (2013, March) Power plane. [Online]. Available: http://www.ampyxpower.com/PowerPlane.html

[7] Makani Power, Inc. (2013, March) What is airborne wind power? [Online]. Available: http://www.makanipower.com/what-is-airborne-wind/

[8] U.N. Department of Economic and Social Affairs, Population Division, "World population prospects: The 2012 revision, highlights and advance tables," 2013. [Online]. Available: http://esa.un.org/wpp/Documentation/pdf/WPP2012_HIGHLIGHTS.pdf

[9] U.S. Energy Information Administration, Office of Energy Analysis, "International energy outlook 2013," 2013. [Online]. Available: http://www.eia.gov/forecasts/ieo/

[10] T. Stocker, D. Qin, G.-K. Plattner, M. Tignor, S. Allen, J. B. A. Nauels, Y. Xia, V. Bex, and P. M. (eds.), *Climate Change 2013: The Physical Science Basis. Contribution of Working Group I to the Fifth Assessment Report of the Intergovernmental*

Panel on Climate Change. Cambridge, United Kingdom and New York, NY, USA: Cambridge University Press, 2013.

[11] Dr. Pieter Tans, NOAA/ESRL and Dr. Ralph Keeling, Scripps Institution of Oceanography. (2014, Feb) Atmospheric co2 at mauna lao observatory. [Online]. Available: www.esrl.noaa.gov/gmd/ccgg/trends/

[12] S. Randalls, "History of the 2°C climate target," *Wiley Interdisciplinary Reviews: Climate Change*, vol. 1, no. 4, pp. 598–605, 2010. doi:10.1002/wcc.62

[13] U.N. Framework Convention on Climate Change, "Copenhagen Accord, Draft decision-/CP. 15," in *Conference of the Parties, Fifteenth Session, Copenhagen*, 2009. [Online]. Available: http://unfccc.int/resource/docs/2009/cop15/eng/l07.pdf

[14] J. Hansen, P. Kharecha, M. Sato, V. Masson-Delmotte, F. Ackerman *et al.*, "Assessing "Dangerous Climate Chang": Required Reduction of Carbon Emissions to Protect Young People, Future Generations and Nature," *PloS one*, vol. 8, no. 12, 2013. doi:10.1371/journal.pone.0081648

[15] E. Lantz, R. Wiser, and M. Hand, "The past and future cost of wind energy," *IEA wind task*, vol. 26, 2012.

[16] U.S. Energy Information Administration. (2014, Feb) Annual energy outlook 2013. [Online]. Available: http://www.eia.gov/forecasts/aeo/electricity_generation.cfm

[17] C. L. Archer and K. Caldeira, "Global assessment of high-altitude wind power," *Energies*, vol. 2, no. 2, pp. 307–319, 2009. doi:10.3390/en20200307

[18] B. W. Roberts, D. H. Shepard, K. Caldeira, M. E. Cannon, D. G. Eccles, A. J. Grenier, and J. F. Freidin, "Harnessing high-altitude wind power," *Energy Conversion, IEEE Transactions on*, vol. 22, no. 1, pp. 136–144, 2007. doi:10.1109/TEC.2006.889603

[19] U. Ahrens, M. Diehl, and R. Schmehl, Eds., *Airborne Wind Energy*. Springer, 2013. doi:10.1007/978-3-642-39965-7

[20] SwissKitePower. [Online]. Available: http://www.swisskitepower.ch/

[21] S. GmbH. (2013) Skysails website. [Online]. Available: http://www.skysails.info/english/media/photos-and-graphics/mv-bbc-skysails/

[22] KiteGen Research. [Online]. Available: http://www.kitegen.com/en/

[23] S. Gros and M. Diehl, "Modeling of airborne wind energy systems in natural coordinates," in *Airborne Wind Energy*, U. Ahrens, M. Diehl, and R. Schmehl, Eds. Berlin Heidelberg: Springer, 2013, pp. 181–203. doi:10.1007/978-3-642-39965-7_10

[24] G. Horn, "Numerical trajectory optimization for airborne wind energy systems described by high fidelity aircraft models," in *Airborne Wind Energy*, U. Ahrens, M. Diehl, and R. Schmehl, Eds. Berlin Heidelberg: Springer, 2013, ch. 11, pp. 205–218. doi:10.1007/978-3-642-39965-7_11

[25] ——. RAWESOME Airborne Wind Energy Simulation, Optimization and Modeling Environment. [Online]. Available: github.com/ghorn/rawesome

[26] M. L. Loyd, "Crosswind kite power," *Journal of Energy*, vol. 4, no. 3, pp. 106–111, 1980. doi:10.2514/3.48021

[27] W. J. Ockels, "Laddermill, a novel concept to exploit the energy in the airspace," *Aircraft Design*, vol. 4, no. 2-3, pp. 81 – 97, 2001. doi:10.1016/S1369-8869(01)00002-7

[28] I. Argatov, P. Rautakorpi, and R. Silvennoinen, "Estimation of the mechanical energy output of the kite wind generator," *Renewable Energy*, vol. 34, no. 6, pp. 1525–1532, 2009. doi:10.1016/j.renene.2008.11.001

[29] J. Breuer and R. H. Luchsinger, "Inflatable kites using the concept of tensairity," *Aerospace Science and Technology*, vol. 14, no. 8, pp. 557–563, 2010. doi:10.1016/j.ast.2010.04.009

[30] R. v. d. V. Roland Schmehl, Michael Noom, "Traction power generation with tethered wings," in *Airborne Wind Energy*, U. Ahrens, M. Diehl, and R. Schmehl, Eds. Berlin Heidelberg: Springer, 2013, pp. 23–45.

[31] D. Vander Lind, "Analysis and flight test validation of high performance airborne wind turbines," in *Airborne Wind Energy*, U. Ahrens, M. Diehl, and R. Schmehl, Eds. Berlin Heidelberg: Springer, 2013, ch. 28, pp. 473–490. doi:10.1007/978-3-642-39965-7_28

[32] J. Breukels, "An engineering methodology for kite design," Ph.D. dissertation, Delft University of Technology, 2011.

[33] E. Terink, J. Breukels, R. Schmehl, and W. Ockels, "Flight dynamics and stability of a tethered inflatable kiteplane," *Journal of Aircraft*, vol. 48, no. 2, pp. 503–513, 2011. doi:10.2514/1.C031108

[34] S. de Groot, J. Breukels, R. Schmehl, and W. Ockels, "Modelling kite flight dynamics using a multibody reduction approach," *Journal of Guidance, Control, and Dynamics*, vol. 34, no. 6, pp. 1671–1682, 2011. doi:10.2514/1.52686

[35] D. T. Greenwood, *Principles of Dynamics*. Englewood Cliffs, NJ: Prentice-Hall Inc., 1988.

[36] B. Houska and M. Diehl, "Optimal control for power generating kites," in *European Control Conference*, 2007.

[37] P. Williams, B. Lansdorp, and W. Ockesl, "Optimal crosswind towing and power generation with tethered kites," *Journal of guidance, control, and dynamics*, vol. 31, no. 1, pp. 81–93, 2008. doi:10.2514/1.30089

[38] E. Terink, "Kiteplane Flight Dynamics - Stability and control analysis of tethered flight for power generation purposes," Master's thesis, Delft University of Technology, 2009.

[39] J. Andersson, J. Åkesson, and M. Diehl, "Casadi: A symbolic package for automatic differentiation and optimal control," in *Recent Advances in Algorithmic Differentiation*. Springer, 2012, pp. 297–307. doi:10.1007/978-3-642-30023-3_27

[40] S. Gros, M. Zanon, and M. Diehl, "Orbit control for a power generating airfoil based on nonlinear MPC," in *American Control Conference (ACC), 2012*. IEEE, 2012, pp. 137–142.

[41] N. V. Queipo, R. T. Haftka, W. Shyy, T. Goel, R. Vaidyanathan, and P. K. Tucker, "Surrogate-based analysis and optimization," *Progress in Aerospace Sciences*, vol. 41, no. 1, pp. 1 – 28, 2005. doi:10.1016/j.paerosci.2005.02.001

[42] D. C. Wilcox, *Turbulence modeling for CFD*. La Canada, CA: DCW industries, 1998, vol. 2.

[43] R. D. Moser, J. Kim, and N. N. Mansour, "Direct numerical simulation of turbulent channel flow up to Re_τ=590," *Phys. Fluids*, vol. 11, no. 4, pp. 943–945, 1999. doi:10.1063/1.869966

[44] P. Sagaut and S. Deck, "Large eddy simulation for aerodynamics: status and perspectives," *Philosophical Transactions of the Royal Society A: Mathematical, Physical and Engineering Sciences*, vol. 367, no. 1899, pp. 2849–2860, 2009. doi:10.1098/rsta.2008.0269

[45] J. Hess, "Panel methods in computational fluid dynamics," *Annual Review of Fluid Mechanics*, vol. 22, no. 1, pp. 255–274, 1990. doi:10.1146/annurev.fluid.22.1.255

[46] B. Maskew, *PROGRAM VSAERO: A computer program for calculating the nonlinear aerodynamic characteristics of arbitrary configurations: User's manual*, 1982.

[47] M. Drela and H. Youngren, "AVL - Aerodynamic Analysis, Trim Calculation, Dynamic Stability Analysis, Aircraft Configuration Development," 2006. [Online]. Available: http://web.mit.edu/drela/Public/web/avl/

[48] M. Noom, "Theoretical analysis of mechanical power generation by pumping cycle," Master's thesis, Delft University of Technology, May 2013.

[49] J. Breukels and W. Ockels, "A multi-body dynamics approach to a cable simulation for kites," in *Proceedings of the IASTED Asian Conference on Modelling and Simulation*. ACTA Press, 2007, pp. 168–173. [Online]. Available: http://www.kitepower.eu/publications.html

[50] P. Williams and P. Trivailo, "Dynamics of Circularly Towed Aerial Cable Systems, Part I: Optimal Configurations and Their Stability," *Journal of guidance, control, and dynamics*, vol. 30, no. 3, pp. 753–765, 2007. doi:10.2514/1.20433

[51] O. von Stryk and R. Bulirsch, "Direct and indirect methods for trajectory optimization," *Annals of Operations Research*, vol. 37, no. 1, pp. 357–373, 1992. doi:10.1007/BF02071065

[52] A. Wächter and L. T. Biegler, "On the implementation of an interior-point filter line-search algorithm for large-scale nonlinear programming," *Mathematical programming*, vol. 106, no. 1, pp. 25–57, 2006. doi:10.1007/s10107-004-0559-y

[53] P. E. Gill, W. Murray, and M. A. Saunders, "SNOPT: An SQP algorithm for large-scale constrained optimization," *SIAM Journal on Optimization*, vol. 12, no. 4, pp. 979–1006, 2002. doi:10.1137/S1052623499350013

[54] M. Diehl, H. G. Bock, H. Diedam, and P.-B. Wieber, "Fast direct multiple shooting algorithms for optimal robot control," in *Fast motions in biomechanics and robotics*. Springer, 2006, ch. 4, pp. 65–93. doi:10.1007/978-3-540-36119-0_4

[55] J. T. Betts, *Practical methods for optimal control and estimation using nonlinear programming*. Society for Industrial and Applied Mathematics, 2009, vol. 19. doi:dx.doi.org/10.1137/1.9780898718577

[56] F. Fahroo and I. M. Ross, "Direct trajectory optimization by a Chebyshev pseudospectral method," *Journal of Guidance, Control, and Dynamics*, vol. 25, no. 1, pp. 160–166, 2002. doi:10.2514/2.4862

[57] E. D. Smith, F. Szidarovszky, W. J. Karnavas, and A. Bahill, "Sensitivity analysis, a powerful system validation technique," *Open Cybernetics & Systemics Journal*, vol. 2, pp. 39–56, 2008.

[58] J. P. Kleijnen, "An overview of the design and analysis of simulation experiments for sensitivity analysis," *European Journal of Operational Research*, vol. 164, no. 2, pp. 287–300, 2005. doi:10.1016/j.ejor.2004.02.005

[59] M. Canale, L. Fagiano, and M. Milanese, "High altitude wind energy generation using controlled power kites," *IEEE Transactions on Control Systems Technology*, vol. 18, no. 2, pp. 279–293, 2010. doi:10.1109/TCST.2009.2017933

[60] M. Drela. Qprop formulation. [Online]. Available: http://web.mit.edu/drela/Public/web/qprop/qprop_theory.pdf

[61] Maxon Motors AG. Maxon dc motor and maxon ec motor - key information. [Online]. Available: http://goo.gl/X9qYBA

[62] C. L. Archer and M. Z. Jacobson, "Spatial and temporal distributions of us winds and wind power at 80 m derived from measurements," *Journal of Geophysical Research: Atmospheres (1984–2012)*, vol. 108, no. D9, 2003.

[63] J. Henderson, "Some towing problems with faired cables," *Ocean Engineering*, vol. 5, no. 2, pp. 105–125, 1978.

[64] A. Gray, *Modern Differential Geometry of Curves and Surfaces with Mathematica*. CRC Press, 1997, ch. 8, p. 192.

[65] K. B. Petersen and M. S. Pedersen, "The matrix cookbook," 2006, Technical University of Denmark. [Online]. Available: www.mit.edu/~wingated/stuff_i_use/matrix_cookbook.pdf

[66] L. Euler, "Découverte d'un nouveau principe de la mécanique," *Mémoires de l'Académie des Sciences de Berlin*, vol. 6, pp. 185–217, 1752.

Appendix A

Direction cosine matrices

This appendix tries to briefly explain the concept of a direct cosine matrix (DCM) as a method to describe rotations between different reference frames. It is based on the textbook [35]. The purpose of any rotation formalism in the scope of this text is to describe a certain vector quantity in Euclidean space, here denoted with $\boldsymbol{r} \in \mathbb{R}$, in two reference frames with a different orthonormal basis, denoted E_E and E_B.

The *direction cosines* of $\boldsymbol{r}$ in E_E are the cosines of the angles between $\boldsymbol{r}$ and the basis vectors of E_E. Equivalently, they are the subsequent projections of $\boldsymbol{r}$ on the basis vectors of E_E. Assuming $\{\boldsymbol{e}_1, \boldsymbol{e}_2, \boldsymbol{e}_3\}$ are the unit vectors which span E_E, then the scalars $\{r_{e1}, r_{e2}, r_{e3}\}$ are the direction cosines, such that:

$$\boldsymbol{r}^E = r_{e1}\boldsymbol{e}_1 + r_{e2}\boldsymbol{e}_2 + r_{e3}\boldsymbol{e}_3 \tag{A.1}$$

Assuming $\{\boldsymbol{b}_1, \boldsymbol{b}_2, \boldsymbol{b}_3\}$ are the unit vectors which span E_B, the unit vectors of E_E itself can be expressed in terms of E_B using direction cosines:

$$\begin{aligned} \boldsymbol{e}_1 &= c_{1'1}\boldsymbol{b}_1 + c_{2'1}\boldsymbol{b}_2 + c_{3'1}\boldsymbol{b}_3 \\ \boldsymbol{e}_2 &= c_{1'2}\boldsymbol{b}_1 + c_{2'2}\boldsymbol{b}_2 + c_{3'2}\boldsymbol{b}_3 \\ \boldsymbol{e}_3 &= c_{1'3}\boldsymbol{b}_1 + c_{2'3}\boldsymbol{b}_2 + c_{3'3}\boldsymbol{b}_3 \end{aligned} \tag{A.2}$$

Where the scalars $c_{i'j}$ represents the cosine of the angle between the i^{th} unit vector of E_B and the j^{th} unit vector of E_E. Using the coefficients, the vector $\boldsymbol{r}$ can now be expressed in the E_B frame in the following way:

$$\begin{aligned} \boldsymbol{r}^B = &\left(c_{1'1}r_{e1} + c_{1'2}r_{e2} + c_{1'3}r_{e3}\right)\boldsymbol{b}_1 \\ &+ \left(c_{2'1}r_{e1} + c_{2'2}r_{e2} + c_{2'3}r_{e3}\right)\boldsymbol{b}_2 \\ &+ \left(c_{3'1}r_{e1} + c_{3'2}r_{e2} + c_{3'3}r_{e3}\right)\boldsymbol{b}_3 \end{aligned} \tag{A.3}$$

By close inspection of equation A.3 one can see that the component in the direction of a unit vector $\boldsymbol{b}_i$ is the collection of the projections of $\{r_{e1}\boldsymbol{e}_1, r_{e2}\boldsymbol{e}_2, r_{e3}\boldsymbol{e}_3\}$ on the unit vector $\boldsymbol{b}_i$.
Finally, equation A.3 is written in matrix notation to obtain:

$$\begin{bmatrix} r_1^B \\ r_2^B \\ r_3^B \end{bmatrix} = \begin{bmatrix} c_{1'1} & c_{1'2} & c_{1'3} \\ c_{2'1} & c_{2'2} & c_{2'3} \\ c_{3'1} & c_{3'2} & c_{3'3} \end{bmatrix} \begin{bmatrix} r_1^E \\ r_2^E \\ r_3^E \end{bmatrix} \tag{A.4}$$

Which in short notation reduces to:

$$\boldsymbol{r}^B = \boldsymbol{R}_{BE}\, \boldsymbol{r}^E \tag{A.5}$$

where the *direct cosine matrix* $\boldsymbol{R}_{BE}$ is used to denote the rotation matrix **from** E_E **to** E_B.

Using an equivalent derivation, it can be shown that:

$$\boldsymbol{R}_{BE}^{-1} = \boldsymbol{R}_{BE}^T = \boldsymbol{R}_{EB} \tag{A.6}$$

The fact that $\boldsymbol{R}_{BE}^{-1} = \boldsymbol{R}_{BE}^T$, proves that rotation matrices are orthogonal, which is used in section B.3 to reduce the number of equations of motion.

Appendix B

Equations of Motion

The detailed derivation of the equations of motion are given here. The derivation is very similar and strongly based on the beautiful mathematical work of Gros and Diehl [23]. The key difference is the treatment of the tether which is not implemented as a constraint but as a straight, elastic element. Following the Lagrangian formalism (equation 5.6, repeated below), each term is discussed separately in the sections below.

$$\frac{d}{dt}\left(\frac{\partial \mathcal{L}}{\partial \dot{q}_j}\right) - \frac{\partial \mathcal{L}}{\partial q} = Q_j \tag{B.1}$$

The Lagrangian was constructed in section 5.2 and is repeated below from equation 5.14:

$$\mathcal{L} = \underbrace{\left[\frac{1}{2}\left(\boldsymbol{\omega}^T \boldsymbol{J} \boldsymbol{\omega}\right) + \frac{1}{2}\left(\dot{\boldsymbol{r}}^T m_{\text{in}} \dot{\boldsymbol{r}}\right)\right]}_{\text{kinetic energy } T} - \underbrace{\left[\frac{1}{2} k_t \left(\left(\left(\boldsymbol{r} + \boldsymbol{R}\boldsymbol{r}_{\text{br}}^{\overline{B}}\right)^T \left(\boldsymbol{r} + \boldsymbol{R}\boldsymbol{r}_{\text{br}}^{\overline{B}}\right)\right)^{1/2} - l_{t0}\right)^2 + m_k g z\right]}_{\text{potential energy } V} \tag{B.2}$$

As all math is performed keeping the column vector and matrix notation of $\boldsymbol{r}$ and $\boldsymbol{R}$ respectively, the derivation below relies on vector calculus (see example [65] for reference). The partial operator $\frac{\partial}{\partial q_j}$ is therefore replaced by the *del* operators $\nabla_{\boldsymbol{r}}$ and $\nabla_{\boldsymbol{R}}$.

B.1 Operators definition

Before proceeding, a few mathematical operators are required. They are defined in [23], and repeated here for readability.

The *skew* operator $.\times \mathbb{R}^3 \rightarrow \mathbb{R}^{3\times 3}$ is defined as in B.3

$$\boldsymbol{a}_\times = \begin{bmatrix} 0 & -a_3 & a_2 \\ a_3 & 0 & -a_1 \\ -a_2 & a_1 & 0 \end{bmatrix} \tag{B.3}$$

Similarly the *unskew* operator $U : \mathbb{R}^{3\times3} \to \mathbb{R}^3$ is then defined as in equation B.4

$$U\left(\begin{bmatrix} a_{11} & a_{12} & a_{13} \\ a_{21} & a_{22} & a_{23} \\ a_{31} & a_{32} & a_{33} \end{bmatrix}\right) = \frac{1}{2}\begin{bmatrix} a_{32} - a_{23} \\ a_{13} - a_{31} \\ a_{21} - a_{12} \end{bmatrix}, \; U(\boldsymbol{a}_\times) = \boldsymbol{a} \tag{B.4}$$

Lastly the operator $P_{\boldsymbol{R}}(A) : \mathbb{R}^{3\times3} \to \mathbb{R}^3$

$$P_{\boldsymbol{R}}(A) = U(R^T A) \tag{B.5}$$

B.2 Derivative $\frac{\partial \mathcal{L}}{\partial q_j}$

Taking the partial derivative to the generalized coordinates: $\frac{\partial \mathcal{L}}{\partial \boldsymbol{q}_j}$.

B.2.1 Partial derivative to R

Starting with $\nabla_{\boldsymbol{R}} \mathcal{L}$

$$\nabla_{\boldsymbol{R}} T = \nabla_{\boldsymbol{R}} \left[\frac{1}{2}\left(\boldsymbol{\omega}^T \boldsymbol{J} \boldsymbol{\omega}\right)\right]$$

$$\nabla_{\boldsymbol{R}} V = k_t \left[\left(\left(\boldsymbol{r} + \boldsymbol{R}\boldsymbol{r}_{\mathrm{br}}^{\overline{B}}\right)^T \left(\boldsymbol{r} + \boldsymbol{R}\boldsymbol{r}_{\mathrm{br}}^{\overline{B}}\right)\right)^{1/2} - l_{t0}\right] \nabla_{\boldsymbol{R}} \left(\left(\boldsymbol{r} + \boldsymbol{R}\boldsymbol{r}_{\mathrm{br}}^{\overline{B}}\right)^T \left(\boldsymbol{r} + \boldsymbol{R}\boldsymbol{r}_{\mathrm{br}}^{\overline{B}}\right)\right)^{1/2}$$

Applying the chain rule:

$$\begin{aligned} \nabla_{\boldsymbol{R}} \left(\left(\boldsymbol{r} + \boldsymbol{R}\boldsymbol{r}_{\mathrm{br}}^{\overline{B}}\right)^T \left(\boldsymbol{r} + \boldsymbol{R}\boldsymbol{r}_{\mathrm{br}}^{\overline{B}}\right)\right)^{1/2} =& \frac{1}{2}\left(\left(\boldsymbol{r} + \boldsymbol{R}\boldsymbol{r}_{\mathrm{br}}^{\overline{B}}\right)^T \left(\boldsymbol{r} + \boldsymbol{R}\boldsymbol{r}_{\mathrm{br}}^{\overline{B}}\right)\right)^{-1/2} \dots \\ & \nabla_{\boldsymbol{R}} \left(\left(\boldsymbol{r} + \boldsymbol{R}\boldsymbol{r}_{\mathrm{br}}^{\overline{B}}\right)^T \left(\boldsymbol{r} + \boldsymbol{R}\boldsymbol{r}_{\mathrm{br}}^{\overline{B}}\right)\right) \end{aligned}$$

Expanding the last term:

$$\begin{aligned} \nabla_{\boldsymbol{R}} \left(\left(\boldsymbol{r} + \boldsymbol{R}\boldsymbol{r}_{\mathrm{br}}^{\overline{B}}\right)^T \left(\boldsymbol{r} + \boldsymbol{R}\boldsymbol{r}_{\mathrm{br}}^{\overline{B}}\right)\right) &= \nabla_{\boldsymbol{R}} \left(\left(\boldsymbol{r}^T + \boldsymbol{r}_{\mathrm{br}}^{\overline{B}\,T} \boldsymbol{R}^T\right)\left(\boldsymbol{r} + \boldsymbol{R}\boldsymbol{r}_{\mathrm{br}}^{\overline{B}}\right)\right) \\ &= \nabla_{\boldsymbol{R}} \left(\boldsymbol{r}^T\boldsymbol{r} + \boldsymbol{r}^T\boldsymbol{R}\boldsymbol{r}_{\mathrm{br}}^{\overline{B}} + \boldsymbol{r}_{\mathrm{br}}^{\overline{B}\,T}\boldsymbol{R}^T\boldsymbol{r} + \boldsymbol{r}_{\mathrm{br}}^{\overline{B}\,T}\boldsymbol{R}^T\boldsymbol{R}\boldsymbol{r}_{\mathrm{br}}^{\overline{B}}\right) \\ &= \nabla_{\boldsymbol{R}} \left(\boldsymbol{r}^T\boldsymbol{r} + \left(2\boldsymbol{r}^T\boldsymbol{R}\boldsymbol{r}_{\mathrm{br}}^{\overline{B}}\right) + \boldsymbol{r}_{\mathrm{br}}^{\overline{B}\,T}\boldsymbol{r}_{\mathrm{br}}^{\overline{B}}\right) \\ &= 2\left(\boldsymbol{r}\boldsymbol{r}_{\mathrm{br}}^{\overline{B}\,T}\right) \end{aligned}$$

Recombining the equation:

$$\begin{aligned}\nabla_{\boldsymbol{R}} V &= k_t \underbrace{\left[1 - \frac{l_{t0}}{\left(\left(\boldsymbol{r} + \boldsymbol{R}\boldsymbol{r}_{\mathrm{br}}^{\overline{B}}\right)^T \left(\boldsymbol{r} + \boldsymbol{R}\boldsymbol{r}_{\mathrm{br}}^{\overline{B}}\right)\right)^{1/2}}\right]}_{\lambda} \left(\boldsymbol{r}\boldsymbol{r}_{\mathrm{br}}^{\overline{B}\,T}\right) \\ &= k_t \lambda \left(\boldsymbol{r}\boldsymbol{r}_{\mathrm{br}}^{\overline{B}\,T}\right) \end{aligned} \tag{B.6}$$

The resulting expression is the matrix $\left(\boldsymbol{r}\boldsymbol{r}_{\mathrm{br}}^{\overline{B}\,T}\right)$ multiplied with a scalar $k_t\lambda$.
Equation B.7 shows the intermediate result which will be used later in section B.4

$$\nabla_{\boldsymbol{R}} \mathcal{L} = \nabla_{\boldsymbol{R}} \left[\frac{1}{2}\left(\boldsymbol{\omega}^T \boldsymbol{J} \boldsymbol{\omega}\right)\right] - k_t \lambda \left(\boldsymbol{r}\boldsymbol{r}_{\mathrm{br}}^{\overline{B}\,T}\right) \tag{B.7}$$

B.2.2 Partial derivative to r

$$\begin{aligned}\nabla_{\boldsymbol{r}} T =& 0 \\ \nabla_{\boldsymbol{r}} V =& k_t \left[\left(\left(\boldsymbol{r} + \boldsymbol{R}\boldsymbol{r}_{\mathrm{br}}^{\overline{B}}\right)^T \left(\boldsymbol{r} + \boldsymbol{R}\boldsymbol{r}_{\mathrm{br}}^{\overline{B}}\right)\right)^{1/2} - l_{t0}\right] \dots \\ & \nabla_{\boldsymbol{r}} \left(\left(\boldsymbol{r} + \boldsymbol{R}\boldsymbol{r}_{\mathrm{br}}^{\overline{B}}\right)^T \left(\boldsymbol{r} + \boldsymbol{R}\boldsymbol{r}_{\mathrm{br}}^{\overline{B}}\right)\right)^{1/2} + m_k g \mathbf{1}_3\end{aligned}$$

Applying the chain rule on the last term:

$$\begin{aligned}\nabla_{\boldsymbol{r}} \left(\left(\boldsymbol{r} + \boldsymbol{R}\boldsymbol{r}_{\mathrm{br}}^{\overline{B}}\right)^T \left(\boldsymbol{r} + \boldsymbol{R}\boldsymbol{r}_{\mathrm{br}}^{\overline{B}}\right)\right)^{1/2} =& \frac{1}{2}\left(\left(\boldsymbol{r} + \boldsymbol{R}\boldsymbol{r}_{\mathrm{br}}^{\overline{B}}\right)^T \left(\boldsymbol{r} + \boldsymbol{R}\boldsymbol{r}_{\mathrm{br}}^{\overline{B}}\right)\right)^{-1/2} \dots \\ & \nabla_{\boldsymbol{r}} \left(\left(\boldsymbol{r} + \boldsymbol{R}\boldsymbol{r}_{\mathrm{br}}^{\overline{B}}\right)^T \left(\boldsymbol{r} + \boldsymbol{R}\boldsymbol{r}_{\mathrm{br}}^{\overline{B}}\right)\right)\end{aligned}$$

Expanding the last term again (fourth step assumes that the transpose of R is equal to it's inverse)

$$\begin{aligned}\nabla_{\boldsymbol{r}} \left(\left(\boldsymbol{r} + \boldsymbol{R}\boldsymbol{r}_{\mathrm{br}}^{\overline{B}}\right)^T \left(\boldsymbol{r} + \boldsymbol{R}\boldsymbol{r}_{\mathrm{br}}^{\overline{B}}\right)\right) &= \nabla_{\boldsymbol{r}} \left(\left(\boldsymbol{r}^T + \boldsymbol{r}_{\mathrm{br}}^{\overline{B}\,T} \boldsymbol{R}^T\right)\left(\boldsymbol{r} + \boldsymbol{R}\boldsymbol{r}_{\mathrm{br}}^{\overline{B}}\right)\right) \\ &= \nabla_{\boldsymbol{r}} \left(\boldsymbol{r}^T\boldsymbol{r} + \boldsymbol{r}^T\boldsymbol{R}\boldsymbol{r}_{\mathrm{br}}^{\overline{B}} + \boldsymbol{r}_{\mathrm{br}}^{\overline{B}\,T}\boldsymbol{R}^T\boldsymbol{r} + \boldsymbol{r}_{\mathrm{br}}^{\overline{B}\,T}\boldsymbol{R}^T\boldsymbol{R}\boldsymbol{r}_{\mathrm{br}}^{\overline{B}}\right) \\ &= \nabla_{\boldsymbol{r}} \left(\boldsymbol{r}^T\boldsymbol{r} + \boldsymbol{r}^T\boldsymbol{R}\boldsymbol{r}_{\mathrm{br}}^{\overline{B}} + \boldsymbol{r}_{\mathrm{br}}^{\overline{B}\,T}\boldsymbol{R}^T\boldsymbol{r}\right) \\ &= \nabla_{\boldsymbol{r}} \left(\boldsymbol{r}^T\boldsymbol{r} + 2\boldsymbol{r}_{\mathrm{br}}^{\overline{B}\,T}\boldsymbol{R}^T\boldsymbol{r}\right) \\ &= \nabla_{\boldsymbol{r}} \left(\boldsymbol{r}^T\boldsymbol{r}\right) + 2\boldsymbol{r}_{\mathrm{br}}^{\overline{B}\,T}\boldsymbol{R}^T \\ &= 2\boldsymbol{r}^T + 2\boldsymbol{r}_{\mathrm{br}}^{\overline{B}\,T}\boldsymbol{R}^T\end{aligned}$$

The result is a row-vector. Since the vectors r^T and $2r_T^T R^T$ 'contain' the unit vectors of the inertial frame, this is equivalent to column vector. Combining the equations results in equation B.8 which also defines the variable λ.

$$\nabla_{\boldsymbol{r}}\mathcal{L} = -k_t \underbrace{\left[1 - \frac{l_{t0}}{\left(\left(\boldsymbol{r} + \boldsymbol{R}\boldsymbol{r}_{\mathrm{br}}^{\overline{B}}\right)^T \left(\boldsymbol{r} + \boldsymbol{R}\boldsymbol{r}_{\mathrm{br}}^{\overline{B}}\right)\right)^{1/2}}\right]}_{\lambda} \left(\boldsymbol{r}^T + \boldsymbol{r}_{\mathrm{br}}^{\overline{B}\,T}\boldsymbol{R}^T\right)^T + m_k g \mathbf{1}_3 \tag{B.8}$$

$$= -k_t \lambda \left(\boldsymbol{r}^T + \boldsymbol{r}_{\mathrm{br}}^{\overline{B}\,T}\boldsymbol{R}^T\right)^T + m_k g \mathbf{1}_3 \tag{B.9}$$

$$= -k_t \lambda \left(\boldsymbol{r} + \boldsymbol{R}\boldsymbol{r}_{\mathrm{br}}^{\overline{B}}\right) + m_k g \mathbf{1}_3 \tag{B.10}$$

This makes sense as $k\lambda$ is the force in the tether per unit length (very similar to Lagrange multipliers!) and $\left(\boldsymbol{r} + \boldsymbol{R}\boldsymbol{r}_{\mathrm{br}}^{\overline{B}}\right)$ has the length of the tether as norm.

B.3 Derivative $\frac{d}{dt}\frac{\partial \mathcal{L}}{\partial \dot{q}_j}$

Again the derivation is performed keeping the vector and matrix notation of the generalized coordinates. The derivation of $\frac{d}{dt}\nabla_{\dot{\boldsymbol{R}}}\mathcal{L}$ and $\frac{d}{dt}\nabla_{\dot{\boldsymbol{r}}}\mathcal{L}$ is performed below. As the rotational part of the Lagrangian was not explicitly formulated in the generalized coordinate $\boldsymbol{R}$ but in terms of $\boldsymbol{\omega}$ a relation between them is required. As shown in [23], their relation can be expressed as in equation B.11 where the subscript $\times$ denotes the skew operator.

$$\dot{\boldsymbol{R}} = \boldsymbol{R}\boldsymbol{\omega}_{\times} \tag{B.11}$$

Equation B.11 allows the derivation of the equations of motion in terms of $\boldsymbol{\omega}$ which then in turn determines the time derivative of the DCM. As the vector of body angular rates determine only the time evolution of the matrix $\boldsymbol{R}$, they do not fully determine the shape of the DCM. Since the columns of the DCM represent the unit vectors of the body reference frame, the DCM has to be orthogonal (see appendix A). Therefore, the condition given by equation B.12 must be applied at some time during the trajectory.

$$\boldsymbol{R}^T\boldsymbol{R} - \boldsymbol{I} = 0 \tag{B.12}$$

Although the rotational rates of the body can now be expressed in the more convenient quantity $\boldsymbol{\omega}$ instead of $\dot{\boldsymbol{R}}$, this does not mean that the choice of generalized coordinates has changed. Therefore, proceeding with the Lagrangian formalism, the derivative $\frac{d}{dt}\nabla_{\dot{\boldsymbol{R}}}\mathcal{L}$ is evaluated. For reasons which will become apparent in section B.4, the term involving $\dot{\boldsymbol{R}}$ is not expanded further than shown in B.13.

$$\frac{d}{dt}\nabla_{\dot{\boldsymbol{R}}}\mathcal{L} = \nabla_{\dot{\boldsymbol{R}}}\left[\frac{1}{2}\left(\boldsymbol{\omega}^T\boldsymbol{J}\boldsymbol{\omega}\right)\right] \tag{B.13}$$

Inspection the contribution of $\dot{\boldsymbol{r}}$ to the kinetic and potential energy in (5.14) results in equation B.14.

$$\frac{d}{dt}\nabla_{\dot{\boldsymbol{r}}}\mathcal{L} = m_{\text{in}}\ddot{\boldsymbol{r}} \tag{B.14}$$

B.4 Full equations

In this section the expressions derived above are combined to obtain the actual equations of motion.

B.4.1 Rotational Dynamics

$$\nabla_{\dot{\boldsymbol{R}}}\left[\frac{1}{2}\left(\boldsymbol{\omega}^T\boldsymbol{J}\boldsymbol{\omega}\right)\right] - \left[\nabla_{\boldsymbol{R}}\left[\frac{1}{2}\left(\boldsymbol{\omega}^T\boldsymbol{J}\boldsymbol{\omega}\right)\right] - k_t\lambda\left(\boldsymbol{r}\boldsymbol{r}_{\text{br}}^{\overline{B}\,T}\right)\right] = \boldsymbol{F}_{\boldsymbol{R}} \tag{B.15}$$

Applying the $2P_{\boldsymbol{R}}$ operator on both sides and using the distributivity of the operator:

$$2P_{\boldsymbol{R}}\left(\nabla_{\dot{\boldsymbol{R}}}\left[\frac{1}{2}\left(\boldsymbol{\omega}^T\boldsymbol{J}\boldsymbol{\omega}\right)\right] - \nabla_{\boldsymbol{R}}\frac{1}{2}\left(\boldsymbol{\omega}^T\boldsymbol{J}\boldsymbol{\omega}\right)\right) + 2P_{\mathbf{R}}\left(k_t\lambda\left(\boldsymbol{r}\boldsymbol{r}_{\text{br}}^{\overline{B}\,T}\right)\right) = 2P_{\mathbf{R}}\left(\boldsymbol{F}_{\boldsymbol{R}}\right) \tag{B.16}$$

Using Preposition 1 from [23] this reduces to:

$$\boldsymbol{J}\dot{\boldsymbol{\omega}} + \boldsymbol{\omega}\times\boldsymbol{J}\boldsymbol{\omega} + 2P_{\mathbf{R}}\left(k_t\lambda\left(\boldsymbol{r}\boldsymbol{r}_{\text{br}}^{\overline{B}\,T}\right)\right) = \boldsymbol{M}^B \tag{B.17}$$

Where the generalized force $\boldsymbol{F}_{\boldsymbol{R}}$ is transformed to $\boldsymbol{M}^B$, the moments acting around the body centre of gravity, expressed in the body frame of reference. Using the definition of the operators as defined above:

$$\begin{aligned} 2P_{\boldsymbol{R}}\left(k_t\lambda\left(\boldsymbol{r}\boldsymbol{r}_{\text{br}}^{\overline{B}\,T}\right)\right) &= 2k_t\lambda\, P_{\boldsymbol{R}}\left(\boldsymbol{r}\boldsymbol{r}_{\text{br}}^{\overline{B}\,T}\right) && \text{(B.18)}\\ &= 2k_t\lambda\, U\left(\boldsymbol{R}^T\boldsymbol{r}\boldsymbol{r}_{\text{br}}^{\overline{B}\,T}\right) && \text{(B.19)}\\ &= k_t\lambda\left(\boldsymbol{r}_{\text{br}}^{\overline{B}}\times\boldsymbol{R}^T\boldsymbol{r}\right) && \text{(B.20)} \end{aligned}$$

Finally the resulting rotational equations of motion are given by B.21

$$\boldsymbol{J}\dot{\boldsymbol{\omega}} + \boldsymbol{\omega}\times\boldsymbol{J}\boldsymbol{\omega} + k_t\lambda\left(\boldsymbol{r}_{\text{br}}^{\overline{B}}\times\boldsymbol{R}^T\boldsymbol{r}\right) = \boldsymbol{M}^B \tag{B.21}$$

B.4.2 Translational dynamics

Combining all the terms derived earlier results in the equations of motion for the generalized coordinate $\boldsymbol{r}$ given by B.22. The generalized force vector $\boldsymbol{F}_{\boldsymbol{r}}$ reduces to $\boldsymbol{F}$ as the generalized forces are simply the forces acting on the center of mass expressed in the inertial frame of reference.

$$m_{\text{in}}\ddot{\boldsymbol{r}} + k_t\lambda\left(\boldsymbol{r} + \boldsymbol{R}\boldsymbol{r}_{\text{br}}^{\overline{B}}\right) - m_k g\mathbf{1}_3 = \boldsymbol{F} \tag{B.22}$$

B.4.3 Matrix notation

Combining all the terms and putting it in matrix notation:

$$\begin{bmatrix} m_{\text{in}} I_3 & 0 \\ 0 & \boldsymbol{J} \end{bmatrix} \begin{bmatrix} \ddot{\boldsymbol{r}} \\ \dot{\boldsymbol{\omega}} \end{bmatrix} = \begin{bmatrix} \mathbf{F} + m_k g \mathbf{1}_3 - k_t \lambda \left(\boldsymbol{r} + \boldsymbol{R} \boldsymbol{r}_{\text{br}}^{\overline{B}} \right) \\ \boldsymbol{M}^B - \boldsymbol{\omega} \times \boldsymbol{J}\boldsymbol{\omega} - k_t \lambda \left(\boldsymbol{r}_{\text{br}}^{\overline{B}} \times \boldsymbol{R}^T \boldsymbol{r} \right) \end{bmatrix} \tag{B.23}$$

B.5 Sanity check

In this section, an attempt is made to compare the results of the derivation above to common sense.

B.5.1 Translational dynamics

Investigating equation B.22, the expression is remarkably simple. The acceleration $\ddot{\boldsymbol{r}}$ is proportional to the external forces $\boldsymbol{F}$, the gravitational force $m_k g \mathbf{1}_3$ and the tether force $k_t \lambda \left(\boldsymbol{r} + \boldsymbol{R} \boldsymbol{r}_{\text{br}}^{\overline{B}} \right)$. The sign of the gravitational force is positive as both gravity and the direction of the inertial Z-axis point in the same direction.
The expression for the tether force is expanded below (equation B.24) which shows that the tether force vector is proportional to the equivalent spring stiffness k_t and the elongation of the tether Δl_t in the direction of the bridle point $\boldsymbol{e}_{\text{br}}^E$.

$$\boldsymbol{F}_t = -k_t \lambda \left(\boldsymbol{r} + \boldsymbol{R} \boldsymbol{r}_{\text{br}}^{\overline{B}} \right) \tag{B.24}$$

$$= -k_t \left[1 - \frac{l_{t0}}{\underbrace{\left(\left(\boldsymbol{r} + \boldsymbol{R} \boldsymbol{r}_{\text{br}}^{\overline{B}} \right)^T \left(\boldsymbol{r} + \boldsymbol{R} \boldsymbol{r}_{\text{br}}^{\overline{B}} \right) \right)^{1/2}}_{l_t}} \right] \underbrace{\left(\boldsymbol{r} + \boldsymbol{R} \boldsymbol{r}_{\text{br}}^{\overline{B}} \right)}_{l_t \boldsymbol{e}_{\text{br}}^E} \tag{B.25}$$

$$= -k_t \frac{\Delta l_t}{l_t} l_t \boldsymbol{e}_{\text{br}}^E \tag{B.26}$$

$$= -k_t \Delta l_t \boldsymbol{e}_{\text{br}}^E \tag{B.27}$$

B.5.2 Rotational dynamics

The expression shown in B.21 is again remarkably simple and is in essence Euler's equation for rigid bodies (Euler [66]). The term $k_t \lambda \left(\boldsymbol{r}_{\text{br}}^{\overline{B}} \times \boldsymbol{R}^T \boldsymbol{r} \right)$ is the moment caused by the tether force which might be at first glance counterintuitive. Rewriting the equation as shown in B.28 however shows that the contribution to the moments around the center of gravity due to the tether is simply the cross product of the tether force and the moment arm, expressed in the body reference frame.

$$\boldsymbol{M}_t^B = k_t \lambda \left(\boldsymbol{r}_{\mathrm{br}}^{\overline{B}} \times \boldsymbol{R}^T \boldsymbol{r} \right) \tag{B.28}$$

$$= -k_t \frac{\Delta l_t}{l_t} \left(\boldsymbol{r}_{\mathrm{br}}^{\overline{B}} \times \boldsymbol{R}^T \boldsymbol{r} \right) \tag{B.29}$$

$$= -k_t \frac{\Delta l_t}{l_t} \left(\boldsymbol{r}_{\mathrm{br}}^{\overline{B}} \times \boldsymbol{r}_{cg}^B \right) \tag{B.30}$$

$$= -k_t \frac{\Delta l_t}{l_t} \left(\boldsymbol{r}_{\mathrm{br}}^{\overline{B}} \times (\boldsymbol{r}_t^B - \boldsymbol{r}_{\mathrm{br}}^{\overline{B}}) \right) \tag{B.31}$$

$$= -k_t \frac{\Delta l_t}{l_t} \left[\boldsymbol{r}_{\mathrm{br}}^{\overline{B}} \times \boldsymbol{r}_t^B - \underbrace{\boldsymbol{r}_{\mathrm{br}}^{\overline{B}} \times \boldsymbol{r}_{\mathrm{br}}^{\overline{B}}}_{=0} \right] \tag{B.32}$$

$$= -k_t \frac{\Delta l_t}{l_t} l_t \left(\boldsymbol{r}_{\mathrm{br}}^{\overline{B}} \times \boldsymbol{e}_t^B \right) \tag{B.33}$$

$$= \boldsymbol{r}_{\mathrm{br}}^{\overline{B}} \times \boldsymbol{F}_{\boldsymbol{t}}^{\boldsymbol{B}} \tag{B.34}$$

Appendix C

Trajectory optimization using direct collocation

This appendix explains the numerical solution strategy to optimize kite trajectories. The method was developed by Horn et al., described in [24] and concerns a more general type of problems called, optimal control problems. Trajectory optimization is just one of many applications of optimal control problems. Since no contributions to this method are presented, it is covered here as an appendix. However, it should be stressed that this method is crucial in enabling the work in this research. Similarly, the development of the software tool *Rawesome* by Horn [25], incorporating the method above, proved indispensable. Both are described in the sections below which follow the structure of reference [24] but more explanation detail is added to some aspects.

Firstly, the optimal control problem (OCP) formulation is presented in section C.1. Subsequently, section C.2, describes how OCP is translated into an NLP using the direct collocation method. Section C.3 then describes the initial guess generation method. Finally, sections C.4 and C.5, briefly describe the NLP solver IPOPT and automatic differentiation framework CAsaDi, both implemented in Rawesome.

C.1 Optimal control problem formulation

The equations of motion describing the AWT can be written as a system of Differential Algebraic Equations (DAE):

$$0 = \boldsymbol{f}(\dot{\boldsymbol{x}}(t), \boldsymbol{x}(t), \boldsymbol{z}(t), \boldsymbol{u}(t), \theta, t) \tag{C.1}$$

where $\boldsymbol{x}$ represent the differential states, $\boldsymbol{z}$ algebraic variables, $\boldsymbol{u}$ control variables, θ parameters and time t. Contrary to [24], no Lagrange multipliers are used in the equations of motion since the tether was not modeled as a constraint. This eliminates algebraic variables from equation C.1, reducing it to an ordinary differential equation (ODE). However,

algebraic variables are used to generate feasible initial guess solutions (see section C.3) and are therefore included in the problem formulation.

The optimization objective J can be of a *Mayer* (J_M) or *Lagrange* ($\int_0^T J_L$) type or both. A Mayer term is a function of the states at the end of the trajectory, the parameters and the end time itself. For example, when optimizing the steering inputs on a racing on a track, a Mayer type objective could be the end time itself. A Lagrange term is the integral of a certain time varying function along the trajectory, e.g. the amount of fuel used in the example above. In order to use a Lagrange term, the integral should be approximated numerically, often referred to as quadrature, discussed in more detail in section C.2

A number of (in)equality constraints $\boldsymbol{h}$ and bounds on the states, controls, parameters, algebraic variables, and end time are also applied. Lastly periodic boundary conditions $\boldsymbol{c}$ are apply on states and controls. This results in the following optimal control problem:

$$
\begin{aligned}
\text{minimize} \quad & J_M(\boldsymbol{x}(T), \theta, T) + \int_0^T J_L(\boldsymbol{x}(t), \boldsymbol{u}(t), \boldsymbol{z}(t), \theta, T) \\
\text{subject to} \quad & 0 = \boldsymbol{f}(\dot{\boldsymbol{x}}(t), \boldsymbol{x}(t), \boldsymbol{z}(t), \boldsymbol{u}(t), \theta, t) && t \in [0, T] \\
& 0 \geq \boldsymbol{h}(\boldsymbol{x}(t), \boldsymbol{z}(t), \boldsymbol{u}(t), \theta, t) && t \in [0, T] \\
& \boldsymbol{x}_{\min} < \boldsymbol{x}(t) < \boldsymbol{x}_{\max} && t \in [0, T] \\
& \boldsymbol{z}_{\min} < \boldsymbol{z}(t) < \boldsymbol{z}_{\max} && t \in [0, T] \\
& \boldsymbol{u}_{\min} < \boldsymbol{u}(t) < \boldsymbol{u}_{\max} && t \in [0, T] \\
& \theta_{\min} < \theta < \theta_{\max} \\
& T_{\min} < T < T_{\max} \\
& 0 = \boldsymbol{c}(\boldsymbol{x}(0, T),\ \boldsymbol{u}(0, T))
\end{aligned}
\tag{C.2}
$$

C.2 Discretization using Direct Collocation

For a full discussion of the discretization method, the author refers to [24], the general outline is discussed here. In direct collocation, both the control and the state trajectories are discretized into N intervals. The control variables are in this case chosen at a constant level in each interval. The states are approximated by a Lagrange interpolating polynomial with degree D and D+1 control points (called collocation nodes). Each collocation node in interval $I_i = [t_{i,0}, t_{i+1,0}]$ represents a point in parametrized time $t = t_{i,0} + \tau \frac{T}{N}$ with $\tau \in [0, 1]$, and $i \in [0, N-1]$. The polynomial can then be described using closed form expressions C.3 and C.4.

$$
\mathbf{x}_i^D(t) = \sum_{j=0}^{D} \xi_j(\tau) \mathbf{x}_{i,j} \tag{C.3}
$$

$$
\xi_j(\tau) = \prod_{k=0, k \neq j}^{D} \frac{\tau_k - \tau}{\tau_k - \tau_j} \tag{C.4}
$$

Since the polynomial is parametrized by time, an expression for the derivative of the

polynomial $\dot{\mathbf{x}}_i^D(t)$ is known in closed form:

$$\dot{\mathbf{x}}_i^D(t_{i,0} + \tau\frac{T}{N}) = \sum_{j=0}^{D} \frac{N}{T}\xi_j'(\tau)\mathbf{x}_{i,j} \tag{C.5}$$

The model equations are imposed to be equal to this polynomial derivative at the collocation nodes as shown in figure C.1.

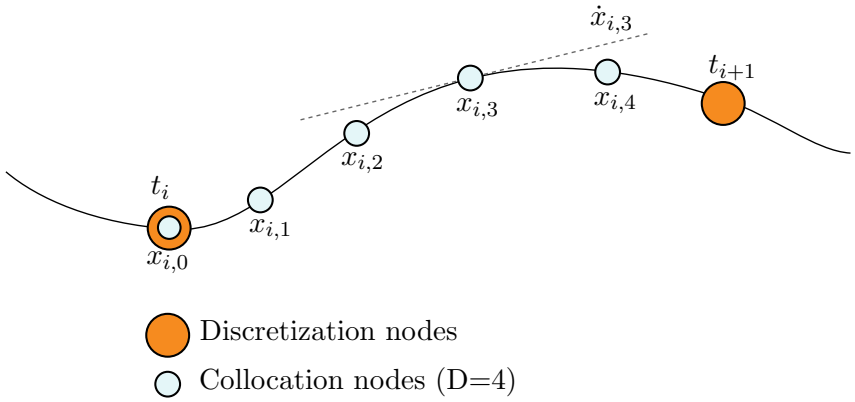

Figure C.1: State trajectory discretization using collocation: the shape of the polynomial is fixed by imposing the model equations as the polynomial derivative (dotted line) at the collocation nodes

The value of the state at the end of the interval i (not part of the collocation points) can then be determined as follows:

$$\mathbf{x}_{i+1,0} = \mathbf{x}_i^D(t_{i+1,0}) = \sum_{j=0}^{D} \xi_j(1)\mathbf{x_{i,j}} \tag{C.6}$$

This is in essence a numerical integration of the state over the last part of the interval. In oder to guarantee this integration is accurate, the collocation points are chosen as the zeros (roots) of the shifted Gauss-Jacobi polynomials [54]. The result of equation C.6 provides the first collocation point of the next interval. In the same fashion, the collocation equations C.5 can be determined for each interval and coupled through expression C.6.

Lagrange terms appearing in the cost function such as shown in equation C.2 can be discretized and calculated in a similar way. If the integral quantity only appears in the objective, this can be done without adding an extra state to the system. Such a variable is referred as a *quadrature state*.

C.3 Initial guess using pseudo forces

As the search space for the optimization is large, an initial guess has to be provided to the algorithm. A suitable method to generate an initial guess is implemented in Rawesome and is briefly explained here. In order to obtain a feasible initial guess of all states, control variables and parameters, a separate optimization problem (using the

same method described above) is formulated. The cost function is in this case the sum of the offsets between the kite position at the collocation nodes and a user-defined 3-D trajectory. This will force the optimization to find the required control input such that the user-defined trajectory can be flown with the supplied equations of motion.

However, even with this simplified cost function, the algorithm is unlikely to find a feasible trajectory in a reasonable time. In order to approach a feasible guess faster, the equations of motion are augmented with so called *pseudo forces* on all degrees of freedom. These non-physical forces are implemented as algebraic variables which are decision variables of the optimization at each discretization and collocation node. This allows the optimization to directly force the kite to fly a certain physical path, as if a set of rocket boosters was attached on each axis (and a rotary equivalent). The optimization is then executed multiple times, each time using the solution of the previous step as the initial guess for the next. Step by step the the gain of the pseudo forces is forced to zero.

It's important to stress that the optimal solution of the algorithm will be a local one and will have the same *topology* as the provided initial guess. W.r.t. the physical 3D trajectory, topology is in this case related to the winding number of the path. This is covered in more detail section 3.2.1.

C.4 Nonlinear programming using IPOPT

With the problem now discretized, the optimal control problem can be formulated as a nonlinear programming problem. The full NLP problem statement can be found in [24] but is omitted here. The set of collocation equations is large but sparse and allows the use of specialized solvers. Since an interface was provided in Rawesome, the Interior Point OPTimizer IPOPT, developed by Wächter and Biegler [52] was used. IPOPT uses a primal-dual interior-point algorithm with a filter line-search method and has been used numerous times in the field of nonlinear programming.

C.5 Automatic Differentiation using CasADi

In order to reduce the computational cost of solving the NLP, gradient information is supplied using the automatic differentiation (AD) package CasADi, developed by Joel Andersson et al. [39]. AD applies the chain rule to the elementary operations a computer program executes to solve a (complicated) function. This results in a direct expression for the gradients of that function with an error as small as working precision. CasADi provides an interface to IPOPT which is used by Rawesome. An important consequence of using AD is that all used expressions should be formulated as a continuous function, e.g. no lookup tables can be used.